A Thermodynamic Analysis of Microbial Surface Chemistry and Metabolic Strategies

Addien C. Wray

A dissertation
submitted in partial fulfillment of the
requirements for the degree of

Doctor of Philosophy

University of Washington

2022

Reading Committee:

Drew Gorman-Lewis, Ph.D., Chair

John Baross, Ph.D.

Fang-Zhen Teng, Ph.D.

Program Authorized to Offer Degree:
Department of Earth and Space Sciences

University of Washington

Abstract

A Thermodynamic Analysis of Microbial Surface Chemistry
and Metabolic Strategies

Addien C. Wray

Chair of the Supervisory Committee:
Drew Gorman-Lewis, Ph.D.
Department of Earth and Space Sciences

A thorough understanding of microbial life on Earth and effective methods of searching for life beyond Earth require the description of possible interactions between those organisms and their geochemical environments. Such assessments need to include both a quantitative description of the chemical reactions involved and the capability to predict the favorability of their occurrence. These can both be addressed by measuring the thermodynamic properties of microbial activities. We can think of those activities in two regimes, passive and active, where the former involves surficial reactivity and the latter concerns growth-related processes. Research to date has quantified some thermodynamic properties, such as stability constants of passive processes and standard-state Gibbs energies of active processes, for a diverse suite of microbial taxa. Little work, however, has sought to thoroughly assess passive and active microbial bioenergetics by quantifying all three thermodynamic terms: ΔH, ΔG, and ΔS. This dissertation applies this more detailed approach to (1) the surface reactivity of a common groundwater bacterium, (2) U(VI) adsorption onto that microbe, (3) aerobic and anaerobic bacterial growth, and (4) methanogenic archaeal growth. In doing so, I demonstrate that the bacterium *Shewanella putrefaciens* strain CN32 has three energetically distinguishable functional groups (carboxyl, polyphosphate, and amine), where the amine group undergoes a measurable conformational change with alterations to ionic

strength. Moreover, I identify the reactions between those functional groups and U(VI) under a variety of geochemical conditions, along with the stability constants of those reactions. I also demonstrate that aerobic and anaerobic growth by CN32 yield measurably different thermodynamic trends as a function of temperature, where growth efficiency is affected primarily by the production of extra-cellular exudates and physiological stress. Lastly, I present the first bioenergetic description of hyperthermophilic methanogenesis, by *Methanocaldococcus sp.* FS406-22, and demonstrate the effects temperature has on that growth efficiency, where growth proceeds best in the middle of the possible range of temperatures. In sum, the data presented in this dissertation help to expand our understanding of a range of microbial-geochemical interactions under varied conditions and will help us to better assess the impacts microbial life may have on systems on Earth as well as inform our search for it elsewhere.

TABLE OF CONTENTS

LIST OF FIGURES

LIST OF TABLES

ACKNOWLEDGMENTS

First must come the science. For all of the discussions, suggestions, and guidance I sincerely thank my advisor, Drew Gorman-Lewis. I am beyond thankful for the patience and calm atmosphere you brought to this journey. You have made it an exhilarating, thought-provoking one. I am also grateful to the members of my committee: Fang-Zhen Teng, John Baross, Robert Morris, and Christopher Anderson. Without your insights and inputs this would, quite literally, not have been possible.

Science, of course, does not exist in a vacuum and this dissertation was no exception. To my parents, Alan and Vanessa Wray, and my partner, Ayla Heinze Fry, I extend the deepest thanks. Your love and kindness has meant so much and brought with it such an invaluable framework of support. I cannot imagine having completed this work without each of you at my side. I am profoundly grateful.

DEDICATION

for Alan and Vanessa

Chapter 1
INTRODUCTION

1.1 Organization of the Dissertation

Chapter 1 provides a brief introduction to the dissertation, outlining the primary motivations for the work and summarizing the contents of the subsequent chapters. Chapters 2-5 are structured as independent papers, Chapter 6 outlines the astrobiological contributions of the work, and Chapter 7 summarizes the main conclusions from the dissertation. Chapter 2, **Thermodynamic and spectroscopic investigations of *Shewanella putrefaciens* CN32 cell envelope**, was published in *Chemical Geology* in June 2022. Chapter 3 describes **Surface complexation of U(VI) onto *Shewanella putrefaciens* CN32**. Chapter 4 covers the **Bioenergetics of aerobic and anaerobic growth of *Shewanella putrefaciens* CN32**, and Chapter 5 discusses **Bioenergetic effects of H_2 limitation and temperature on *Methanocaldococcus sp.* FS406-22**.

1.2 Motivation

The overall goal of this dissertation is to improve our understanding of passive and active microbial processes through a thermodynamic description of the reactions involved. Thermodynamic constraints on life are central to accurate assessments of not only the presence of habitable environments on exoplanets, but the magnitude of that habitability (i.e., what types of life can be supported and at what scale). This dissertation is divided into four chapters, addressing first microbial surface reactivity and complexation and, second, microbial metabolic strategies.

The surface properties of microbes, in addition to their importance for understanding their impacts on local geochemistry, are also essential to understanding how life has

adapted to fill those niches in the first place. Specifically, for a microbe to complete its metabolism (i.e., perform both catabolism and anabolism), it must uptake nutrients. This is largely done by cross-membrane transport from the environment into the cell. Nutrient acquisition, mediated by surface interactions, gives an adaptive advantage to microbial life but has yet to be explored in detail in terms of the thermodynamic properties of the surface structure. This work will help to fill this gap and will directly address a key element of the NASA Astrobiology Roadmap, wherein "properties of energy transduction, transport of nutrients, growth, and division" warrant investigation. In all, the evolution and diversification of microbial surficial properties was a necessary step in the success of life on Earth, plays a key role in our understanding of life's origin, and encompasses Chapters 1 and 2 of the dissertation.

By also applying this thermodynamic approach to microbial metabolisms, we can better understand the variables that contribute to habitability on Earth, while also informing our search for life elsewhere. Vital to that effort is a quantitative understanding of the energetic requirements for terrestrial life. This means we need to describe the bioenergetics of microbial metabolisms across a range of metabolic strategies; that approach is applied in Chapters 3 and 4. Specifically, in Chapter 3 I discuss the bioenergetics of metabolic O_2 and Fe(III) reduction to understand the relative energetic requirements of aerobic- versus metal-based metabolisms, which may be important in nutrient-limited extraterrestrial environments. Additionally, these data help to place constraints on life earlier in Earth's past, prior to the oxygenation of the atmosphere, where anaerobic metabolisms like Fe(III) reduction were dominant. In Chapter 4, I quantify a process similar to what was likely one of the earliest metabolic strategies: methanogenesis. Specifically, that work focuses on a hyperthermophilic archeaen found at hydrothermal vents (which are themselves locales of particular interest regarding the origin of life). This combination of habitat and metabolism is strong motivation for measuring the energetic limits of growth for that archeaen and will deepen our understanding of this underexplored area of research. Chapters 3 and 4 com-

bined address the question of how much energy is required for microbial metabolisms to proceed, which is a requirement for understanding the potential habitability of exoplanets. What follows is a more detailed chapter-by-chapter summary.

1.3 Chapter Descriptions

Chapter 2: Thermodynamic and spectroscopic investigations of S. putrefaciens CN32 cell envelope

In Chapter 2, I present quantification of the surface reactivity of *Shewanella putrefaciens* CN32, a common gram-negative bacterium found in groundwater systems. The metabolic plasticity exhibited by CN32 allows it to survive in a variety of habitats, both aerobic and anaerobic, and thus makes measurements of its surface reactivity applicable to a range of geochemical conditions. I identified three discrete binding sites on CN32 as carboxyl, phosphoryl, and amine groups. In addition, for each site I measured their stability constant, concentration, and protonation enthalpy and entropy. Lastly, I demonstrated how ionic strength impacts these surface properties and described a conformational change of the amine group with increased ionic strength. This demonstrates that important alterations to microbial surface protonation properties can be caused by ionic strength changes -– a causal relationship that has to date been unresolved in the literature. These data allow for the prediction of how the surface of CN32 may react with geochemical components in its environment. These descriptions are essential to accurately understand the adaptations of microbial surfaces in relation to nutrient acquisition, which ultimately begins on the outermost portion of the cell envelope. Moreover, these data allow us to define how changes in salt concentrations affect those surface adaptations, which is important to better predict how microorganisms may impact, and be impacted by, systems where salinity either changes over time or is physically stratified, such as in brine fluids and ocean moons.

Chapter 3: Surface Complexation of U(VI) onto S. putrefaciens CN32

The third chapter builds directly from the results of Chapter 2, wherein I describe the adsorption of a heavy metal, U(VI), onto CN32. Towards that end, I measured how three geochemical variables impact adsorption: ionic strength, pH, and the co-presence of other cations. This culminated in the identification of specific U(VI)–CN32 reactions and associated stability constants. This work demonstrated interesting parallel trends in ionic strength at high pH, where the maximum and minimum ionic strengths tested resulted in greater adsorption than an intermediate concentration, but for likely opposing reasons (an expanded double layer versus increased cationic bridging, respectively). I also identified countervailing impacts of two divalent cations (Mg^{2+} and Ca^{2+}), where increased bridging effects (Mg^{2+}) increased adsorption and contrasted with alterations to surface chemistry (Ca^{2+}), which reduced adsorption. Ultimately, this work helps to quantify a useful microbial adaptation that results in the removal of a toxic compound from solution. This may impart improved growth conditions for the subject microbe and co-present organisms. As new systems are examined beyond Earth, this work will help to refine our descriptions of localized habitability to include, potentially, habitats with what would otherwise be considered inhospitable due to heavy metal presence.

Chapter 4: Bioenergetics of metabolic O_2 and Fe(III) reduction by S. putrefaciens CN32

In this chapter, I examined the bioenergetics of O_2 and Fe(III) reduction coupled to lactate oxidation in CN32 during growth. I made measurements over a range of temperatures (25-36°C) to infer how CN32 allocates its energy in terms of maintenance and growth. For aerobic growth, growth efficiency (energy normalized to biomass produced) increased with temperature to 30°C, beyond which it decreased slightly. Fe(III) growth efficiency was insensitive to temperature below 30°C and decreased dramatically above it. By comparing ΔH and ΔG measurements, I established that maintenance (i.e., non-growth) reactions are exothermic and decrease in activity with growth efficiency for both metabolic strate-

gies. Uniformly, however, more non-growth energy was expended for aerobic growth than Fe(III) growth, which suggests growth under anaerobic conditions comes at a substantial energetic cost. The examination of how energy is dissipated requires measurement of both ΔG and ΔH, and this work demonstrates that accurate assessments of habitability require quantification of bioenergetics in terms of both parameters. That approach allows us to quantify how adaptation to complex geochemical systems, such as those with fluctuations in available electron acceptors, affects the efficiency by which microbes can grow. This work, specifically, provides thermodynamic context for the requirements of aerobic and anaerobic growth, which is useful in defining habitability from a geochemical perspective and can aid in more accurately assessing energetic availability in heterogeneous habitats, on Earth and elsewhere.

Chapter 5: Bioenergetic effects of H_2 limitation and temperature on Methanocaldococcus FS406-22

In Chapter 5, I expand the application of bioenergetics from mesophilic growth to hyperthermophilic growth with the archeaen *Methanocaldococcus sp.* FS406-22. FS406 exhibits metabolism that is both fundamental to the origin of life (methanogenesis) and its subsequent diversification (N-fixation). Here I focus on constraining the growth parameters of non-N-fixing methanogenic growth, such that future work can decouple the effects of methanogenesis from N-fixation. In this work, I quantified the bioenergetics of growth at three temperatures (65, 76, and 85°C). At each temperature, a range of biomass yields was produced by varying substrate (H_2) concentration. This allowed me to investigated the stress response by FS406 and to elucidate the relationship between the magnitude of growth and the associated thermodynamics. The results showed that growth efficiency was maximized when substrate concentration (and, thus, biomass yield) was highest and the growth temperature was in the middle of the range examined (76°). Correspondingly, as efficiency decreased, so did biomass yield. Importantly, as with CN32, the dissipation of Gibbs energy into enthalpy and entropy showed that non-growth reactions were both

exothermic and increased with decreased efficiency. Overall, this chapter helps to define the bioenergetic requirements of growth similar to some of the earliest life, which allows for constraints to be made regarding the thermodynamic requirements of those organisms. In addition, this work provides crucial data to contextualize potential life in unexamined hydrothermal systems on Earth, in its early history when hydrothermal activity was greater, and in hydrothermal systems beyond it, such as on the icy moons Enceladus and Titan.

Chapter 2

THERMODYNAMIC AND SPECTROSCOPIC INVESTIGATIONS OF *SHEWANELLA PUTREFACIENS* CN32 CELL ENVELOPE

This manuscript was published in Chemical Geology:

https://doi.org/10.1016/j.chemgeo.2022.120853

Co-authored by Addien C. Wray and Drew Gorman-Lewis

Abstract

A quantitative understanding of prokaryotic cell envelope reactivity is necessary to accurately describe the surface complexation reactions known to impact metal transport in the subsurface. The gram-negative bacterium *Shewanella putrefaciens* CN32 (CN32) has been the focus of previous cell envelope studies in large part due to its ability to directly influence iron and uranium geochemistry; however, important gaps remain in our understanding of reactions occurring on its cell envelope. Combining surface complexation modeling of potentiometric titration data with isothermal titration calorimetry provides an additional method to evaluate how well surface complexation models (SCMs) represent cell envelope reactivity. It also gives us the ability to determine site-specific enthalpies and entropies of protonation, which can aid both in site structure identification and description of conformational changes to those sites, further improving our understanding of the CN32 cell envelope. We gathered potentiometric and isothermal calorimetric titration data of CN32 over a range of ionic strength (0.02 – 0.53 M) while monitoring cell viability and performing Fourier transform infrared spectroscopy (FTIR) investigations. FTIR analysis was performed over a range of pH (4 – 9.4) to confirm identification of proton-active sites. Surface complexation modeling revealed that models involving 3 and 4 sites could adequately describe the potentiometric titration data; however, a 3-site model best repre-

sented the calorimetric data. We inferred the following site identities based on characteristic enthalpies, entropies, and equilibrium constants of protonation: carboxyl (log(K): 4.79 – 4.95), phosphoryl (6.69 – 6.97), and amine groups (9.37 – 9.64). Spectral corroboration via FTIR indicated the presence of chemical moieties consistent with these functional group assignments. Ionic strength was shown to have a significant impact on the concentration of all three sites at 95% confidence. Entropies and equilibrium constants of protonation for carboxyl and phosphoryl sites did not significantly change with ionic strength. For the carboxyl group, enthalpies of protonation varied significantly between the lowest and highest ionic strengths examined, though enthalpies at intermediate concentrations were not distinguishable. Enthalpies of protonation for the amine group were statistically different at each ionic strength. Additionally, entropies and equilibrium constants of protonation for the amine group were significantly affected by all ionic strengths tested. The entropy of protonation for the amine site changed from -21.5 ± 6.1 to $+109.0 \pm 4.2$ J/molK^{-1} as ionic strength increased from 0.02 to 0.53 M, respectively. A change in the entropy of protonation of this magnitude and sign is indicative of a substantial conformational change in this functional group. Cell viability was significantly impacted over the course the titrations; however, viability did not impact SCMs results. In sum, these data fill gaps in our understanding of CN32 and provide new insights into the intricacies of its cell envelope.

2.1 Introduction

The gram-negative bacterium *Shewanella putrefaciens* has been the focus of numerous geochemical and geobiological studies in recent years, in large part due to its ability to directly influence iron and uranium geochemistry (e.g., Lovley et al., 1991; Lovley & Phillips, 1992; Haas et al., 2001; Liu et al., 2001a; Sokolov et al., 2001; Smith & Ferris, 2003; Furukawa & Dale, 2013; Belli et al., 2015). *S. putrefaciens* is a facultative anaerobe, allowing it to survive in both near-surface and sub-vadose zone environments (Lovley et al., 1991; DiChristina & DeLong, 1993). This habitable plasticity provides opportunity for *S. putrefaciens* to interact with Fe and U throughout the subsurface, both metabolically and through surface complexation. Multiple strains of *S. putrefaciens* (e.g., 200, MR-1, CN32) are known to reduce U(VI) and Fe(III) while also adsorbing those compounds (respectively, see Belli et al. (2015), Myers & Nealson (1990), and Lovley et al. (1991)). These processes have the potential to affect the transport of Fe and U in aqueous systems by removing them from the aqueous phase (either through a change in oxidation state or via complexation on surface sites). The metabolic and surface properties of these strains have been investigated (e.g., Haas et al., 2001; Sokolov et al., 2001; Smith & Ferris, 2003; Furukawa & Dale, 2013; Belli et al., 2015); however, the scope of these studies is limited by the narrow range of geochemical conditions considered and the methods used to probe surface interactions between *S. putrefaciens*, protons, and metals. While previous research has shed important light on the surface reactivity of *S. putrefaciens* (e.g., Haas et al., 2001; Sokolov et al., 2001; Smith & Ferris, 2003), lacking from the literature is a comprehensive study across ionic strength that includes an understanding of temperature dependence and spectroscopic examination of the surface. Each of these are important steps in assessing interpretations of potentiometric titrations to understand surface reactivity.

The microbial surface, while sometimes compared with mineral surfaces, is a complex structure with a more nuanced coordination environment responsible for complexation reactions (Fein, 2006). Given its three dimensional nature and the fact that conformational

changes can occur in constituents within the "cell surface" (Rahnamoun et al., 2020), from here forward we will be referring to the outermost portion as its cell envelope. The outer membrane of gram-negative bacteria consists of an oligosaccharide, and a subset of those also contain an O-specific oligosaccharide anchored by lipid A (Nazarenko et al., 2003; Krasikova et al., 2004). Functional groups are found within lipid A, including anionic oxygen within carboxylic acids, phosphates, and possibly phenols (Jiang et al., 2004; K. Auer & B. Weibel, 2017). Proteins are embedded throughout the lipopolysaccharides (LPS) that are also present in the outer membrane, but likely compose at least an order of magnitude less mass than the total LPS (Beveridge & Murray, 1980; Jiang et al., 2004; Silhavy et al., 2010). These proteins can also contain a variety of functional groups, including anionic oxygen, thiol, and amine ligands with proton-ionizable side chains (Welte et al., 1995; Koebnik et al., 2000; Nell & Fein, 2017). The observed surface chemistry is also strongly affected by the growth medium used (Furukawa & Dale, 2013; Paulo et al., 2018). Thus, meaningful comparisons of cell envelope structure and reactivity need to be done with microbes that have been similarly cultured.

To date, a small body of research has analyzed the surface of CN32 from a geochemical perspective, wherein surface complexation models (SCMs) focus on predicting ion binding by using stability constants and balanced chemical equations. SCMs from Sokolov et al. (2001) and Smith & Ferris (2003) are largely in agreement regarding the potential reactive sites on CN32 when modelled with this approach. Missing from the literature, however, is a surficial analysis of CN32 from a biological perspective, where the cell envelope is the focus of the analysis, aimed at enhancing our understanding of how the cell envelope may react to changes in geochemical conditions. This would also, in turn, better constrain inferences of how that biology affects the pH of a system. The measurement of enthalpies of protonation via isothermal titration calorimetry (ITC), is a powerful tool for analyzing that coordination environment. Specifically, ITC data can be used to derive site-specific enthalpies of protonation when combined with SCMs and allow for the calculation of en-

tropies of protonation. Since ITC data can be more sensitive than potentiometric titration data, this approach can illuminate intricacies of surface reactivity that are not detected in modeling of potentiometric titration data alone (Gorman-Lewis, 2011; Harrold & Gorman-Lewis, 2013; Gorman-Lewis et al., 2014). Importantly, the ability to test SCMs with an additional dataset like ITC allows us to constrain those models to better reflect the reactivity of the cell envelope.

Ionic strength has long been understood to impact mineral surface complexation reactions (Robertson & Leckie, 1997; Peak et al., 1999; Goldberg & Johnston, 2001; Hao et al., 2019). However, the complexity of bacterial cell envelopes impedes the use of electrostatic models, which are typically designed for mineral surfaces, in describing microbial surface reactivities. When applied, electrostatic models have been shown repeatedly to over-predict electrostatic effects (Borrok & Fein, 2005; Fein et al., 2005; Gorman-Lewis, 2009). The application of non-electrostatic models to describe bacterial surface complexation has been widely used, whereby apparent constants are derived at ionic strengths of interest (Bishop et al., 2019; Borrok & Fein, 2005; Borrok et al., 2005b,a; Butzen & Fein, 2019; Fein et al., 2005; Flynn et al., 2014; Gorman-Lewis et al., 2005b; Gorman-Lewis et al., 2019; Gorman-Lewis, 2014; Ginn & Fein, 2009; Liu et al., 2020; Phoenix et al., 2002). Using apparent constants is a preferable approach for making comparisons across ionic strength as it eliminates the uncertainty associated with applying electrostatic models to microbial surfaces.

For microbial surfaces, studies to date have largely focused on whether ionic strength changes the reactivity of the cell surface (Plette et al., 1995; Daughney & Fein, 1998; Martinez et al., 2002; Borrok & Fein, 2005; Fein et al., 2005; Tourney & Ngwenya, 2010). Less examined is the role ionic strength may play in directly altering the structure of the cellular envelope, and how those changes may be reflected in SCMs and ITC data. Enthalpies (ΔH) and particularly entropies (ΔS) of protonation are sensitive to solution conditions which impart structural changes on ligands (Edward J. King, 1965). While log(K) values (or Gibbs energies of protonation, ΔG) may not be substantially impacted by changes in

ionic strength, the structure of the envelope may still be altered. We can take advantage of the sensitivity of ΔH and ΔS to make inferences about that alteration, potentially yielding information about temperature dependence, coordination environment, and individual site structure (Gorman-Lewis, 2011; Harrold & Gorman-Lewis, 2013; Gorman-Lewis et al., 2014).

Examinations of the identity of CN32 surface sites, to date, are similarly limited. Sokolov et al. (2001) assigned functional group structures to each log(K) value they identified, but determined those by correlation of log(K) values to sites on *Bacillus subtilis* identified spectroscopically by Cox et al. (1999). Some spectroscopic analysis has shown a high density of carboxyl groups on CN32 (Adhikari et al., 2017), along with adsorption of Fe(II) onto carboxyl groups on CN32 (Liu et al., 2001a). Importantly, both of these studies were focused on the structure of mineral precipitates on *S. putrefaciens* and did not include variations in pH or ionic strength, were not compared to other techniques, such as Fourier transform infrared spectroscopy (FTIR), and did not identify the number and structure of each functional group. In all, a detailed description of the coordination environment of the functional groups on CN32 is missing from the literature.

A more complete examination of the surface properties of CN32 is needed. Towards that end, we examined CN32 with potentiometric titration, ITC, FTIR, and cellular viability tests. This work supplements the gaps left in the literature and includes results on the influences of ionic strength and temperature on protonation properties, spectroscopic examination of the structure of functional groups, the enthalpic and entropic properties of those groups, and measurements of cell viability and surficial integrity across multiple titrations. These data ultimately improve our understanding of the CN32 surface.

2.2 Materials and Methods

2.2.1 Cell preparation

CN32 was grown using procedures similar to previous work with that strain (Sokolov et al., 2001; Smith & Ferris, 2003). 5 mL volumes of 30 g/L trypticase soy broth (TSB) were inoculated from cultures of CN32 maintained on a TSB-yeast extract agar. Cultures were grown on an orbital shaker at 120 rpm and 30°C for 24 hours (±4 h). The 5 mL cultures were then used to inoculate larger volumes of TSB, with an inoculation percent of 0.5 %. Cells were harvested during late exponential phase, which was reached after 24 hours (±2 h) of growth.

The biomass was isolated by centrifugation at $5,000\ g$ for 15 minutes. The resulting pellet was washed in a sodium perchlorate solution at either 0.01, 0.1, or 0.5 M by vortexing, centrifuging at $6,552\ g$ for 2 – 4 minutes, and discarding the supernatant. Cells were washed three times, then centrifuged at $6,552\ g$ for two consecutive 30 minute periods. After each 30 min period, any remaining supernatant was removed. Cells were stored at 4°C and used within 24 hours.

2.2.2 Potentiometric titrations

A sodium perchlorate solution (at a concentration of 0.01, 0.1, or 0.5 M) was sparged with N_2 for 1 hour. The sparged solution was placed in an anaerobic chamber and, while stirring, allowed to equilibrate with the atmosphere ($\approx$ 98:2, N_2:H_2) for 30 minutes. Washed cells were suspended in the electrolyte solution, in the anaerobic chamber, by vortexing. The final concentration of the suspended biomass was 40 g/L (wet weight). The volume of sparged sodium perchlorate varied accordingly, ranging from approximately 75 – 125 mL. While in the anaerobic chamber, the suspension was adjusted to approximately pH 10 with CO_2 free NaOH and then titrated to approximately pH 4 with 0.2516 M $HClO_4$ at 0.025 or 0.05 mL increments and 2 minute intervals.

To test the ability of CN32 to withstand multiple protonation/deprotonation reactions, deemed here as 'reversibility,' we performed two potentiometric titrations on the same suspension. Following each initial titration, suspensions were adjusted back to pH 10 with CO_2 free NaOH. The suspensions were then titrated to pH 4 following the same protocol. The initial ionic strengths for these suspensions were 0.02 – 0.04 M (low), 0.11 – 0.13 M (medium), and 0.51 – 0.53 M (high). The pH electrodes were calibrated to H^+ concentration by Gran analysis of titrations of sodium hydroxide in a solution of $NaClO_4$ that was within the experimental ranges (low, medium, and high). Gran analysis was performed with the GLEE software program (Gans & O'Sullivan, 2000). To ensure reproducibility of the entire growth, washing, suspension, and titration procedure, titrations were done with two cell suspensions per ionic strength.

2.2.3 Titration calorimetry

We performed isothermal titration calorimetry (ITC) on a TAM III nanocalorimeter that measures heat flux between a reaction and reference vessel as a function of time (Johansson & Wadsö, 1999; Goldberg & Wadsö, 2001). Calorimetric response was calibrated by electrical heating and verified by measuring protonation of TRIS at 25°C (Grenthe et al., 1970). A computer-controlled Lund syringe pump delivered aliquots of acid to the reaction vessel in the calorimeter and to an identical, external sample being monitored by an Orion 8103BN Ross semi-micro combination pH electrode calibrated as described above.

Cells were suspended in N_2 sparged $NaClO_4$ such that the final biomass concentration was 10 g/L (wet weight). As with the potentiometric titrations, the concentrations of $NaClO_4$ used were 0.01, 0.1, and 0.5 M and the suspension was adjusted to approximately pH 10 in an anaerobic chamber using CO_2 free NaOH. 2.5 mL aliquots of the suspension were pipetted into Hastelloy vials for ITC analysis and an external reaction vessel for pH monitoring.

Each suspension began at approximately pH 10 and was titrated to approximately pH

4 by injecting 2 μL aliquots of 0.143 M $HClO_4$ into both the ITC reaction vessel and the external suspension. To allow the heat signal to reach the baseline between injections, injections were spaced apart at 20 minute intervals. Titrations were performed on two cell suspensions at each ionic strength.

We determined the heat produced from cell surface protonation reactions ($Q_{corr,v}$, Equation 2.1) with each addition of acid (v) by subtracting the background heats (i.e., heats of dilution, $Q_{bkg,v}$), from the ITC data ($Q_{meas,v}$). Background heats were determined as described above in cell-free solutions.

$$Q_{corr,v} = Q_{meas,v} - Q_{bkg,v} \tag{2.1}$$

Heats of hydroxide neutralization ($H^+ + OH^- \rightarrow H_2O$) were calculated from the measured pH change for each step of a titration using enthalpies of hydroxide neutralization for each ionic strength (Table 1 in Supplemental Materials) and were included in $Q_{bkg,v}$.

2.2.4 Fourier transform infrared spectroscopic analysis

The identities of surface moieties were probed spectroscopically via FTIR. Cells were grown and washed as described above and then suspended in a solutions of 0.1 M $NaClO_4$ at ca. pH 4, 5, 6.5, 8, and 9.5. The suspensions were centrifuged at $6,552$ g for 1 hour and the resulting pellets were then analyzed on a Perkin Elmer Frontier FTIR spectrometer with an ATR attachment. An averaged spectrum was produced from 120 scans over the range of $4,000 - 400$ cm^{-1} with a resolution of 4 cm^{-1}. The background electrolyte (0.1 M $NaClO_4$) was subtracted from the spectra using the same scan parameters as the bacterial pellets. We applied an asymmetric least squares baseline correction to the spectra (Eilers, 2004) and trimmed the data to include only the fingerprint region ($1800 - 900$ cm^{-1}). The spectra were normalized to the area under the amide II group (Kenney et al., 2018). The type of surface moieties were then identified by comparing the wavenumbers of peaks to known

vibrations in the literature.

For those peaks with multiple possible assignments, or with significant spectral overlap, we performed spectral deconvolution modeling with Gaussian curves. Individual Gaussian functions were fit to the region containing target peak/peaks using Fityk (Wojdyr, 2010). The number of peaks fit to the data was constrained by the number of known vibrations for the potential chemical assignments in that spectral region.

2.2.5 Cell viability quantification

Cell viability was checked during cell isolation and the potentiometric experiments in the high ionic strength system. All samples were centrifuged at $6,552\ g$ for 2 minutes, the supernatant discarded, and the cells suspended in a filter-sterilized phosphate buffered solution at pH 7. A 3:1 mixture of propidium iodide (20 mM, PI hereafter) and SYBR Green I ($10,000\ \times$ stock, Invitrogen) was prepared and diluted by a factor 1:5 in filter-sterilized DI water. The PI/SYBR Green mixture was then added to the suspended cells at a ratio of 1:10 (dye:cell suspension) to dye the cells (modified from the method used by Feng et al. (2014)). Total and non-viable cell counts of 10 photomicrographs were performed using the software CellC (Selinummi et al., 2005). A 5% error was estimated for viability quantification of each photomicrograph based on the propagation of counting error through calculations of average viability of triplicate slides. The surface integrity of the cells was then investigated visually with fluorescence microscopy to determine whether non-viable cells were intact or not. Intact cells were defined as those cells that maintained their shape with no visible ruptures when viewed at $1000\times$ via fluorescence microscopy.

2.2.6 Potentiometric modeling

We used a non-electrostatic surface complexation model (NE-SCM) to describe the cell surface protonation. A generic surface protonation reaction can be describe by a balanced chemical equation as illustrated in Equation 2.2, where $R - L_i^-$ is ligand i on the cell surface.

The total concentration of deprotonated sites on the surface is constrained by Equation 2.3,

$$R - L_i^- + H^+ \rightarrow R - L_i H \tag{2.2}$$

$$\sum [R - L_i^-] = \sum_1^i \frac{[R - L_i]_{tot}}{1 + \gamma_{H^+} \times [H^+] \times K_i} \tag{2.3}$$

where γ_{H^+} is the activity coefficient of protons in solution calculated using the Davies equation, and K_i is the stability constant defining the protonation of ligand i. The moles of protons adsorbed onto the cell surface normalized to biomass (m_s) is defined by Equation 2.4, where C_a and C_b are the total concentration of acid and base, respectively, added to the titrand, and [H^+] and [OH^-] are titrand concentrations calculated from the pH. This description of protons adsorbed onto the cell surface is defined relative to a zero state that is the pH of immersion or initial surface protonation state for each titration. The initial surface protonation state (T_H°) is defined by Equation 2.5, where T_H represents the mass balance for total proton concentration in the system (see Westall et al. (1995) and Fein et al. (2005) for further discussion).

$$H^+_{consumed} = (C_a - C_b - [H^+] + [OH^-])/m_s \tag{2.4}$$

$$T_H = T_{H^0} + (C_a - C_b) \tag{2.5}$$

Site concentrations and stability constants were derived with best fit models over the pH range 10 to 4. Best fit models were produced by non-linear least squares fitting of cell-proton adsorption (C_a and C_b) with the Newton-Raphson method. For each experiment,

we began with a single ligand model and added reactions as necessary so that the model would best represent the data, as determined with *F*-tests. The *F*-test determines statistical improvement of a more complex model compared to a simpler one by using the degrees of freedom and the sum of squares of those models. Parameters from all models at each ionic strength were averaged to produce a global model at each ionic strength.

2.2.7 Calorimetric modeling

Enthalpies of protonation (ΔH_{HL_i}) are related to total heat produced, $Q_{corr,v}$, by the change in the number of moles of protonated sites ($\Delta n^v_{HL_i}$) with each step of the titration as described by equation 2.6.

$$\sum Q_{corr,v} = \sum \Delta H_{HL_i} \times \sum \Delta n^v_{HL_i} \tag{2.6}$$

$\Delta n^v_{HL_i}$ values are calculated using the SCMs, simultaneous pH measurements, and volumes of acid added. These $\Delta n^v_{HL_i}$ values are used as independent variables in equation 2.6. We derive enthalpies of protonation by minimizing the difference between corrected heats and calculated heats with non-linear optimization. 1σ errors were calculated from the covariance matrix.

2.3 Results

2.3.1 Titration data

Potentiometric data

Figure 2.1 illustrates the buffering intensity (described by Equation 2.7) of CN32 potentiometric titrations. Non-zero buffering intensity is observed across the pH range investigated. At all ionic strengths, a buffering minimum is revealed around pH 8 and a buffering maximum is evident between pH 9 and 10. The medium ionic strength buffering intensity around circumneutral pH and high pH is substantially greater than the buffering intensity for low and high ionic strength. Around pH 5, buffering intensity increases for all ionic strengths compared to circumneutral pH. Reversibility titrations (closed symbols) exhibit similar buffering intensity to initial titrations. Difficulties in calculating slopes at the edges of the datasets caused increased scattering in the buffering intensities at the pH extremes.

$$\frac{d(\sum[R - L_i^-])}{d(pH)} \tag{2.7}$$

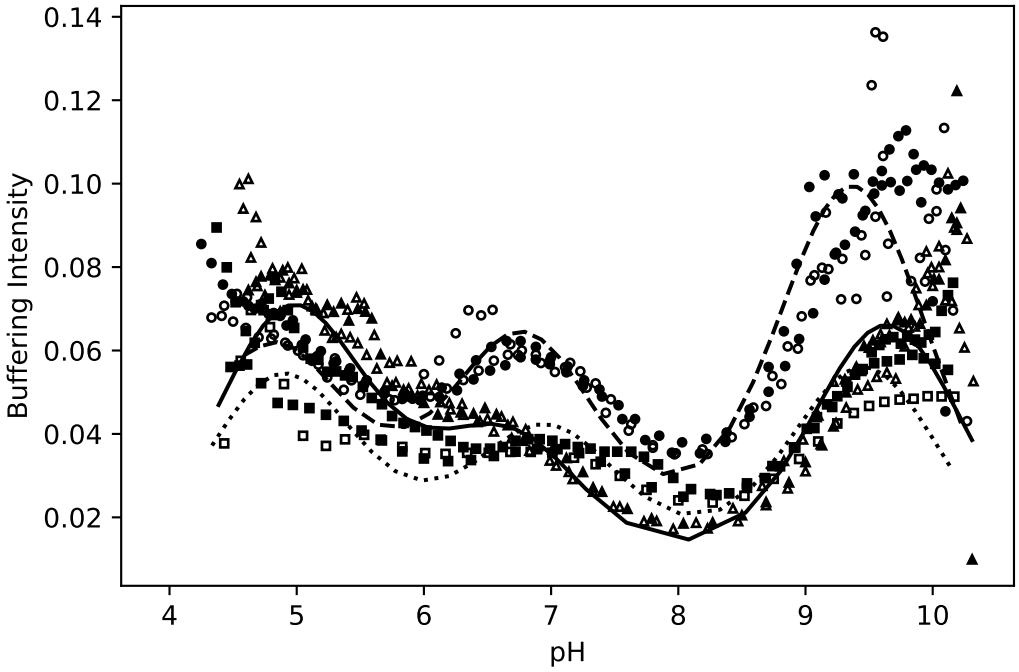

Figure 2.1: Buffering intensity of potentiometric titrations at low (open and closed squares), medium (open and closed circles), and high ionic strengths (open and closed triangles). Predicted buffering intensity shown for average titration conditions using the surface complexation models described in Table 2.1 for low (dotted curve), medium (dashed curve) and high (solid curve) ionic strength.

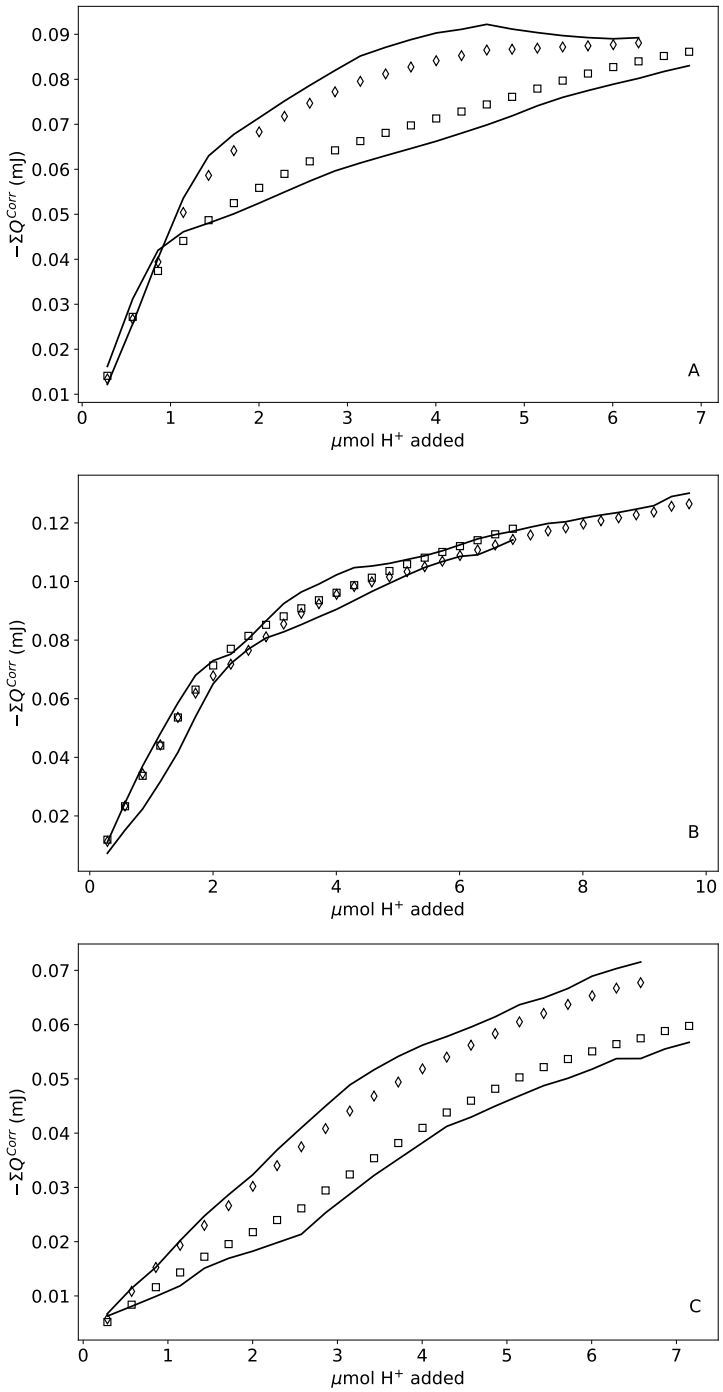

Figure 2.2: ITC results at each ionic strength with the curves corresponding to the 3-site model fit described in Table 2.1. Squares and diamonds are separate ITC experiments. A is low ionic strength, B is medium ionic strength, and C is high ionic strength.

Titration calorimetry data

Figure 2.2 (A – C) illustrates the corrected cumulative heats of protonation as a function of pH, across the same range of ionic strength as the potentiometric titrations. Overall, the cumulative heat evolved increased with increasing additions of acid. The heat per injection became less exothermic once about 1 – 2 μmoles of H^+ was added at low ionic strength. At higher ionic strength, cumulative heat evolved became less exothermic after about 2 – 4 μmoles of protons were added. The total heat produced varied with ionic strength from about 0.06 J to 0.12 J with the maximum total heat produced in suspension at medium ionic strength. These data illustrate that the total enthalpy of protonation for CN32 is exothermic. To establish how that total heat is divided between functional groups, we applied the surface complexation models to these data and derived enthalpies of protonation from Equation 2.6.

Table 2.1: Surface complexation model parameters and thermodynamic potentials for the 3-site model at low, medium, and high ionic strengths. Changes in equilibrium constants of protonation (ΔK) reflect the difference between stability constants at 20°C and 45°C, as determined with Equation 2.8. Standard error is reported.

IS (M)	Site	log(K)	[C] (μmol/g)	ΔG (kJ/mol)	ΔH (kJ/mol)	ΔS (J/molK^{-1})	$\lvert\Delta K\rvert$
0.02 - 0.04	$L1$	4.88 ± 0.05	93 ± 5	-27.85 ± 0.28	-7.03 ± 1.21	69.8 ± 4.2	0.10
	$L2$	6.97 ± 0.05	70 ± 1	-39.74 ± 0.28	-13.70 ± 1.48	87.4 ± 5.1	0.19
	$L3$	9.46 ± 0.03	97 ± 5	-53.96 ± 0.16	-60.38 ± 1.82	-21.5 ± 6.1	0.85
0.11 - 0.13	$L1$	4.79 ± 0.07	104 ± 3	-27.35 ± 0.39	-7.92 ± 1.51	65.2 ± 5.2	0.11
	$L2$	6.78 ± 0.08	107 ± 2	-38.69 ± 0.43	-13.98 ± 1.11	82.9 ± 4.0	0.20
	$L3$	9.37 ± 0.06	172 ± 9	-53.43 ± 0.34	-47.87 ± 1.10	18.7 ± 3.9	0.67
0.51 - 0.53	$L1$	4.95 ± 0.03	119 ± 2	-28.26 ± 0.17	-11.09 ± 0.75	57.6 ± 2.6	0.16
	$L2$	6.69 ± 0.03	64 ± 1	-38.18 ± 0.19	-11.10 ± 1.37	90.9 ± 4.6	0.16
	$L3$	9.64 ± 0.02	115 ± 5	-54.98 ± 0.12	-22.51 ± 1.25	109.0 ± 4.2	0.32

Titration modeling

Potentiometric titration data was modeled using 1 – 5 discrete sites and *F*-tests to determine statistical improvement of model fits for each dataset. The 1- and 2-site models under-predicted proton adsorption between pH 4 and 5 and pH 7 and 10. The 3-site models produced a statistically better fit to the data than the one and two site models, and a significantly worse fit than the 4-site models for all but two of the titrations (one at low ionic strength and one at medium ionic strength). Table 2.1 reports 3-site model results (4-site model results are shown in Supplementary Materials). A 5-site model failed to converge to our data. Statistical data can be found in the Supplementary Materials.

Applying surface complexation models to the ITC data using Equation 2.6 produced contrasting results to the potentiometric titration data. The 3-site model produced the best fit to each of the ITC datasets across ionic strengths. Thermodynamic parameters are presented in Table 2.1 and in the Supplementary Materials. Figure 2.2 illustrates the fit of Equation 2.6 to $Q_{corr,v}$ using the 3-site model. The 1-site model vastly under- and over-predicted $Q_{corr,v}$. The 2-site model was a substantial improvement over the 1-site model but was not significantly better than the 3-site model. While the 4-site model was an improvement over the 1- and 2-site models, the residual sum of squares was higher than and statistically significant from the 3-site model. The inferior fit of the 4-site model was clearly reflected in the ΔH errors, where the 4-site model produced consistently larger errors, with some exceeding the estimated value. An unreasonable enthalpy of protonation was obtained for *L*3 when 4 sites are applied at high ionic strength. This produced an endothermic enthalpy of protonation, which is unlikely given the potential structures (e.g., phosphoryl) expected on the cell envelope with a log(K) within the range observed for *L*3 (7.00 – 8.29).

The enthalpies of protonation for each site in the 3-site models were entirely exothermic, with some variation between ionic strengths (Table 2.1). Protonation enthalpies for each site, regardless of ionic strength, were positively correlated with its ΔG, with *L*3 be-

ing the most exothermic. Between ionic strengths, this trend was also observed for $L2$, where changes in a ΔG were directly proportional to changes in ΔH. The correlation is lost, however, for $L3$, where an increase in ΔG with ionic strength corresponds to a decrease in protonation enthalpy.

2.3.2 FTIR data

Figure 2.3 shows the spectra of CN32 at medium ionic strength from pH 4 to 9.4. Medium ionic strength was chosen due to a lack of effect of ionic strength on FTIR spectra (see Supplementary Materials). Over the entire pH range, there are peaks known to be associated with microbial surfaces centered at 970, 990, 1084, 1230, 1396, 1450, 1544, and 1637 cm^{-1} (Kamnev et al., 1999; Jiang et al., 2004; Parikh & Chorover, 2006; Kenney et al., 2018). An additional peak with a much reduced intensity is also present at 1736 cm^{-1}. Peak assignments are summarized in Table 2.2. Peak position was largely consistent across pH values, while some peak heights decreased slightly with increased pH. That change in height is evident in peaks 1637, 1230, and 1084 cm^{-1} (IR bands *b*, *f*, and *h*). The peak centered around 1396 cm^{-1} showed an opposite trend as peak height increased with increasing pH.

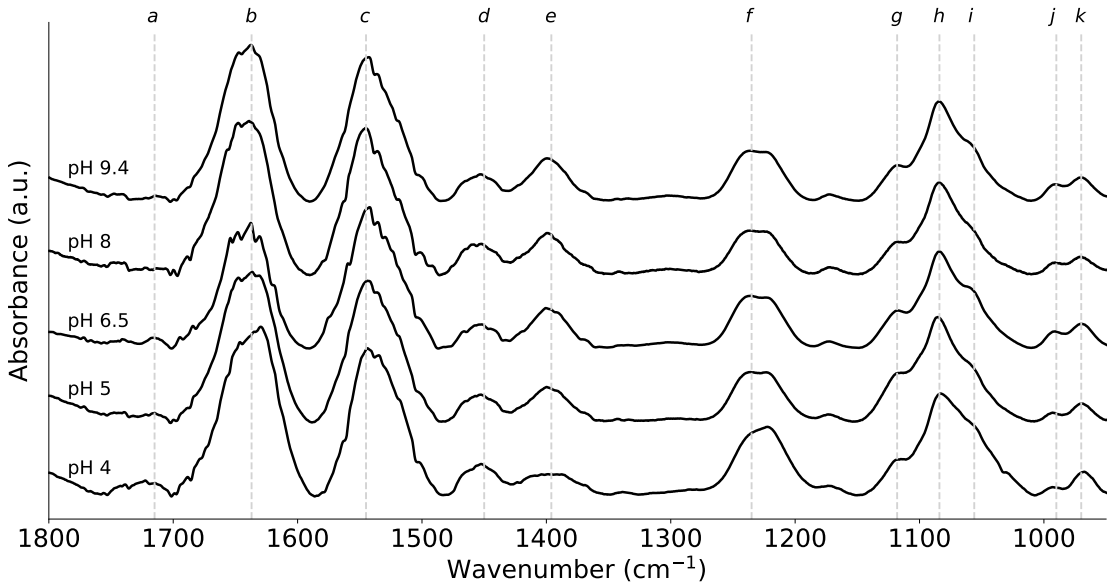

Figure 2.3: FTIR spectra normalized to the area under the amide II band (1548 cm^{-1}) of CN32 at medium ionic strength with varied pH. Approximate band locations indicated with vertical dashed lines.

Table 2.2: Assignments for the major vibrational bands, shown in Figure 2.3, as compiled from Kamnev et al. (1999), Jiang et al. (2004), Parikh & Chorover (2006), and Kenney et al. (2018). δ = bending, ν = stretching, s = symmetrical, as = asymmetrical

IR band	Wavenumber (cm^{-1})	Assignment
a	1736	ν C=O in protonated carboxylic acid groups
b	1637	ν C=O in amide I
c	1544	δ N−H and ν C−N in amide II
d	1450	Asymmetric CH_2 scissoring in lipids or proteins
e	1396	ν_s COO^- in carboxyl groups
f	1230	ν_{as} P=O in a protonated polyphosphate
g	1118	ν_s C−C and C−O−C and ν_{as} P−O−C in phosphates, phosphodiesters, and carbohydrates
h	1084	P−OH vibrations in a protonated polyphosphate
i	1061	Carbohydrates and phospholipid vibrational modes
j	993	C−OH and C−C vibrations in polysaccharides and alcohols
k	972	ν_s P−OH

2.3.3 Cell viability analysis

CN32 was at least partially viable throughout the pH range examined (see Supplemental Materials). The majority of cells, however, became non-viable over the course of the initial and reversibility titrations (decreasing in viability from 77% to 6%). Viability was not statistically affected by the initial suspension of cells and subsequent pH adjustment to ca. pH 10. Viability decreased by a factor of 1.5 after the initial titration, and by an additional factor of 8.5 following the reversibility titration. These two reductions in viability were statistically significant at 95% confidence. While a less oxidative electrolyte, such as NaCl, may have imparted a smaller change in viability, $NaClO_4$ was selected to support

future studies with metal adsorption onto CN32 in an electrolyte with less complexation potential. In addition, despite using $NaClO_4$, cells appear nearly completely intact despite a loss in membrane integrity, as shown by the staining. This suggests that cell fragments, or the exposure of internal cellular components, did not substantially contribute to proton adsorption.

2.4 Discussion

2.4.1 Thermodynamic constraints on surface complexation modeling

Quantifying bacterial surface reactivity with surface complexation modeling results in parameters that are dependent on the modeling approach. Additionally, the range of pH values included in the modeled titrations will directly impact the number of discrete sites needed to optimize the fit between model and data. When SCMs are applied to ITC data, we can further constrain the number of sites based on the magnitude and the error of the enthalpies of protonation in addition to the reasonableness of the derived parameters. Specifically, we define models that yield both reasonable enthalpies of protonation for known bacterial surface sites and minimal errors on those values as enthalpically constrained models. Importantly, the number of sites in an enthalpically constrained model may differ from the number of sites in an SCM only constrained by proton adsorption data. Our 3-site enthalpically-constrained model demonstrates this difference.

Typically, when modeling the consumption of protons in titration data, increasing the number of available discrete binding sites produces a better fit between model and data, provided that there is some degree of misfit to the model with fewer sites. This was evident in eight of our ten datasets; increasing the SCM from 3 to 4 sites by adding additional site with a log(K) value below 7 yielded a better fit to our data. However, increasing the total number of sites from 4 to 5 over-constrained the model, most likely because of the pH range considered in our experiments (pH 4 to 10) did not possess enough distinct foci of buffering intensity; however, this range did ensure cells remained at least partly viable for reversibility titrations. CN32 titration datasets from a broader pH range can be modeled with 5 sites as shown by Smith & Ferris (2003) and Sokolov et al. (2001). The typically clear improvements in SCM fits to proton adsorption mass balance data (Equation 2.5) by increasing sites, when appropriate for the pH range of the data, may not be mirrored when applying the SCM to ITC data. Derivation of site-specific enthalpies of protonation uses SCM predictions of the extent of protonation with each step in the titration. The more sites

that are involved in a model, the more proton adsorption is partitioned between sites, and the smaller $\Delta n^{v}_{HL_i}$ values become. This can result in $Q_{corr,v}$ partitioning beyond what can be constrained by the calorimetric data and yield both unreasonable enthalpies of protonation and/or errors on those values. Deriving site-specific enthalpies of protonation from ITC data provides an additional test for SCMs and determines the limits of how many sites can be resolved based on two types of data. From here forward, we will evaluate CN32 surface reactivity based on the enthalpically-constrained 3-site model.

The formation constants and enthalpies and entropies of protonation for each site fell within ranges previously observed for gram negative bacteria. The log(K) and ΔS values of $L1$ (4.79 – 4.95 and 57.6 – 69.8 J/molK^{-1}) are consistent with the protonation of a carboxylic acid group (DeRobertis et al., 1999; Goldberg et al., 2002; Kitano et al., 2006). While the ΔH values for $L1$ (-7.03 – -11.09 kJ/mol) are more exothermic than some observations of carboxyl protonation enthalpies (Christensen et al., 1967; Goldberg et al., 2002; Kitano et al., 2006), they are within the ranges observed for multicarboxyl compounds, such as oxalate and phthalate (Goldberg et al., 2002) and aminopolycarboxyates like EDTAPA (Danil De Namor & Pacheco Tanaka, 1998). For $L2$, our measurements of the enthalpy and entropy of protonation are within the range of parameters previously observed for the protonation of polyphosphates (Sawada et al., 1993; Nash et al., 1995). Specifically, $L2$ has ΔH values (-11.10 – -13.98 kJ/mol) and ΔS values (82.9 – 90.9 J/molK^{-1}) very similar to those for the protonation of a P-O group in a polyphosphate, as measured by De Stefano et al. (2004). Lastly, our observations of $L3$, as summarized in Table 2.1, are consistent with thermodynamic parameters of amines. De Robertis et al. (1991) previously observed similar changes in aspartic acid where the amine group is near carboxyl groups. Moreover, $L3$ exhibits enthalpy-entropy compensation with ionic strength, where a reduction in exothermy correlates with an increase in entropy, as seen in amines previously (De Robertis et al., 1991; Bretti et al., 2014). In all, our thermodynamic measurements suggest that the three acidic sites on CN32 are predominantly carboxyl, polyphosphate, and amine moieties.

2.4.2 *Temperature dependence on surface protonation*

In addition to providing constraints on site identity and the coordination environment more broadly, protonation enthalpies can be used to estimate temperature impacts on log(K) values. We can estimate temperature dependence using enthalpies of protonation, protonation constants, absolute temperature (T), and the gas constant (R) in the van 't Hoff equation (Equation 2.8).

$$\frac{\delta}{\delta T} lnK_{eq} = \frac{\Delta H}{RT^2} \tag{2.8}$$

Previous work has shown that enthalpies of microbial surface protonation change little from 25 to 75 °C (Gorman-Lewis, 2011). This supports the assumption that relative heat capacities of the products and reactants are zero for the protonation reactions (such that $\Delta C_P = 0$). This method is preferable to performing potentiometric titrations over a range of temperatures, as errors on protonation and stability constants when performing titration and adsorption experiments with biomass suspensions at elevated temperatures can often be large (Wightman et al., 2001; Ginn & Fein, 2009).

S. putrefaciens studies are typically performed at 30°C, though the genus exhibits a range in temperature tolerance, with growth possible down to 5°C (Hau & Gralnick, 2007). We used the Van't Hoff equation to calculate the change in protonation constants from 20°C to 45°C (Table 2.1). This range includes the most broadly accepted range of growth temperatures for mesophilic bacteria (Willey et al., 2008). As expected, for all sites and all ionic strengths, this predicts a decrease in the log(K) values with temperature. For $L1$ and $L2$ at each ionic strength, the change was less that 0.3 log units, suggesting a minimal dependence of the acidity constants of those sites on temperature. At low and medium ionic strength, $L3$ changed more appreciably over the range of temperature examined, with a change of more than 0.5 log units for each. While this effect was lost somewhat at high ionic strength, $L3$ still had the largest temperature effect at that ionic strength. This in-

dicates that the acidity constant for Site 3 is dependent on temperature, distinguishing it from the other sites. The fact that this impact decreases with ionic strength may be due to the conformational changes suggested by the entropy of protonation for *L*3, which increased from a negative value at low ionic strength (-21.5 J/molK^{-1}) to a large positive value at high ionic strength (109.0 J/molK^{-1}, see discussion below). The structure of this conformational change, and why it was only observed at *L*3, is beyond the scope of this study. However, as demonstrated here, conformational changes are important to fully understanding the reactivity of microbial envelopes.

2.4.3 Comparison to previous work

When putting the work presented here in the context of previous studies, it is important to consider both the experimental methods and modeling approach. Sokolov et al. (2001) and Smith & Ferris (2003) grew and harvested CN32 biomass using similar methods to this work. However, the experimental pH range over which they titrated CN32 was larger and their modeling approach was different. They applied a linear programming method and a Fully Optimized ContinUouS (FOCUS) pK_a spectrum method, respectively. These approaches fix log(K) values typically from the minimum and maximum of the pH range of the titrations at intervals of 0.2 units while the site concentrations remain as unknowns. This approach can avoid convergence issues when fitting both the acidity constants and site concentrations, which was the approach used in the current work (Brassard et al., 1990; Cox et al., 1999). Given the pH range of their work and modeling approaches, a 5-site SCM is a reasonable outcome. Despite the differences between our approach and previous work, meaningful comparisons can still me made.

When we compare log(K) values for our medium ionic strength data to the models of both Sokolov et al. (2001) and Smith & Ferris (2003) (also done at 0.1 M), our values are within approximately a half log unit of those observed for sites 2, 3, and 5. Similarly, the total site concentration in dry weight (calculated using a 4:1 conversion of wet weight to

dry weight; see Supplemental Materials) is 1510 ± 56 μmole/g, which is consistent with the values of Sokolov et al. (2001) (1770 μmole/g) and Smith & Ferris (2003) (1590 μmole/g). This suggests all three modeling methods are capturing the CN32 surface reactivity regardless of the partitioning of those sites based on log(K) values. In order to evaluate if a particular approach more accurately captures structural character (i.e., potential coordination environment and nearest neighbor functional groups) of the CN32 surface, the models need to be applied to another type of data that is more sensitive to the surrounding structural character of surface functional groups.

We can apply the surface complexation models from Sokolov et al. (2001) and Smith & Ferris (2003) to our ITC data, just as we have done for our own SCMs. This allows us to quantitatively evaluate the ability of those 5-site models to capture the heat and entropy produced from protonation. The model by Sokolov et al. (2001) (see Supplemental Materials) produced site-specific enthalpies of protonation that were both reasonable (e.g., -3.1 kJ/mol) and unreasonable (e.g., -165 kJ/mol) for microbial functional groups. Furthermore, the errors for those enthalpies of protonation (e.g., 14.2 kJ/mol) indicate that the parameters are not accurately describing reactivity. The model by Smith & Ferris (2003) also produced unreasonable enthalpies of protonation (e.g., -108 kJ/mol) and errors. Similarly, the entropies of protonation derived from these ΔH and log(K) values included values exceeding the range expected for microbial surfaces (e.g., -171 J/molK^{-1}) and uniformly high errors (e.g., 122 J/molK^{-1}). The inability of these models to produce reasonable enthalpies and entropies of protonation suggests that the inclusion of five discrete sites represents an overly partitioned state of surface reactivity. The relatively small errors on the thermodynamic parameters observed in this work, in constrast, indicate that those parameters are reasonably well constrained. This may indicate that although surface reactivity can be captured by additional sites with the linear programming and FOCUS methods, the SCMs may not reflect the intricacies of binding site structure that are elucidated with entropies and enthalpies of protonation.

2.4.4 *Ionic strength impacts*

It has recently become well established that the ionic environment directly alters the structure of the LPS on the outer membrane of gram-negative bacteria (Silhavy et al., 2010; Simpson & Trent, 2019; Rahnamoun et al., 2020). For example, cations such as Ca^{2+} cause conformational changes to LPS molecules, such as the transfer of the *O*-ploysaccharide toward the core oligosaccharide, as measured in isolated LPS molecules suspended in 5 mM HEPES and 100 mM KCl at pH 7.4 (Schneck et al., 2009). Consistent between these studies is that divalent cations result in more significant changes to LPS structure than monovalent cations, including higher concentrations of ionic bridges and steric barriers (Rahnamoun et al., 2020). Monovalent cations, in contrast, appear to have a weaker effect on LPS, manifested primarily in charge shielding rather than bridging or steric barriers. Still, as observed by Rahnamoun et al. (2020), monovalent cations with smaller radii (e.g., Na^+ versus K^+) result in increased packing of LPS (i.e., closer physical association of LPS molecules), with some degree of ionic bridging. Broadly, these studies have provided critical initial measurements in understanding how the ionic environment affects LPS structure.

The work by Rahnamoun et al. (2020) highlights important details regarding bacterial surface conformation which can aid in the interpretation our ionic strength comparisons. We performed an analysis of variance along with a Tukey post-hoc test on the average parameters in Table 2.1 to determine if these impacts on LPS were evident in the SCM results across the ionic strengths investigated. All site concentrations ($C1$ - $C3$) were significantly affected by ionic strength at 95% confidence, although those changes did not follow an overall trend. $L1$ concentration increased with ionic strength, while the concentrations of $L2$ and $L3$ peaked at medium ionic strength. As ionic strength changes, it is expected that LPS packing and ionic bridging will change. We attribute the changes observed in site concentrations to these known conformational changes in the cell envelope with changing cation concentrations described by Rahnamoun et al. (2020), which will alter the number

of titratable sites.

Changes in enthalpies and entropies of protonation along with log(K) values may reveal more structural details about how these binding site environments change with ionic strength. The analysis of variance showed that the log(K) of site 3 increased significantly (95% confidence) at high ionic strength but was insensitive to change from low to medium ionic strength. Protonation enthalpies and entropies of $L3$ were significantly different (95% confidence) at high ionic strength compared to medium and low ionic strengths. The fact that only site 3 was affected by ionic strength in terms of all three thermodynamic parameters (log(K), ΔH, and ΔS) suggests that $L3$ constitutes a binding environment that is more sensitive to LPS conformational changes than $L1$ and $L2$. Indeed, enthalpies and entropies of protonation and stability constants for amine-containing ligands, the site identity assigned to $L3$ (*vida supra*), appear to be more directly affected by ionic strength when part of a multidentate ligand (De Stefano et al., 2005) than as a monoamine (De Robertis et al., 1991).

The sensitivity of aqueous entropies of association to hydration make it an excellent parameter to use to learn more about why $L3$ is more sensitive to ionic strength than $L1$ or $L2$. Entropies of protonation for $L3$ decreased with decreasing electrolyte concentration, which indicates an increase in order around $L3$. It is well established that an increase in order of aqueous systems (a decrease in the entropy of association) is a result of hydrogen bonding between ligands and the ordering of water molecules along with statistical effects (Frank & Evans, 1945; Edward J. King, 1965; Irudayam & Henchman, 2009; Ahmad et al., 2014). This decrease in entropy of protonation to negative values of a postulated amine-containing ligand as seen in this work has been previously observed in polyamines. Barbucci et al. (1981) found low and negative protonation entropies of amine protonation. They attributed this to the influence of nearest neighbor effects on hydrogen bonding between the protonated site and water molecules (Barbucci & Vacca, 1974; Barbucci & Barone, 1979). The fact that a negative protonation entropy was only observed in our low ionic strength data is consis-

tent with this reasoning. Surface potential increases as electrolyte concentration decreases, allowing the surface to exert a larger effect on the bulk solution and increasing order (Marshall et al., 1971; Dzombak & Morel, 1990; Busalmen & De Sánchez, 2001). This effect is lost at high ionic strength, where surface potential decreases and LPS packing increases.

The contrasting effects of ionic strength on the three sites identified here are consistent with the current understanding of how ionic strength impacts bacterial protonation properties. Martinez et al. (2002) quantified nonspecific interactions between the bacterial surface and background electrolyte for a gram positive (*Bacillus subtilis*) and a gram negative (*Escherichia coli*) bacterium. Specific effects of ionic strength were observed both for log(K) values and site concentrations when analyzed with the FOCUS model (a continuous log(K) affinity distribution method) and Donnan potential. The influence of ionic strength on site chemistry of the gram positive *Bacillus subtilis* was reevaluated by Fein et al. (2005). Their analysis included a more exhaustive application of modeling approaches for potentiometric data and suggest the effect of ionic strength is at best smaller than observed by Martinez et al. (2002), or not present. Indeed, as noted by Fein et al. (2005), and others (e.g., Plette et al., 1995; Daughney & Fein, 1998; Tourney & Ngwenya, 2010) the effect of ionic strength on surface reactivity with protons may be very small. A slightly different conclusion was reached in a subsequent analysis by Borrok & Fein (2005) that included two gram negative bacteria, where a moderate effect of ionic strength on protonation properties was observed. The variations we observed in the effect of ionic strength on log(K) values are consistent with the variegated effects of ionic strength on bacterial protonation properties observed to date. That is, for the log(K) values of $L1$ and $L2$, we see evidence for the very minor effects similar to those observed by Fein et al. (1997), but in $K3$ and each of the site concentrations, we see more substantial correlation of ionic strength change with functional group changes, as suggested by Martinez et al. (2002).

It is likely that conformational changes in the cell envelope impact surface site concentrations. However, our present understanding of conformation changes is very limited.

This is compounded by the inability of electrostatic models to satisfactorily describe protonation behavior at various ionic strengths. This implies that these conformational changes cannot be satisfactorily predicted, which ultimately suggests that the best approach to include these conformational effects in SCMs is by using apparent constants at appropriate ionic strengths.

2.4.5 FTIR

Spectroscopic data can aid in the identification of functional groups and provide complementary lines of evidence regarding the reactivity of the cell surface. For CN32, our FTIR data are consistent with vibrational modes in compounds including amides, carboxyls, phosphates, and carbohydrates (Table 2.2). In contrast to observations by Jiang et al. (2004), the intensity ratio of the Amide I to II bands decreases with an increase in pH from pH 4 – 6, and increases from pH 6 – 9. The addition of a new peak in the same energy region, namely C=O stretching in a protonated carboxylic acid group at 1736 cm^{-1}, could impact this ratio. Alternatively, it may suggest that there are conformational changes to the protein secondary structure that vary with pH (Jiang et al., 2004; Parikh & Chorover, 2006).

Changes to peak intensity are the main impacts pH had on spectra in this work. An internal standard would allow for a quantitative assessment of site concentration from peak intensity. Lacking that, the change in intensity can be used to qualitatively infer changes in concentration of the sites. Specifically, peak *h* decreases in intensity with pH. Similarly, the intensity of peak *f* decreases from pH 4 to 5. This implies the corresponding functional groups decrease in concentration with pH. Peak *e* has the opposite trend, where intensity and concentration increase with pH.

The confidence with which the bonding environment can be described on the cell envelope directly depends on identifying constituent peaks within these spectral data, and is correspondingly limited by peak overlap. Specifically, the region from approximately 1000 – 1150 cm^{-1} contains a variety of potential structures. Additionally, the amide II band is

a result of both N-H and N-C vibrations. Whether both signals are observed, and what their respective intensities were, however, was not clear from this initial spectral analysis. To establish which structures contribute to these regions of broad peaks where additional vibrational bands are likely, we performed Gaussian deconvolution on the spectra. Those deconvolved peak assignments are summarized in Table 2.3, and the corresponding spectra can be found in the Supplementary Materials.

Table 2.3: Peak assignments for the deconvolution analysis. IR Bands refer to bands in the deconvolved region that were previously identified (see Table 2.2). Spectra are shown in the Supplementary Materials. 1σ errors of peak location ranged from 0.1 – 3 cm^{-1}, with an average of 0.6 cm^{-1} (see Supplementary Materials for individual peak errors). δ = bending, ν = stretching, s = symmetrical, as = asymmetrical

IR Band(s)/pH	Wavenumber	Assignment	Reference
c (pH 4)	1499	δ_s NH_3 / ν_s C-N-C=O	Rosado et al. (1998) / Ji et al. (2020)
c	1513	δ_s NH_3 / ν_s C=O	Rosado et al. (1998) / Ji et al. (2020)
c	1532	δ_s NH_3	Parker (2013)
c	1550	δ_s NH_3	Parker (2013)
c	1558	δ_s NH_3	Parker (2013)
c	1567	δ_{as} NH_3	Parker (2013)
c (pH 9)	1498	δ_s NH_3 / ν_s C-N-C=O	Rosado et al. (1998) / Ji et al. (2020)
c	1524	δ_s NH_3 / ν_s C=O	Parker (2013) / Ji et al. (2020)
c	1535	δ_s NH_3	Parker (2013)
c	1543	δ_s NH_3	Parker (2013)
c	1548	δ_s NH_3	Parker (2013)
c	1570	δ_{as} NH_3	Parker (2013)
g, *h*, *i* (pH 4)	1026	δ C-O	Ibrahim et al. (2006)
g, *h*, *i*	1054	δ C-O	Ibrahim et al. (2006)
g, *h*, *i*	1064	δ_{as} P-O in PO_3^{2-}	Zenobi et al. (2008)
g, *h*, *i*	1086	δ_s P-O in HPO_3^{-}	Zenobi et al. (2008)
g, *h*, *i*	1102	δ_{as} P-O in PO_3^{2-}	Zenobi et al. (2008)
g, *h*, *i*	1117	δ C-O	Ibrahim et al. (2006)
g, *h*, *i* (pH 9)	1031	δ C-O	Ibrahim et al. (2006)
g, *h*, *i*	1056	δ C-O	Ibrahim et al. (2006)
g, *h*, *i*	1069	δ_{as} P-O in PO_3^{2-}	Zenobi et al. (2008)
g, *h*, *i*	1086	δ_s P-O in HPO_3^{2-}	Zenobi et al. (2008)
g, *h*, *i*	1101	δ_{as} P-O in PO_3^{2-}	Zenobi et al. (2008)
g, *h*, *i*	1118	δ C-O	Ibrahim et al. (2006)

This more detailed analysis of the FTIR spectra also allowed us to examine any effects resulting from pH not readily observable from the original spectral analysis. For both regions examined, this showed only a very minor impact of pH on surface functional groups. In the deconvolved region containing peak *c*, there is a shift of one peak from 1513 at pH 4 to 1524 at pH 9, but these are both consistent with symmetric bending of an NH_3 group. In the deconvolved region containing peaks $g/h/i$, an increase in the intensity of peaks at 1101 cm^{-1} and 1053 cm^{-1} with pH is evident. A decrease in the intensity of the peak at 1069 cm^{-1} is illustrated as well. Overall, however, the peak assignments remain consistent from pH 4 to pH 9.

2.4.6 Viability impacts

A key step in inferring surficial reactivity from titration data is the assumption that protonation reactions are predominantly only occurring on the cell surface. This is in contrast to reactions occurring on cell fragments that have exposed internal proton active sites and/or leakage of proton-ionizable molecules from non-viable cells. The most common method of evaluating cell viability is through differential staining of cells (e.g., Feng et al., 2014). The reactivities of viable versus non-viable cells have consistently been shown to differ (see the compilation of data provided by Javanbakht et al. (2014) and Torres (2020)). Cells that stain as non-viable have ruptured membranes that allow proton-ionizable chemicals to leak from inside the cell, which has the potential to modify the proton mass balance calculation (Equations 2.4 and 2.5) if sufficient leakage occurs. This is supported by the quantifiable reactivity of non-cellular biomass produced from bacteria (Torres, 2020). To assess if cell fragmentation influences proton mass balance, an examination of cell morphology is needed.

We used viability staining, described above, and reversibility titrations to assess potential leakage of proton-ionizable chemicals from the washed, metabolically inactive cells. A representative photomicrograph of non-viable CN32 cells in a suspension of $NaClO_4$

at pH 4 is provided in the Supplemental Materials. The observed loss of viability suggests that leakage of proton-ionizable molecules through compromised membranes was possible. In order for leakage to impact the titration data, the sensitivity of the titrations would have to be greater than the change to the proton mass balance equation. This means that there would have to be a significant difference in the proton mass balance between the initial, primarily viable, and the reversibility, primarily non-viable, titrations. The agreement between these titrations demonstrates that the titrations in this work were insensitive to leakage of proton ionizable chemicals. This suggests that addition of proton-ionizable molecules from within cells was not sufficiently high to be detected in the titrations.

2.5 Conclusions

The complementary datasets from SCMs and ITC provide new data on the binding environment on the CN32 cell envelope. FTIR data support the structural assignments of three predominant reactive sites on CN32. Deconvolution of the FTIR spectra provided an additional level of detail in our understanding of that surface structure, revealing the constituent peaks for two of the more complex spectral regions, along with the relative intensities of those bands. Our results indicate the presence of carboxyl, polyphosphate, and amine groups on CN32, with all site concentrations significantly affected by ionic strength. The amine group showed the greatest sensitivity to ionic strength, with changes to its thermodynamic properties consistent with conformational alterations.

More-complex electrolytes than were considered in this work, such as those with divalent cations, may have important effects on the protonation properties of microbial surfaces. Specifically, impacts of LPS packing, imparted by the electrolyte, on protonation parameters should be be investigated further. Additionally, more detailed analyses regarding the specific chemical alterations involved in conformational changes would further improve our ability to accurately describe the chemical structure of microbial envelopes across a range of geochemical conditions. Site concentrations may be more sensitive to electrolytes than stability constants of protonation. Our results show that these impacts are varied, and previous work on applying electrostatic models to cell envelope protonation have mixed results. Ultimately, the success of applications of surface complexation models of microbial envelopes to geochemical systems may depend on accurately accounting for electrolyte impacts. In all, this work helps to refine our understanding of the cell envelope of CN32 and the results are directly applicable to examining the interaction of those functional groups and reactive contaminants such as heavy metals.

Chapter 3

SURFACE COMPLEXATION OF U(VI) ONTO *SHEWANELLA PUTREFACIENS* CN32

Co-authored by Addien C. Wray and Drew Gorman-Lewis

Abstract

The adsorption of chemical species onto charged surfaces is central in regulating their interactions with and effects on *in situ* microorganisms. The specific adsorption of radionuclides onto bacterial surfaces has gained recent traction in the literature for its obvious remediation implications, but also for understanding microbial adaptations to toxic compounds. The adsorption of hexavalent uranium onto bacterial surfaces is important for microbes to adapt to high concentrations of heavy metals. In energy-limited systems, this ability can prove essential, as other metals are often comingled with U(VI) and the ability to withstand those toxic chemicals is necessary to obtain adequate nutrients and chemical energy. In this chapter, I present results obtained by constraining the U(VI) adsorptive potential of the same bacterium from Chapter 1, *Shewanella putrefaciens* CN32. I describe how four important variables impact the amount of U(VI) that gets adsorbed onto CN32: ionic strength, CO_2, pH, and the co-presence of other cations. By combining those measurements with chemical speciation models for U(VI) in each system, I describe the specific chemical reactions involved with that adsorption and, critically, the stability constants of those reactions. This allows for predictive statements to begin to be made about the ability of this bacterium to adsorb U(VI) under a variety of environmental conditions. Because each variable included would very likely be applicable to the chemical environments of exoplanets, this work is foundational in the application of surface complexation models to heavy metal-rich systems, which would allow us to better predict the actual habitability of

what may otherwise appear to be uninhabitable systems.

3.1 Introduction

Chemical interactions between metals and reactive surfaces is critical in regulating the transport of toxic compounds in the environment (Dzombak & Morel, 1990; Dube et al., 2001; Moon & Peacock, 2012; Zou et al., 2016; Ciffroy & Benedetti, 2018). Radionuclide adsorption onto bacterial surfaces is of particular concern given the widespread distribution of radionuclides from both anthropogenic and natural sources (e.g., Gorman-Lewis et al., 2005b; Anderson et al., 2007; Gorman-Lewis et al., 2013; Safonov et al., 2019; Lopez-Fernandez et al., 2018). Moreover, radionuclides present an important obstacle to environmental habitability, where otherwise favorable conditions are made inhospitable by their presence (Sitte et al., 2015; Boteva et al., 2016; Chen et al., 2021). Some microorganisms, however, are able to withstand that toxicity and, through their chemical interactions with radionuclides, alter the geochemical environment sufficiently for other taxa to survive (Newsome et al., 2014; Lopez-fernandez et al., 2020; Povedano-priego et al., 2022).

Uranium has been of particular interest given its high potential for mobility under oxidizing conditions, where the soluble U(VI) is the dominant oxidation state (Haas et al., 2001; Arnold et al., 2006; Alessi et al., 2012; Stylo et al., 2013). However, understanding interactions of uranyl ions (UO_2^{2+}) with bacterial surfaces is difficult because UO_2^{2+} readily forms highly soluble complexation products, dependent on *in situ* geochemical conditions (Stanley & Wilkin, 2019; Kalintsev et al., 2021). To date, there have been few investigations about how geochemical variables, such as the presence of CO_2 and divalent cations, alter the way UO_2^{2+} impacts bacterial surface reactivity. Quantifying that interaction requires a combined understanding of U(VI) speciation and microbial surface reactivity. As described below, our knowledge in this area has advanced significantly in recent years, but there remain key gaps that need to be addressed.

The geochemical environment determines the speciation of U(VI). For example, in an aqueous solution, the free uranyl ion remains dominant up to circumneutral pH, beyond which uranyl hydroxides form. As shown in Figure 3.1, when equilibrated with atmo-

spheric conditions (i.e., CO_2 partial pressure of $10^{-3.5}$ bar), the system yields uranyl-carbonate-hydroxide complexes in place of the uranyl hydroxides. The introduction of divalent cations into solution, like Ca^{2+} and Mg^{2+} (see Figure 3.2), similarly complex with UO_2^{2+} and form negatively charged ternary species (Dong & Brooks, 2006, 2008).

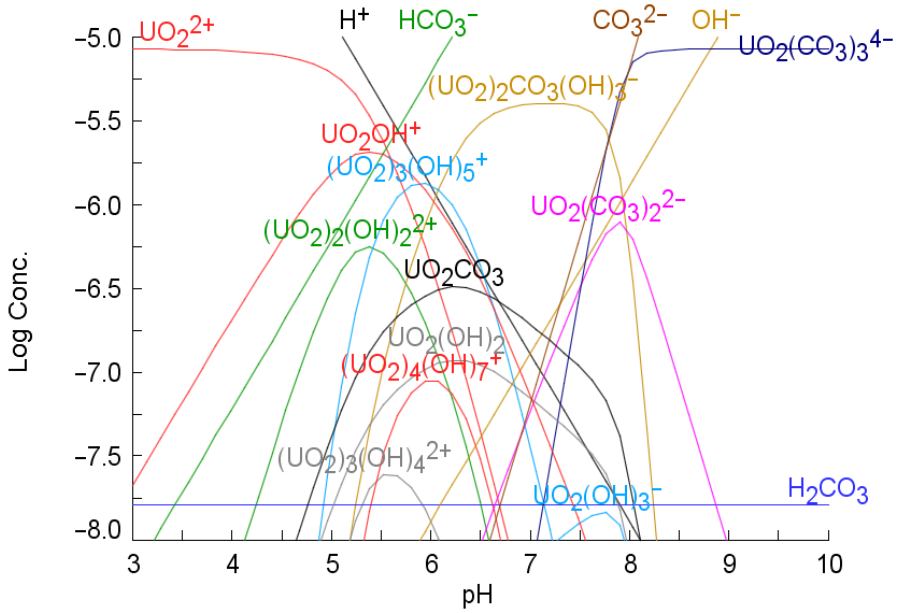

Figure 3.1: Speciation of U(VI) in water equilibrated with atmospheric CO_2.

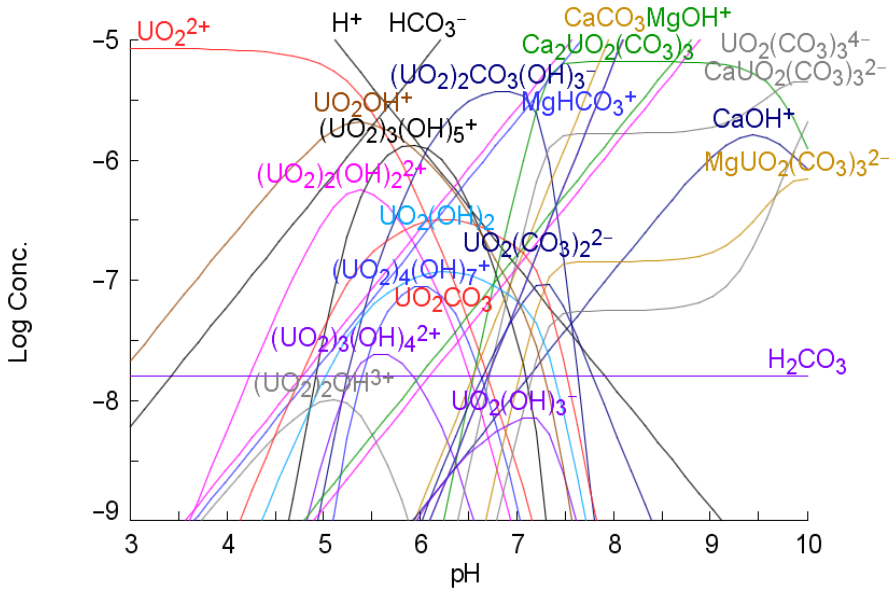

Figure 3.2: Speciation of U(VI) in water with 10 mM Ca^{2+} and Mg^{2+} and equilibrated with atmospheric CO_2.

The predominantly negatively charged uranyl complexes forming above circumneutral pH have interesting electrostatic implications for adsorption onto bacterial surfaces. Typically, cations interact with bacterial surfaces in this pH range. This is due to bacterial surfaces being dominated by negatively charged surface sites above pH 6 (Noda & Kanemasa, 1984; Wilson et al., 2001; Ayala-torres et al., 2014). Therefore, electrostatics predicts there should be no direct interaction between the surface and anionic U(VI) species, such as those formed at high pH. Yet previous work has repeatedly shown that uranyl complexes do interact, reversibly, with bacterial surfaces (Fowle et al., 2000; Haas et al., 2001; Sar & D'Souza, 2001; Gorman-Lewis et al., 2005a; Sheng et al., 2011; Sheng & Fein, 2013a). Interactions could be facilitated by ternary reactions, where a free cation bridges a functional group and a U(VI) complexation product (Kenney et al., 2017a). Those ternary interactions, and the direct complexation of U(VI) species onto the cell at lower pH, are ultimately governed by the net electrical potential of that surface.

The bacterial surface is a complex structure with a nuanced coordination environment responsible for complexation reactions (Fein, 2006). Hereafter, we will refer to the outer-

most portion of the cell as its cell envelope to denote the complexity of this cell structure (Rahnamoun et al., 2020). Outer membranes of gram-negative bacteria are composed of an oligosaccharide, and a subset of those also contain an O-specific oligosaccharide anchored by lipid A (Nazarenko et al., 2003; Krasikova et al., 2004). Carboxylic acids, phosphates, and possibly phenols are found within lipid A (Jiang et al., 2004; K. Auer & B. Weibel, 2017). Proteins, embedded throughout the lipopolysaccharides (LPS), are also present in the outer membrane, but likely compose at least an order of magnitude less mass than the total LPS (Beveridge & Murray, 1980; Jiang et al., 2004; Silhavy et al., 2010). A variety of functional groups can be found within proteins, including carboxylic acids, thiols, and amines (Welte et al., 1995; Koebnik et al., 2000; Nell & Fein, 2017). These acidic functional groups found on the cell envelope are responsible for the net electrical potential of a microbial surface. This phenomenon is well documented by previous work measuring ζ potentials in bacterial suspensions. Beskok & Pillai (2008), Ktodzinska et al. (2010), and Ayala-torres et al. (2014) all found that Gram negative cell envelopes are negatively charged above pH 6 – 7.

Electrolytes commonly used in bacterial adsorption studies, such as sodium perchlorate or sodium chloride, can impact ζ potentials and consequently the extent of metal ion interaction with the cell envelope (Alessi et al., 2010). Changing the ionic strength of a bacterial suspension has well known effects on the adsorption of metals onto bacterial surfaces. The impact of ionic strength on the protonation/deprotonation of cell envelope acidic sites is also documented, though the magnitude of that impact is variable (Plette et al., 1995; Daughney & Fein, 1998; Martinez et al., 2002; Fein et al., 2005; Tourney & Ngwenya, 2010; Wray & Gorman-Lewis, 2022). Ngwenya & Chirwa (2015) recently quantified the inverse proportionality between ionic strength and the adsorption of a variety of metals (Sr^{2+}, Co^{2+}, and Cs^{+}) onto multiple sulfate-reducing bacteria. He et al. (2013) observed a similar inverse proportionality between ionic strength and proton adsorption by a hyperthermophilic arachaean. To date, however, few studies have directly investigated the effects of ionic strength on U(VI) adsorption to dissimilatory metal reducing bacteria

(DMRB) (Haas et al., 2001).

This is a crucial weakness in the literature as surface reactions of U(VI) on DMRB have been tied to the reduction of U(VI) (Marshall et al., 2006). Of DMRB, some taxa utilize U(VI) as an energy source, where it acts as the terminal electron acceptor during growth (Lovley, 1993; Anderson et al., 2003). Others enzymatically reduce U(VI) to U(IV), where the energy of that reaction is not used in catabolism (Liu et al., 2002; Burgos et al., 2007). Of these taxa, the species *Shewanella putrefaciens* presents an intriguing dichotomy, where some strains are capable of metabolic U(VI) reduction (Jr & Dichristina, 2000; Dale & Dichristina, 2006), while others can only do the enzymatic version(Brooks et al., 2003; Burgos et al., 2007). Two of the most studied strains are 200 (metabolic reduction) and CN32 (enzymatic).

Critical initial measurements of U(VI) adsorption onto CN32 were made by Haas et al. (2001), where the effects of ionic strength were also taken into account. Missing from that work, however, is a quantification of the effects of divalent cations on U(VI) adsorption as well as the application of site concentrations measured at experimental ionic strengths. In light of Wray & Gorman-Lewis (2022), the CN32 cell envelope may be more sensitive to ionic strength variations than previously thought, especially at higher concentrations than investigated by Haas et al. (2001). For these reasons the interaction between U(VI) and the CN32 cell envelope needs to be rexamined.

Wray & Gorman-Lewis (2022) also suggests that the surface reactivity of CN32 changes with goechemical conditions. It is likely, then, that the chemical reactions occurring on its surface in the presence of U(VI) also vary, especially given the diverse and varied valancies of U(VI) complexation products. Surface complexation models (SCMs), are an excellent tool to investigate U(VI) interactions on bacterial surfaces because they quantify adsorption based on balanced chemical equations and take into account aqueous speciation.

To help address these shortcomings in the literature, we quantified the effects of U(VI) presence on CN32 surface reactivity in concert with four variables: ionic strength, pH, the co-presence of two divalent cations (Ca^{2+} and Mg^{2+}), and the presence of dissolved CO_2.

Additionally, we used SCMs to infer the specific reactions involved in that adsorption, wherein we identified which uranyl species are adsorbing to which functional groups and quantified the stability constants for those reactions. In sum, this work provides new insights into the nature of surface complexation of an important radionuclide onto a common subsurface bacterium.

3.2 Materials and Methods

3.2.1 Cell preparation

CN32 was grown using procedures similar to previous work with that strain (Sokolov et al., 2001; Smith & Ferris, 2003). 5 mL volumes of 30 g/L trypticase soy broth (TSB) were inoculated from cultures of CN32 maintained on a TSB-yeast extract agar. Cultures were grown on an orbital shaker at 120 rpm and 30°C for 24 hours (±4 h). The 5 mL cultures were then used to inoculate larger volumes of TSB, with an inoculation percent of 0.5 %. Cells were harvested during late exponential phase, which was reached after 24 hours (±2 h) of growth.

The biomass was isolated by centrifugation at $5,000\ g$ for 15 minutes. The resulting pellet was washed in a sodium perchlorate solution at either 0.01, 0.1, or 0.5 M by vortexing, centrifuging at $6,552\ g$ for 2 – 4 minutes, and discarding the supernatant. Cells were washed three times, then centrifuged at $6,552\ g$ for two consecutive 30 minute periods. After each 30 min period, any remaining supernatant was removed. Cells were stored at 4°C and used within 24 hours.

3.2.2 Experimental suspensions

Seven experimental solutions of $NaClO_4$ were used, in equilibrium with atmospheric CO_2 ($10^{-3.5}$ bar). In total, one 0.01 M solution and three each of 0.1 M and 0.5 M were prepared. A pair of one 0.1 M solution and one 0.5 M solution was then amended with 10 mM $CaClO_4$. Another pair of the same ionic strengths was amended with 10 mM $Mg(NO_3)_2$. The remaining three solutions (one of each ionic strength) were left unaltered (no Ca^{2+} or Mg^{2+}). U(VI) from an ICP standard was then added to all seven solutions at 10 μM.

All solutions were adjusted to ca. pH 7 to ensure that cellular membrane integrity was maintained initially. The washed cells were suspended in each solution by vortexing, such that the final concentration of biomass was 0.1 g/L (wet weight). All solutions were pre-

pared and kept in teflon bottles to prevent loss of U during preparation.

3.2.3 Adsorption experiments

To prepare adsorption samples, the total volume of suspended cells was divided into two aliquots. One aliquot was titrated to ca. pH 10 and the other was titrated to ca. pH 3, using NaOH and $HClO_4$, respectively. 10 mL samples were taken from each aliquot at intervals of one half pH unit, and were placed in air-tight teflon containers. Those samples were then agitated for 1 hour by placing them on a shaker plate set at 160 rpm. The final pH of each was then measured. The cells were then removed from solution by centrifuging the samples at 10,000 *g* for 10 minutes. 5 mL of the resulting supernatant was then sampled, acidified with 5 μL of 70% HNO_3, and stored at 4°C.

The concentration of U(VI) in the supernatant was measured spectrophotometrically, using arsenazo III as the absorbing ligand. Standards were prepared gravimetrically with the same ICP standard and matrix matched to the samples. Aliquots of both standards and samples were measured gravimetrically and dried on a hot plate and allowed to cool. Each was then brought up in 1.25 mL 3 M HNO_3, followed by 188 μL of 1 M sulfamic acid, 418 μL of 0.6 % arsenazo III (w/w), and 644 μL 3 M HNO_3 (see Dubey et al. (1999)). Samples were measured on a Cary UV-Vis Spectrophotometer, scanning from 700 to 600 nm. From the resultant function, a linear regression of the peak-minus-valley values for the first derivatives of each standard was used to calculate the concentrations of U(VI) in each sample.

3.2.4 Complexation modeling

Surface complexation reactions were fit to the data from low to high pH. We began with a single reaction and added reactions as necessary to improve the fit of the model to the data. Aqueous speciation reactions were used to determine the dominant uranyl species in each pH region. Uranyl species considered in the modeling are summarized in Table 3.1.

Log(K) values for each species were adjusted to the ionic strength of the experiment using the Davies equation. That species was then applied to the surface complexation reaction, where it was assumed that interactions only occurred between a uranyl species and a deprotonated functional group on the cell envelope. For a given pH region, adsorptive sites were selected that were predominantly deprotonated. For pH regions where a poor fit to the data remained, multidentate reactions were included, based on the sites most deprotonated in that region. Surface complexation modeling was performed in Octave (Eaton et al., 2021). System speciation was calculated using a Newton Rhapson algorithm modified from Maeder & Neuhold (2007). Conditional stability constants were optimized using a Levenberg-Marquardt algorithm for non-linear least squares curve-fitting (Gavin, 2019).

Table 3.1: Uranyl species considered in the SCM, along with log(K) values. Obtained from Guillaumont et al. (2003).

U(VI) Species	log(K)
$H_2O + UO_2^{2+} \leftrightarrow H^+ + UO_2OH^+$	-5.25
$2H_2O + UO_2^{2+} \leftrightarrow 2H^+ + UO_2(OH)_2$	-12.15
$3H_2O + UO_2^{2+} \leftrightarrow 3H^+ + UO_2(OH)_3^-$	-20.25
$4H_2O + UO_2^{2+} \leftrightarrow 4H^+ + UO_2(OH)_4^{2-}$	-32.40
$H_2O + 2UO_2^{2+} \leftrightarrow H^+ + (UO_2)_2OH^{3+}$	-2.70
$2H_2O + 2UO_2^{2+} \leftrightarrow 2H^+ + (UO_2)_2(OH)_2^{2+}$	-5.62
$3H_2O + 2UO_2^{2+} \leftrightarrow 3H^+ + (UO_2)_3(OH)_5^+$	-15.55
$7H_2O + 3UO_2^{2+} \leftrightarrow 7H^+ + (UO_2)_3(OH)_7^-$	-32.20
$7H_2O + 3UO_2^{2+} \leftrightarrow 7H^+ + (UO_2)_4(OH)_7^+$	-21.90
$2H_2O + 2UO_2^{2+} \leftrightarrow 2H^+ + (UO_2)_3(OH)_4^{2+}$	-11.90
$CO_3^{2-} + UO_2^{2+} \leftrightarrow UO_2CO_3$	9.94
$2CO_3^{2-} + UO_2^{2+} \leftrightarrow UO_2(CO_3)_2^{2-}$	16.61
$3CO_3^{2-} + UO_2^{2+} \leftrightarrow UO_2(CO_3)_3^{4-}$	21.84
$6CO_3^{2-} + 3UO_2^{2+} \leftrightarrow (UO_2)_3(CO_3)_6^{6-}$	54.00
$CO_{2(g)} + 4H_2O + 2UO_2^{2+} \leftrightarrow 5H^+ + (UO_2)_2CO_3(OH)_3^-$	-19.01
$CO_{2(g)} + 4H_2O + 3UO_2^{2+} \leftrightarrow 5H^+ + (UO_2)_3CO_3(OH)_3^+$	-17.50
$6CO_{2(g)} + 18H_2O + 11UO_2^{2+} \leftrightarrow 5H^+ + (UO_2)_{11}(CO_3)_6(OH)_{12}^{2-}$	-72.50

3.3 Results

3.3.1 Adsorption results

Figure 3.3 illustrates U(VI) adsorption over the pH range and ionic strengths examined. For clarity, the 0.01, 0.1, and 0.5 M experiments will be referred to as low, medium, and high ionic strength systems. From pH 3 – 6, adsorption at all three ionic strengths increased, from 20 – 40% to 60 – 80%. Above pH 6, adsorption in the medium ionic strength system decreased rapidly, with adsorption lowering to ca. 50 % at pH 7 and 40% at pH 9. In the low and high ionic strength systems, adsorption was maintained from pH 6 – 7.5 and then decreased with increasing pH. At pH 9, adsorption was approximately 50% in the low ionic strength system and 20% in the high ionic strength system.

Adsorption of U(VI) with Ca^{2+} co-present, in the medium and high ionic strength systems, is shown in Figures 3.8 and 3.9. The overall trends are similar to U(VI) adsorption without Ca^{2+}, where adsorption increases from approximately 20 – 40% to 60 – 80% from pH 3 to 6. In both the medium and high ionic strength systems, however, adsorption decreases above pH 6, to between 5% and 30% at pH 9. Over a majority of the pH range, adsorption in the high ionic strength system is slightly higher than in the medium ionic strength system. That increase in adsorption is maximized at circumneutral pH where about 30% additional U(VI) is adsorbed.

Figures 3.10 and 3.11 show U(VI) adsorption data with Mg^{2+} co-present. Similar to the other conditions, adsorption increases from pH 3 to 6, from approximately 20 – 40% to 60 – 85%. However, for both medium and high ionic strength systems, adsorption is maintained between pH 6 and 7. Above pH 7, adsorption decreases slightly, with a minimum of about 55% at ca. pH 9 for the medium ionic strength system and 35% in the high ionic strength system. The medium and high ionic strength system data are very similar below pH 6, above which the high system generally yields about about 10% greater adsorption.

3.3.2 SCM results

Table 3.2 summarizes the complexation reactions necessary to describe observed reactivity. Those reactions are also illustrated in Figures 3.5 – 3.7. For all ionic strengths, below pH 5, speciation is dominated by the free uranyl ion and site 1 ($L1$) is the predominant deprotonated surface site. In the low ionic strength system, free uranyl ion complexation with $L1$ underpredicted adsorption below pH 4 and reasonably predicted adsorption between pH 4 and 5, as shown in Figure 3.3. At the higher ionic strengths, adsorption was underpredicted up to pH 5 (medium ionic strength) and pH 5.5 (high ionic strength). To represent adsorption below pH 4, uranyl complexation with protonated $L3$ allowed for the prediction of a relatively constant extent of adsorption as shown in Figure 3.4. In each system, between pH 5.5 and 6.5, $(UO_2)_3(OH)_5^+$ is dominant and $L1$ is still the predominant deprotonated site. In the low and medium systems, complexation between $L1$ and $(UO_2)_3(OH)_5^+$ represented adsorption. In the high system, however, a bidentate complexation reaction involving two $L2$ sites and $(UO_2)_2CO_3(OH)_3^-$ was necessary to represent observed adsorption up to pH 8.5. In the low and medium ionic strength systems, a reaction with surface sites $L2$ and $L3$ complexing $UO_2(CO_3)_3^{-4}$ in a bidentate form best represented adsorption. In the high ionic strength system, however, adsorption was predicted with the complexation of $L1$ with $UO_2(CO_3)_3^{-4}$. Stability constants in Tables 3.2 and 3.3 illustrate that the presence or absence of a uranyl ion complexing onto a protonated $L3$ has no significant impact on the reactions in surface complexation model that control adsorption above pH 4.

Despite similarities in the adsorption data between the low and high ionic strength systems, application of the same surface complexation reactions to both failed to adequately describe adsorption. The addition of $(UO_2)_3(OH)_5^+$ complexation in the high ionic strength system over-predicted adsorption between pH 5 and 6. In the low ionic strength system, a monodentate reaction with $L1$ in place of the bidentate complexation of $UO_2(CO_3)_3^{-4}$ resulted in an under prediction of adsorption above pH 8.

Table 3.2: Log(K) values for each reaction by ionic strength. R denotes the bacterial surface. 1 σ errors are reported.

Reaction	U Surface Complexation Reaction	Low	Medium	High
1	$\mathrm{R-}L1^{-} + \mathrm{UO_2^{2+}} \leftrightarrow R-L1-UO_2^{2+}$	5.63 ±0.17	5.44 ±0.20	4.98 ±0.57
2	$\mathrm{R-}L1^{-} + (\mathrm{UO_2})_3(\mathrm{OH})_5^{+} \leftrightarrow R-L1-(UO_2)_3(\mathrm{OH})_5$	5.70 ±0.37	6.00 ±0.40	
3	$\mathrm{R-}2\cdot L2^{-} + (\mathrm{UO_2})_2\mathrm{CO_3}(\mathrm{OH})_3 \leftrightarrow R-2\cdot L2-(UO_2)_2\mathrm{CO_3}(\mathrm{OH})_3$	12.24 ±0.21	10.12 ±0.29	14.98 ±0.27
4	$\mathrm{R-}L1^{-} + \mathrm{UO_2}(\mathrm{CO_3})_3^{-4} \leftrightarrow R-L1-UO_2(\mathrm{CO_3})_3^{-4}$			6.87 ±0.15
5	$\mathrm{R-}L2^{-} + \mathrm{R-}L3 + \mathrm{UO_2}(\mathrm{CO_3})_3^{-4} \leftrightarrow R-L2-L3-UO_2(\mathrm{CO_3})_3^{-4}$	11.93 ±0.18	11.82 ±0.15	

Table 3.3: Log(K) values for each reaction by ionic strength, with adsorption onto a protonated $L3$ site. R denotes the bacterial surface. 1 σ errors are reported.

Reaction	U Surface Complexation Reaction	Low	Medium	High
0	$\mathrm{R-}HL3 + \mathrm{UO_2^{2+}} \leftrightarrow R-HL3-UO_2^{2+}$	13.73 ±0.31	13.75 ±0.23	14.45 ±0.19
1	$\mathrm{R-}L1^{-} + \mathrm{UO_2^{2+}} \leftrightarrow R-L1-UO_2^{2+}$	5.61 ±0.24	5.40 ±0.16	5.03 ±0.36
2	$\mathrm{R-}L1^{-} + (\mathrm{UO_2})_3(\mathrm{OH})_5^{+} \leftrightarrow R-L1-(UO_2)_3(\mathrm{OH})_5$	5.72 ±0.29	5.93 ±0.26	
3	$\mathrm{R-}2\cdot L2^{-} + (\mathrm{UO_2})_2\mathrm{CO_3}(\mathrm{OH})_3 \leftrightarrow R-2\cdot L2-(UO_2)_2\mathrm{CO_3}(\mathrm{OH})_3$	12.29 ±0.25	10.18 ±0.23	14.95 ±0.17
4	$\mathrm{R-}L1^{-} + \mathrm{UO_2}(\mathrm{CO_3})_3^{-4} \leftrightarrow R-L1-UO_2(\mathrm{CO_3})_3^{-4}$			7.11 ±0.09
5	$\mathrm{R-}L2^{-} + \mathrm{R-}L3 + \mathrm{UO_2}(\mathrm{CO_3})_3^{-4} \leftrightarrow R-L2-L3-UO_2(\mathrm{CO_3})_3^{-4}$	12.00 ±0.22	11.92 ±0.20	

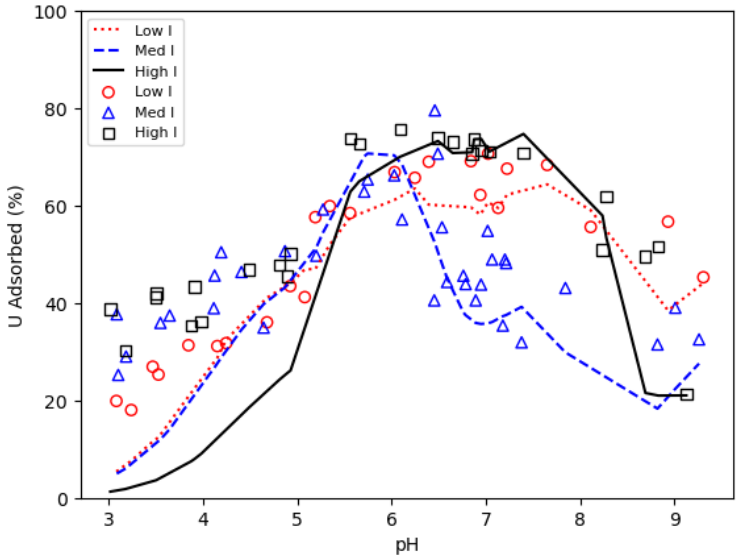

Figure 3.3: Model adsorption predictions with biomass concentrations of 0.1 g/L at each ionic strength.

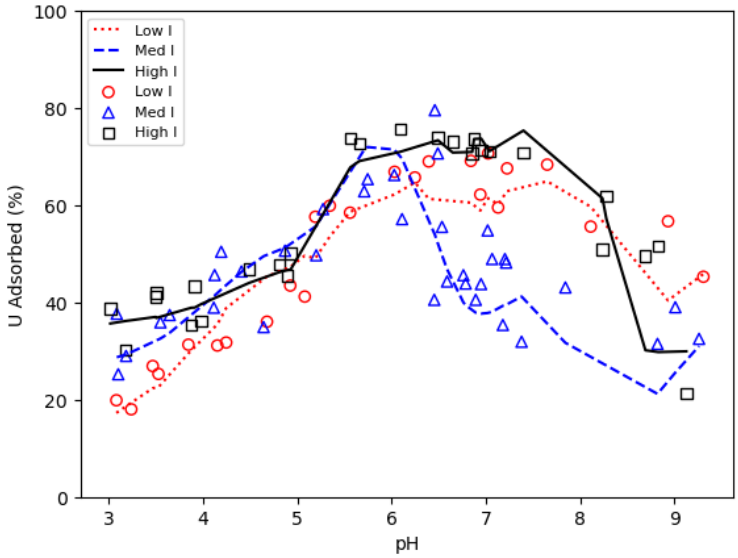

Figure 3.4: Model adsorption predictions, including adsorption onto *HL*3, with biomass concentrations of 0.1 g/L at each ionic strength.

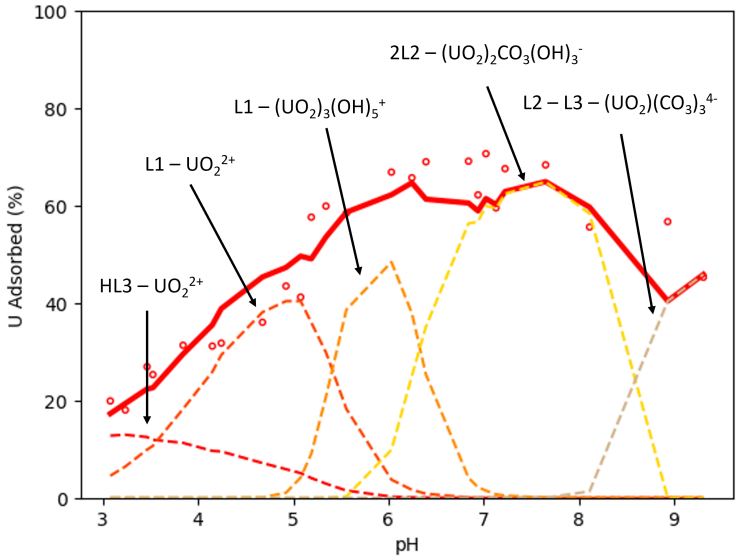

Figure 3.5: Model adsorption predictions with biomass concentrations of 0.1 g/L in the low ionic strength system.

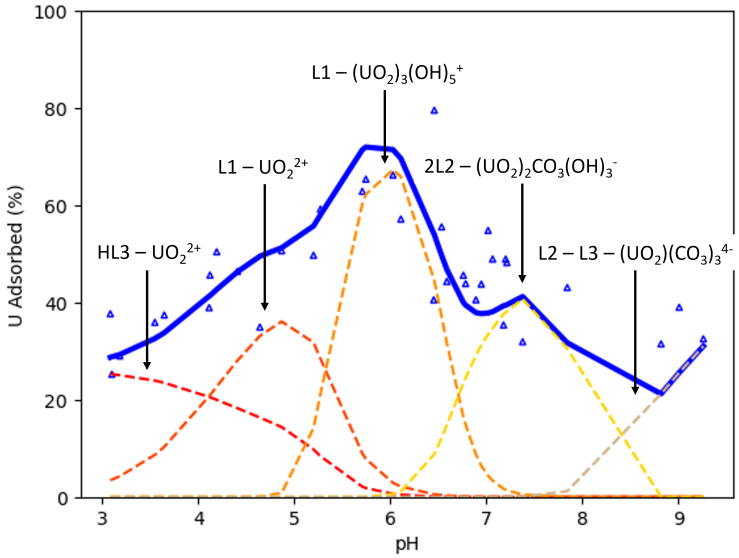

Figure 3.6: Model adsorption predictions with biomass concentrations of 0.1 g/L in the medium ionic strength system.

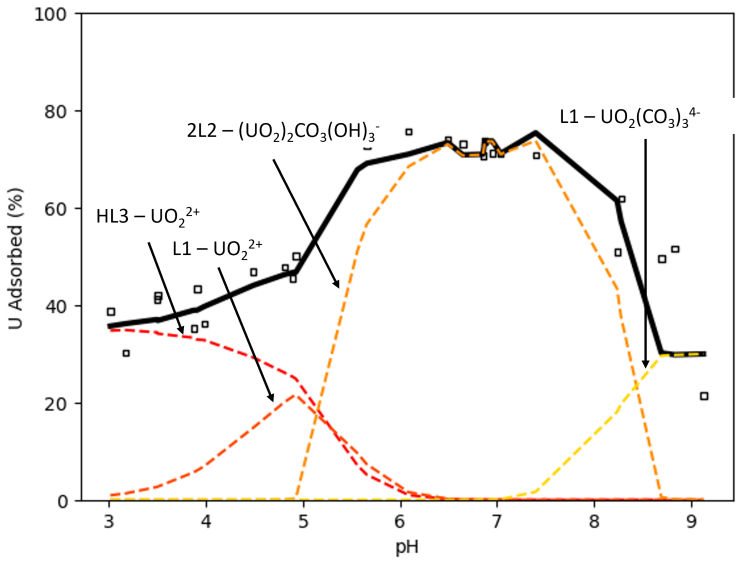

Figure 3.7: Model adsorption predictions with biomass concentrations of 0.1 g/L in the high ionic strength system.

To test the ability of the SCMs to predict uranyl adsorption in the presence of Ca^{2+} and Mg^{2+}, we predicted adsorption using the SCMs in Table 3.3 under the experimental conditions with Ca^{2+} and Mg^{2+} present. Below pH 5, the free uranyl ion is predominant and Reactions 0 and 1 in Table 3.3 are responsible for adsorption in the Ca^{2+}- and Mg^{2+}-free systems. In the Ca^{2+} system, at medium ionic strength, the model substantially over-predicts adsorption from pH 3 – 5 (see Figure 3.8). In contrast, at high ionic strength, adsorption is well predicted over that pH range (Figure 3.9). From pH 5 – 7, $(UO_2)_3(OH)_5^+$ and $(UO_2)_2CO_3(OH)_3^-$ are the dominant uranyl species at both medium and high ionic strength and Reactions 2 and 3 in Table 3.3 are primarily responsible for adsorption in this pH range. At medium ionic strength, the SCM both over-predicts (pH 5 – 6) and under-predicts (pH 6.5 – 7) adsorption, with adsorption well predicted between pH 6 and 6.5. The SCM at high ionic strength slightly under-predicts adsorption over that pH range. From pH 7 – 9, the Ca-complexation product $Ca_2UO_2(CO_3)_3$ is dominant, with additionally high concentrations of $UO_2(CO_3)_3^{4-}$. The SCM only takes surface interactions with $UO_2(CO_3)_3^{4-}$ into account according to Reactions 4 and 5 in Table 3.3. At medium ionic strength, ad-

sorption is not well predicted with both under- and over-prediction occurring between pH 7 and 9. In the high ionic strength system, the SCM slightly over-predicts adsorption from pH 7 to 9 and accurately predicts adsorption above pH 9.

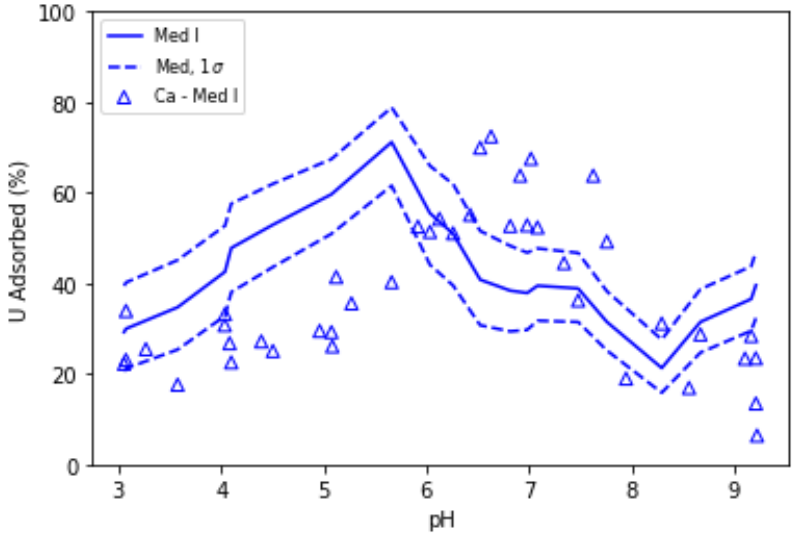

Figure 3.8: U adsorption in the presence of 10 mM Ca, at medium ionic strength, with model adsorption predictions with biomass concentrations of 0.1 g/L (blue curves).

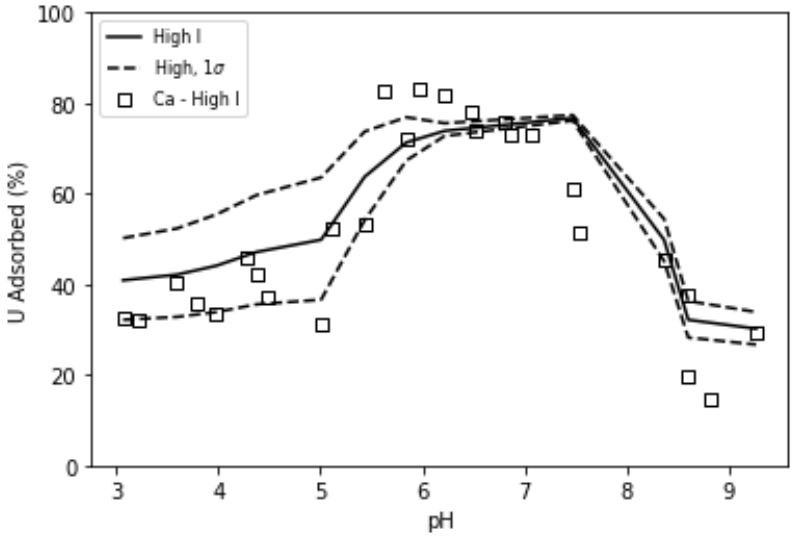

Figure 3.9: U adsorption in the presence of 10 mM Ca, at high ionic strength, with model adsorption predictions with biomass concentrations of 0.1 g/L (black curves).

For the Mg^{2+}-amended system, the SCM predicts adsorption better than for the Ca^{2+}-amended system. Below pH 5, adsorption in both the medium and high ionic strength systems is reasonably predicted (Figures 3.10 and 3.11). From pH 5 – 7, where $(UO_2)_3(OH)_5^+$ and $(UO_2)_2CO_3(OH)_3^-$ are the dominant uranyl species, the SCM at medium ionic strength again both over-predicts (pH 5 – 6) and under-predicts (pH 6.5 – 7) adsorption, with adsorption well predicted between pH 6 and 6.5. At high ionic strength, some under-prediction is observed up to pH 7. Above pH 7 in the medium ionic strength system, $MgUO_2(CO_3)_3^{2-}$ is the dominant species, with high concentrations of $UO_2(CO_3)_3^{4-}$ also present. The $MgUO_2(CO_3)_3^{2-}$ species is not included as a surface complex in the SCM and there is substantial under-prediction of adsorption in the medium ionic strength system. In the high ionic strength system, the uranyl speciation is different than the medium ionic strength system, with $UO_2(CO_3)_3^{4-}$ becoming dominant. Generally adsorption is well predicted above pH 7 in the high ionic strength system.

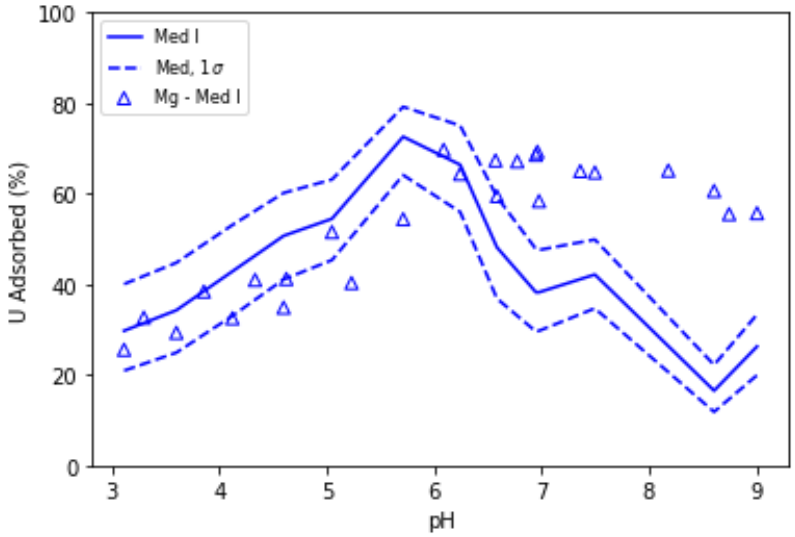

Figure 3.10: U adsorption in the presence of 10 mM Mg, at medium ionic strength, with model adsorption predictions with biomass concentrations of 0.1 g/L (blue curves).

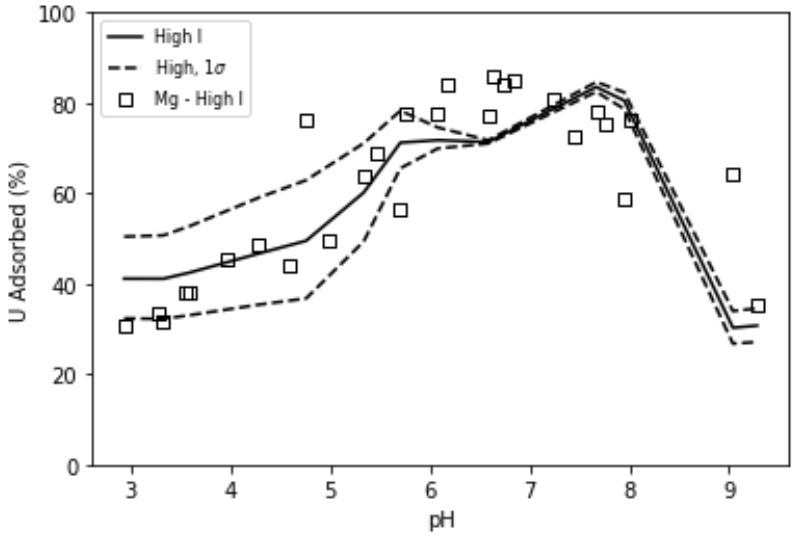

Figure 3.11: U adsorption in the presence of 10 mM Mg, at high ionic strength, with model adsorption predictions with biomass concentrations of 0.1 g/L (black curves).

3.4 Discussion

3.4.1 Low pH Adsorption

The extent of adsorption occurring between pH 3 and 4 is unusual compared to other divalent cations like Cd^{2+} and Pb^{2+}. This is demonstrated with the application of SCMs under similar conditions as our experiments. For the gram-negative bacterium *Pseudomonas putida*, surface complexation modeling between pH 3 and 4 predicts less than 10% adsorption for Pb^{2+} and less than 5% adsorption for Cd^{2+} (Borrok & Fein, 2005). This is far less than the 20 – 40% observed here for uranyl adsorption over that pH range. We can also compare these predictions to an SCM for uranyl adsorption onto *Shewanella oneidensis* MR-1 (Sheng & Fein, 2013a). That model predicts very high adsorption (80 – 90%) between pH 3 and 4, under similar conditions to our experiments. This unusual uranyl adsorption behavior is also evident for the gram-positive bacterium *Bacillus subtilis* (Fowle et al., 2000; Gorman-Lewis et al., 2005a).

It is clear the reactivity of the uranyl ion at low pH with microbial surfaces is unique compared to other divalent cations. Describing this unique behaviour with SCMs is possible despite a lacking a complete understanding of the complexation mechanism. For example, Sheng & Fein (2013a) used a protonation model for *S. oneidensis* MR-1 that possessed a surface site with a relatively low log(K) (3.3). Consequently, the deprotonated site concentrations of this low acidity constant site were sufficient to represent the unusual adsorption behavior observed. This contrasts with the protonation behavior of CN32. Several studies that have measured CN32 surface reactivity and have not identified a site with a low log(K) value comparable to *S. oneidensis* MR-1 (Haas et al., 2001; Sokolov et al., 2001; Smith & Ferris, 2003; Wray & Gorman-Lewis, 2022). Still, measurements in this work and by Haas et al. (2001) show elevated adsorption below pH 4. This suggests that there is a site with a low log(K) value, that cannot be resolved through potentiometric titrations, and is thus likely present at very low concentration. To explain the magnitude of adsorption observed in concert with such a low concentration, that site likely has a high affinity for

uranyl ions. In the absence of a thermodynamic description of that site, we can represent its contribution to observed adsorption with reactions onto the predominant protonated site at that pH range, $HL3$.

3.4.2 Carbonate Complexation and Ionic Strength Impacts

The uranyl ion forms extremely stable, soluble neutral and negatively charged complexes with carbonate above pH 6 (Panias & Krestou, 2015). This carbonate complexation influences uranyl mobility under oxidizing circumneutral pH conditions by potentially limiting interactions with charged surfaces. For mineral surfaces, we can describe potential interactions with the zero point charge (ZPC), where a mineral is positively charged below its ZPC and negatively charged above it. The negatively charged uranyl carbonate complexes, therefore, can be predicted to interact strongly with the surface below a given ZPC, but electrostatics predicts that there should not be interaction above it. This is supported by the literature, where measurements of adsorbed U(VI) drop off dramatically at high pH (Coutelot et al., 2018; Tournassat et al., 2018; Mei et al., 2020). Microbial surface interactions with uranyl carbonates are theoretically more limited as microbial surfaces are uniformly negatively charged over physiological pH ranges (Wilson et al., 2001). However, uranyl complexation on bacterial surfaces, at pH values where negatively charged uranyl carbonates are dominant, has been repeatedly observed (Fowle et al., 2000; Haas et al., 2001; Sar & D'Souza, 2001; Gorman-Lewis et al., 2005a; Sheng & Fein, 2013b)

In this work, as expected, the presence of CO2 decreased adsorption above ca. pH 6. Still, the relatively high amounts of adsorption observed above pH 6 are surprising given the negative charge on the cell surface and the anionic uranyl complexes that form under atmospheric conditions at high pH (see Figure 3.1). Ternary reactions where a Na^+ ion bridges the negatively charged surface and complex may explain these results. Previous work has observed such reactions to explain high radionuclide adsorption at high pH (Wainipee et al., 2013; Kenney et al., 2017b). Our results are notably exaggerated in

this manner, with adsorption above 40% observed at ca. pH 9 (previous data on other *Shewanella* strains have a maximum adsorption closer to 10% at that pH range, see Haas et al. (2001)).

Overall, it appears that ionic strength has a significant, but varied effect on CN32 surface reactivity in concert with U presence. Above pH 6, the adsorption in the low and high ionic strength systems were more similar to each other than that in the medium ionic strength system. This may be the result of two forces: an expansion of the electric double layer at low ionic strength (Brown & Zhao, 1995), and increased Na^+ bridging at high ionic strength (Barnie et al., 2018).

The electric double layer, which defines reactive potential and thus ability to adsorb uranyl species, for any compound scales inversely with ionic strength (Langmuir, 1997). As the concentration of ions in solution increases, the double layer is repressed, and cannot extend as far into solution. An increase in the adsorptive potential on CN32 at low ionic strength is consistent with an extended double layer. The fact that this was not observed across the entire pH range suggests that the affinity of sites reacting at lower pH is greater than those at higher pH.

At high ionic strength, we would expect adsorption to decrease, as the double layer is limited. However, as ionic strength increases the concentration of positively charge ions in solution also increases. This has the potential to facilitate increased cationic bridging between the surface and uranyl species. An increase in adsorption, then, would be expected if the dominant uranyl species is negatively charged, as cationic bridging should not play a large role in adsorption if the surface and uranyl species are oppositely charged. This is true at high pH, where the aforementioned uranyl carbonates are dominant. Our data are consistent with this, where the high ionic strength system correlates with increased adsorption above ca. pH 6. Moreover, as shown in Figure 3.7, the primary reactions that accurately predict observed adsorption involve $(UO_2)_2CO_3(OH)_3^-$ and $UO_2(CO_3)_3^{4-}$. This effect, however, must also be taken in concert with the cation amendment experiments,

where adsorption was decreased by the addition of Ca^{2+}.

3.4.3 Divalent Cation Effects

The observed impacts of Ca^{2+} and Mg^{2+} may reflect differential effects of LPS packing. It has recently become well established that divalent cations can impart significant changes to cell surface reactivity (Silhavy et al., 2010; Simpson & Trent, 2019; Rahnamoun et al., 2020). The comparative effects of two ions on the same cell surface has not been examined in detail. These data suggest that that impact may not be uniform, where divalent cations of larger atomic radii may have substantially different effects than smaller ions.

The relative adhesion of Ca^{2+} versus Mg^{2+} to the cell wall may also explain the contrast between U adsorption in systems amended with those ions. The uptake of metals onto the cell wall is known to vary, and, critically, microbial surfaces have a higher affinity for Mg^{2+} than Ca^{2+} (Beveridge & Murray, 1976; Beveridge & Koval, 1981). Consequently, Mg^{2+} should have a greater impact on surface reactivity than Ca^{2+}. For U adsorption, then, Mg^{2+} may be better able to serve as an ionic bridge between the bacterial surface and negatively charge uranyl carbonate complexes. So, a greater number of bridges are formed with Mg^{2+} present than with Ca^{2+}. Our data in the medium ionic strength system are consistent with this, where Mg^{2+} presence yielded a substantial increase in U adsorption relative to predictions, while Ca^{2+} did not. Also in the medium ionic strength system, Ca^{2+} presence correlated to a decrease in U adsorption at low pH, while Mg^{2+} did not. This contrast may be due to differential impacts of Ca^{2+} and Mg^{2+} on determining the stability of the outer membrane. It has recently been demonstrated that Ca^{2+} presence yields more a symmetric LPS structure by binding to the core of the rough mutant LPS (Clifton et al., 2015). Moreover, there is some evidence that the symmetry of the LPS affects surficial interactions between the microbe and its environment (Lundstedt et al., 2021). This suggests that the presence of Ca^{2+} may, to some degree, alter the adsorptive potential of CN32 by increasing the symmetry of the outer membrane. As pH increases, the cationic

bridging between Ca^{2+} and uranyl-carbonates (which is present, just less so than for Mg^{2+}) may explain why that decrease in adsorption is lost.

In the high ionic strength system, both impacts from Ca^{2+} and Mg^{2+} presence discussed above are lost. This is most readily explained by the reduction in ionic activity with increased ionic strength. In addition, the much higher concentration of Na^{+} ions (500 mM versus 10 mM for Ca^{2+} and Mg^{2+}) may mean that adsorption is primarily governed by Na^{+}-based bridging at high ionic strength. Our data seem to be consistent with this, as adsorption in all three high ionic strength systems (no added cations, and Ca^{2+}/Mg^{2+}-amended) exhibit similar adsorption across the pH range examined.

3.5 Conclusions

The application of SCMs to describe CN32 surface complexation with U(VI) as a function of four environmentally relevant variables (pH, ionic strength, CO2, and co-present cations) provides new insights into the reactivity of that bacterium. Taken in concert with site-specific stability constants and concentrations identified by Wray & Gorman-Lewis (2022), this further allowed for the elucidation of potential complexation reactions to explain observed U(VI) adsorption. Those data indicate a marked increase in adsorptivity at low and high ionic strength, likely explained by a repressed double layer and increased cationic bridging. Na^{+}-based bridging between the negatively charged surface and negatively charged uranyl carbonate complexes above pH 6 also explains the maintenance of relatively large amounts of adsorption at high pH. Lastly, the countervailing effects of two divalent cations, Mg^{2+} and Ca^{2+}, is explained by the differential interactions those ions have with the cell surface. In sum, this work advances our understanding of surficial interactions between a common groundwater bacterium and a widespread radionuclide, with relevance to environmental habitability.

Chapter 4

BIOENERGETICS OF AEROBIC AND ANAEROBIC GROWTH OF *SHEWANELLA PUTREFACIENS* CN32

Co-authored by Addien C. Wray and Drew Gorman-Lewis

Abstract

The utilization of chemical energy in catabolism and the conversion of that energy into new biomass via anabolism underpins observed life. Identifying the presence of habitable conditions, and defining the magnitude of that habitability, is thus predicated on a thorough understanding of energetic needs of microbial life. In this work, we examined the bioenergetics of O_2 and Fe(III) reduction coupled to lactate oxidation in *Shewanella putrefaciens* CN32. Bioenergetics were measured directly via isothermal calorimetry and by changes to the chemically defined growth medium. We performed these measurements from 25 to 36°C. Describing metabolism with macrochemical equations allowed us to determined the thermodynamic growth efficiency of CN32. Aerobic growth efficiency (energy normalized to C-mole of biomass produced) was maximized at 30°C, minimized at 25°C, and progressively decreased above 30°C. Fe(III)-based growth efficiency was insensitive to temperature at 30°C and below. These results suggest that temperature effects on CN32 are metabolism-dependent, where more energy was needed for non-growth reactions under aerobic conditions at decreased temperatures than for anaerobic growth. This is intriguing given the substantially greater potential energy by using O_2 as an electron acceptor rather than Fe(III). Standard state predictions of growth grossly overestimated Gibbs energy requirements and better predicted the partitioning of Gibbs energy as growth enthalpy. By quantifying the growth requirements of CN32, we have advanced our understanding of the thermodynamic constraints of a metabolically multifaceted microorganism. Ultimately,

this work demonstrates that the rigorous evaluation of habitability requires a suite of measurements rather than theoretical calculations based on specific electron donors and acceptors alone.

4.1 Introduction

Microbial metabolisms play a key role in establishing the geochemistry of groundwater systems (Flynn et al., 2013; Maamar et al., 2015; Mansuy, 2018). To best predict potential interactions between microbes and their geochemical environment in a given system, it is necessary to consider the bioenergetics involved (Heijnen & Kleerebezem, 2010; Smeaton & Van Cappellen, 2018; Cook et al., 2021; Hart & Gorman-Lewis, 2021; Paquete et al., 2021). Microbial bioenergetics is primarily based on the redox reactions performed during the catabolic cycle (Heijnen & Kleerebezem, 2010). This allows us to describe geochemical systems in terms of potential available chemical energy, based on available electron donors and acceptors (Hoehler, 2004; Ray et al., 2021). For example, in a system with available organic carbon, potential free energy for heterotrophic growth is maximized when oxidation of that organic carbon is coupled to O_2 reduction. In the absence of sufficient O_2, other potential electron acceptors, such as Fe(III), become metabolically relevant. Similarly, in anoxic and dysoxic systems, a variety of redox couples are important, where maximum available energy depends on available redox couples. Taken together, in addition to free energy sources like O_2, other metabolically-available gases (e.g., CO_2) and both colloidal and dissolved minerals are metabolically relevant when considering the entire subsurface environment. As a result, highly diverse microbial communities and taxa that are able to metabolize a variety of available energy sources play a large role in establishing subsurface redox conditions (Borch et al., 2010; Sang et al., 2018).

The facultative anaerobic bacterium *Shewanella putrefaciens* is widely considered a model dissimilatory metal-reducing bacterium (DMRB), as it can obtain energy for growth on a variety of metals (Lovley, 1993; Liu et al., 2002; Brooks et al., 2003; Yang et al., 2014). *S. putrefaciens* is unique among most DMRB's because it is also able to grow aerobically, making it relevant to both oxic and anaerobic systems (Nealson & Moser, 1996). To date, however, little research has compared its aerobic and anaerobic growth strategies. This is an important gap in the literature, as the metabolic plasticity exhibited by *S. putrefaciens* is

relevant to the impact it may have on metals in the subsurface. Specifically, it allows the organism to maintain its growth even if metal concentrations fluctuate, potentially resulting in varied redox conditions, which would affect other microbial metabolisms and thus the geochemical state of the system as a whole.

The growth of a variety of *S. putrefaciens* strains and metabolisms have been partially investigated stoichiometrically. However, little work has sought to verify theoretical catabolic stoichiometry with more detailed measurements of changes to growth media. For example, Kostka et al. (1995) first identified strain MR-1 as a catalyst for Mn(III) reduction, but only measured the relative changes in electron donors and acceptors. Similar analysis was done by Philips et al. (2018) for Fe(0) oxidation by strain 4t3-1-2LB. The stoichiometry of Fe(II) mineral products from Fe(III) reduction-based enzymatic activity by strain CN32 has also been invstigated (Kukkadapu et al., 2005). Growth-based Fe(III) reduction in strains W3-18-1 and CN32 were also investigated by Cossio Salas et al. (2009) and O'Loughlin et al. (2019) respectively, where stoichiometric ratios of electron donors, Fe(II), and in the case of Cossio Salas et al. (2009), carbon sources, were measured. In order to use measurements of redox species to constraint the catabolic reaction, each potential chemical species involved in that reaction, such as H^+ and the oxidized form of the electron donor, need to be measured. This more exhaustive approach has not been taken with *S. putrefaciens*. Moreover, to the authors' best knowledge, measurements pertaining to the stoichiometry of aerobic growth by *S. putrefaciens* have not been made. To fully understand the impact a microbe may have on its environment, observations of growth stoichiometries are necessary. The lack of these data and reliance on theoretical catabolic reactions is a crucial gap in the literature and must be addressed to accurately assess the impact *S. putrefaciens* may have on *in situ* geochemical conditions throughout the subsurface.

Accurate descriptions of growth stoichiometry are also necessary to constrain the bioenergetics of growth. We can represent growth with simplified chemical equations to represent catabolism and anabolism. Those equations can be used to calculate the thermodyna-

mic potential during growth (ΔG) in a system of interest. By measuring changes to growth media, we can make this calculation before and after growth to quantify the Gibbs energy consumed. This Gibbs energy consumption characterizes geochemical impacts on the environment and provides the mean to assess the potential of growth based on geochemical conditions.

$$\Delta G = \Delta H - T\Delta S \tag{4.1}$$

Calorimetric measurements of growth are needed in addition to calculations of Gibbs energy consumption for a complete thermodynamic description of the metabolic process. Equation 5.2 describes the relative driving forces behind Gibbs energy consumption (i.e., enthalpy (ΔH) versus entropy (ΔS)), where T is absolute temperature. Specifically, this approach allows us to determine if the Gibbs energy is dissipated primarily as enthalpy or as entropy. This combined analysis of ΔG and ΔH has only rarely been applied (von Stockar et al., 1993; Schill et al., 1999; von Stockar et al., 2006; Hart & Gorman-Lewis, 2021), but yields a more nuanced description of the overall energetics involved in growth. It has not been applied to any *S. putrefaciens* strain and is an important gap in our understanding of the growth of that microbe.

Clearly, a complete understanding of *S. putrefaciens* biology and its impacts on subsurface geochemistry needs to include a stoichiometric and thermodynamic description of both its aerobic and anaerobic growth. In this study, we examined the bioenergetics of lactate oxidation coupled to O_2 and Fe(III) reduction. The bioenergetics were measured directly via isothermal calorimetry and through measured changes in a chemically defined growth medium. In addition, by repeating these measurements over a range of temperatures (25-36°C), we were able to infer how *S. putrefaciens* allocates its energy under a range of environmental conditions. In all, by quantifying both aerobic and anaerobic growth requirements of *S. putrefaciens*, this study advances our understanding of an important regulator of groundwater geochemistry.

4.2 Materials and Methods

4.2.1 Culture preparation

S. putrefaciens strain CN32 was maintained aerobically and anaerobically on a defined growth medium (Myers & Nealson, 1988; Belli et al., 2015) at 30°C. Aerobic cultures were grown with approximately 10 mM sodium lactate on an orbital shaker. Anaerobic cultures were grown with approximately 15 mM sodium lactate and 30 mM ferric citrate, in borosilicate glass tubes sealed with butyl rubber septum type stoppers and aluminun sealing rings. The anaerobic chamber was maintained with an N_2:H_2 atmosphere (98:2). Cultures were maintained with an initial cell density of 8×10^5 ($\pm$ 2×10^5) cells per mL, and were grown to late exponential phase. Slides for cell counts were prepared using Whatman 0.2-µm filter membrane with SYBR Green I dye following the procedure of Lunau et al. (2005) and with appropriate filters on a Zeiss Axiostar Plus Microscope.

4.2.2 Calorimetric analysis

Calorimetric measurements were made by growing 3 mL cultures of CN32 in 4.22 mL glass vials, sealed with butyl rubber septa and aluminum sealing rings, in a TAM III nanocalorimeter that measures heat flux between a reaction and reference vessel as a function of time (Johansson & Wadsö, 1999; Goldberg & Wadsö, 2001). Calorimetric response was calibrated by electrical heating and verified by measuring protonation of TRIS at 25°C (Grenthe et al., 1970). Experiments were performed from 25 – 36°C. The range of temperatures included was based on reproducibility of biomass and heat yield.

Cultures were prepared on the same growth medium with an initial cell density of 5×10^5 ($\pm$ 1×10^5) cells per mL and with limited electron acceptor (O_2, Fe(III)) availability. Aerobic cultures were were sealed under atmospheric conditions, yielding an initial headspace with approximately 10 μmol O_2. For the anaerobic cultures, initial concentrations of sodium lactate and ferric citrate were 15 mM and 7 mM, respectively, and vials

were sealed in the anaerobic chamber.

The total heat evolved during growth was measured by monitoring heat flux in the calorimeter throughout the growth period, and the integrating under the resulting curve. Calculation of microbial growth rate and duration of the exponential phase was performed in R with the package grofit (Kahm et al., 2010) based on total heat evolution.

4.2.3 Overall growth reaction modeling

The systems investigated in this work related to growth of CN32 under controlled conditions in reaction vials. From this point forward, we refer to changes in the reaction vials as a result of microbial growth as "incubation" to recognize that abiotic or biotically influenced abiotic reactions will also occur. Simplified macrochemical equations to represent cell growth were used according to Heijnen & Kleerebezem (2010). Those equations are based on the production of one carbon-mole of generic biomass, according to the formula $CH_{1.8}O_{0.5}N_{0.2}$ (Heijnen & Kleerebezem, 2010; Calabrese et al., 2021). The anabolic and catabolic components of the growth reaction were represented according to Equations 5.3 and 5.4. The coefficients for the anabolic and catabolic reactions were determined by solving a series of linear equations to satisfy balances of mass and charge.

$$Y^{an} = a \cdot e^{-}donor + b \cdot Nsource + c \cdot H^{+} + d \cdot H_2O + e \cdot CO_2 + f \cdot oxidizede^{-}donor + CH_{1.8}O_{0.5}N_{0.2} \quad (4.2)$$

$$Y^{cat} = g \cdot e^{-}donor + h \cdot e^{-}acceptor + i \cdot oxidizede^{-}donor + j \cdot reducede^{-}acceptor \quad (4.3)$$

To produce sufficient energy to drive anabolism, the catabolic reaction needs to be performed multiple times. That relationship defines the catabolic multiplicative factor necessary to produce one C-mol of biomass, f_{cat}, as described in Equation 5.5

$$f_{cat} = \frac{-1}{Y_{X/D}} + Y_D^{an} \tag{4.4}$$

where $Y_{X/D}$ is the C-mol biomass produced per mol of e^-donor consumed and Y_D^{an} is the anabolic coefficient of the e^-donor.

From Equations 5.3 – 5.5 we can calculate the coefficients for the overall growth reaction (OGR) with Equation 5.6:

$$Y^{OGR} = Y^{an} + f_{cat} \cdot Y^{cat} \tag{4.5}$$

4.2.4 Gibbs energy of incubation

The Gibbs energy change during incubation was calculated for each experiment before and after growth based on activities of all the chemical species in the overall growth reaction. Measurements of pH and O_2 were made with an Orion 8103BN Ross semi-micro combination pH electrode and a Unisense OX-NP-006340 Clark-type oxygen microelectrode, respectively. Fe(III) was measured with the ferrozine method (Viollier et al., 2000) under anaerobic conditions. Standard states for this work at all temperatures and pressures are unit activity of the pure solvent, unit activity of aqueous species in a hypothetical 1 molal solution referenced to infinite dilution, unit activity of the pure minerals or other crystalline solids, and unit fugacity of a pure gas at 1 bar. The standard state Gibbs energies of formation (ΔG_f°) for the chemical species in the growth reaction were calculated at the experiment temperature with the revised Helgeson-Kirkham-Flowers (HKF) equations of state (Helgeson et al., 1978, 1981; Tanger & Helgeson, 1988) using SUPCRT92 (Shock et al., 1989; Johnson et al., 1992). For biomass, $\Delta G_f^\circ = -67$ kJ/mol was used for all growth experiments (Heijnen & van Dijken, 1992). The standard state Gibbs energies of reactions (ΔG_r°) of the overall growth reaction determined for each experiment were calculated using Equation 5.7, where $\Delta G_{f,products}^\circ$ and $G_{f,reactants}^\circ$ are the standard state Gibbs energies of formation for the products and reactants of the growth reaction, respectively, and Y_i^{ogr} is

the stoichiometric coefficient of the ith chemical species in the overall growth reaction.

$$\Delta G_r^\circ = \sum(\Delta G_{f,products}^\circ \times Y_i^{ogr}) - \sum(\Delta G_{f,reactants}^\circ \times Y_i^{ogr}) \tag{4.6}$$

The change in Gibbs energy of a given chemical reaction represents the Gibbs energy potentially available for microbial growth. This is defined by Equation 5.8, where ΔG_r° is modified with the concentration-dependent reaction quotient (Q), the universal gas constant (R), and absolute temperature (T).

$$\Delta G = \Delta G_r^\circ + 2.3026 \times R \times T \times log(Q) \tag{4.7}$$

Q was calculated according to Equation 5.9, where a_i is the thermodynamic activity of the i^{th} chemical species in the overall growth reaction (r) and $v_{i,r}$ is the stoichiometric coefficient for that species.

$$Q = \Pi a_i^{v_{i,r}} \tag{4.8}$$

Activities of the aqueous species were calculated using PHREEQC (Parkhurst & Appelo, 1999). Activity of biomass in solution was converted from molality (C-mol/kg solvent) assuming an activity coefficient of 1 (Tebes-Stevens et al., 1998; Xu et al., 1998; Parkhurst & Appelo, 1999). Overall Gibbs energy change during incubation, ΔG_{inc}, for each experiment was calculated with Equation 5.10 as the difference between initial ΔG_r available ($\Delta G_{r,initial}$), calculated from the initial chemical composition of the medium solution and biomass, and final ΔG_r available ($\Delta G_{r,final}$), calculated from the final chemical composition of the medium solution and biomass.

$$\Delta G_{inc} = \Delta G_{r,initial} - \Delta G_{r,final} \tag{4.9}$$

4.3 Results

4.3.1 Enthalpies of growth

For each condition, the total heat evolved was normalized to C-mol biomass produced (Figure 4.1). For aerobic growth, ΔH_{inc} was significantly affected by temperature, at 95% confidence. Specifically, it was least exothermic at 30°C and was more exothermic at 25°C and 36°C. ΔH_{inc} at 35°C was not statistically distinguishable from ΔH_{inc} 30°C or 36°C. Anaerobic growth was also significantly affected by temperature, but with a countervailing trend. At 25, 27, and 30°C ΔH_{inc} values for anaerobic growth were not statistically different, at 95% confidence. ΔH_{inc} then increased above 30°C, with statistically significant increases at 33 and 35°C, also at 95% confidence.

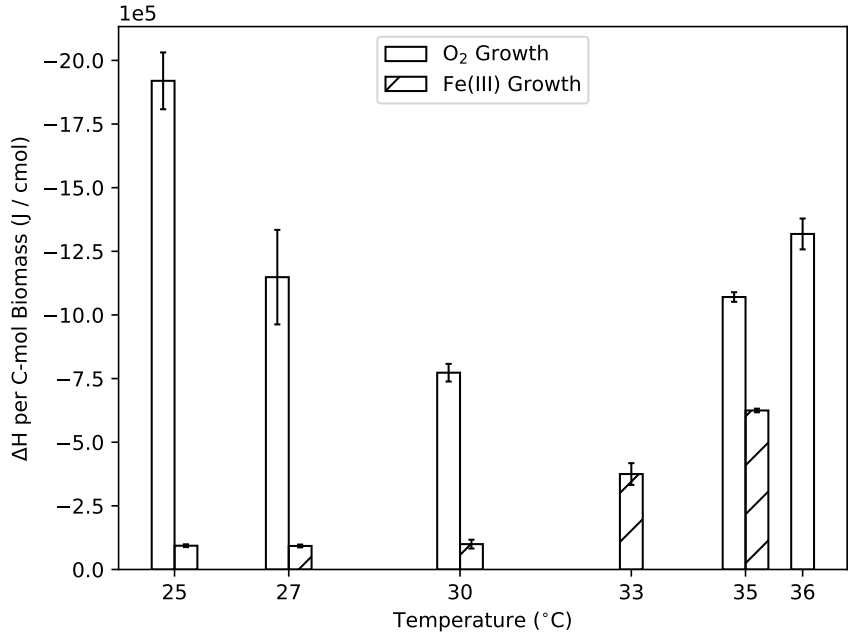

Figure 4.1: Enthalpies of O_2- and Fe(III)-based growth, normalized to C-mol biomass. Error bars reflect standard deviation between replicate experiments.

4.3.2 *Gibbs energy consumption*

The total amount of Gibbs energy consumed during incubation was also normalized to C-mol biomass produced. Figure 4.2 illustrates similar trends to ΔH_{inc}, with a significant impact of temperature for both aerobic and anaerobic growth at 95% confidence. ΔG_{inc} for the aerobic data was least exergonic at 30°C and most exergonic at 25°C. In contrast to the enthalpy data, ΔG_{inc} above 25°C were not distinguishable. Anaerobic ΔG_{inc}, however, demonstrated an identical trend and statistical significance with ΔH_{inc}.

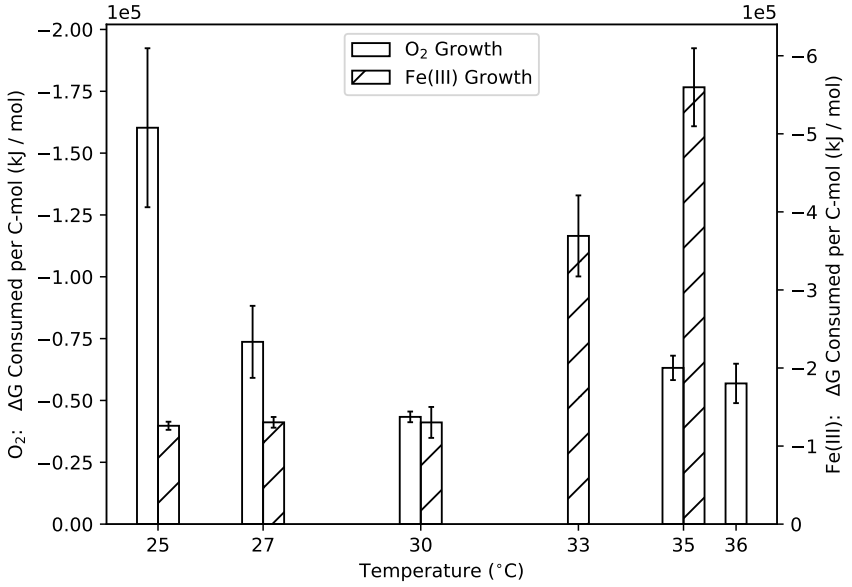

Figure 4.2: Overall Gibbs energy consumed for O_2- and Fe(III)-based growth, normalized to C-mol biomass. Error bars reflect standard deviation between replicate experiments.

4.3.3 *Growth Efficiency*

The fraction of ΔG_{inc} used by the anabolic reaction is illustrated in Figure 4.3 relative to the catabolic ΔG_{inc} liberated. O_2-based growth used between 9 and 54% of the catabolic ΔG_{inc} for anabolic reactions. That percent varied with temperature, where the anabolic reaction consumed the most ΔG_{inc} at 30°C and the least at 25°C. In the anaerobic system,

the anabolic reaction comprised less than 11% of catabolic ΔG_{inc} across the temperature range examined. These trends can also be clearly viewed by considering the thermodynamic efficiency of growth, defined as the ratio of the anabolic to catabolic ΔG_{inc} scaled by f_{cat} (Figure 4.4) (Calabrese et al., 2021). O_2-based growth reaches peak thermodynamic efficiency at 30°C. An increase in thermodynamic efficiency with a decrease in temperature is clear in the anaerobic system with growth at 30°C and below more efficient than 33 and 35°C.

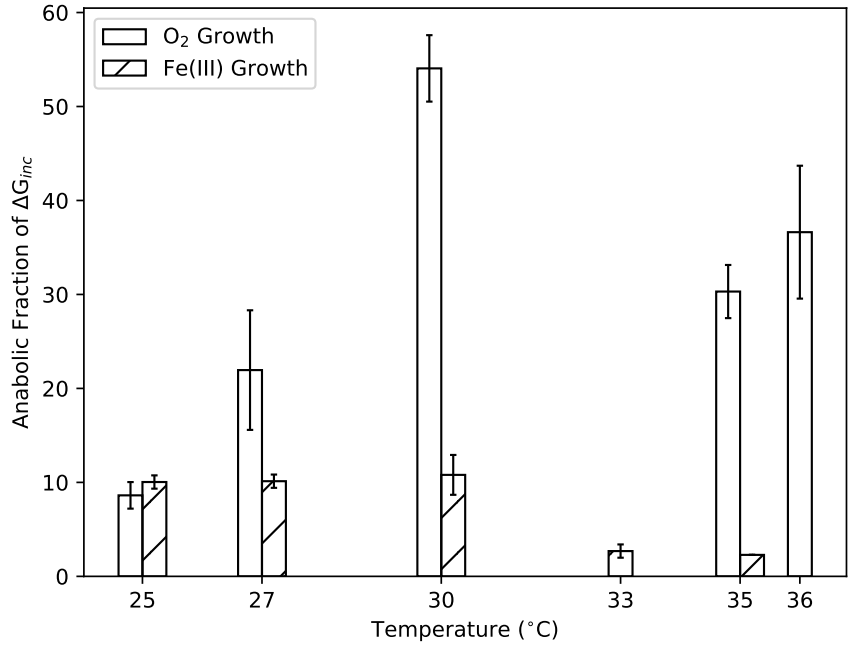

Figure 4.3: Anabolic component of the Gibbs energy consumed for O_2- and Fe(III)-based growth. Error bars reflect standard deviation between replicate experiments.

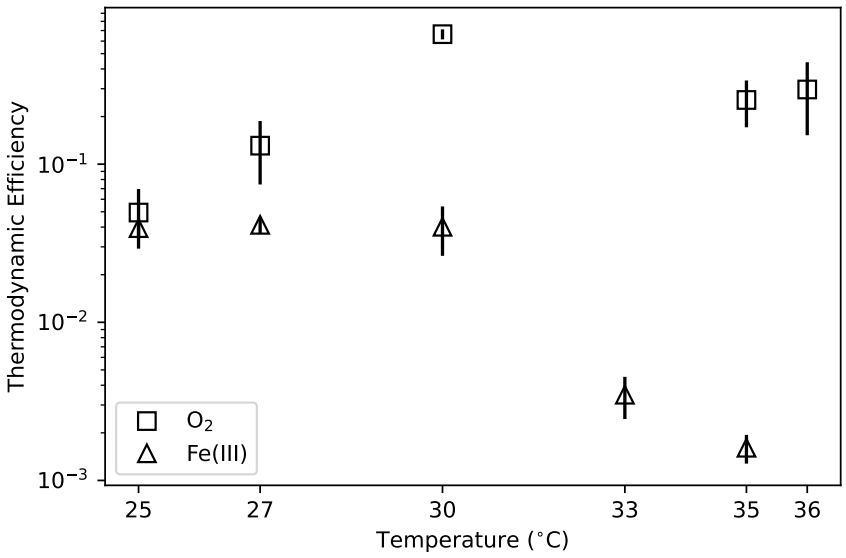

Figure 4.4: Thermodynamic efficiency of growth as a function of temperature and electron donor. Error bars reflect standard deviation between replicate experiments.

4.3.4 Growth stoichiometry

We determined catabolic reactions for each growth strategy based on Equation 5.4 and constraints provided by changes to the growth media. As shown in Equations 4.10 and 4.11, the stoichiometric ratios of electron donor and acceptor differed between O_2 and Fe(III) growth. For aerobic growth, one mole of O_2 is reduced per mole of lactate oxidized. In Fe(III) growth, 1.33 moles of Fe(III) are reduced per mole lactate. For both growth systems, lactate was partially oxidized and acetate/acetic acid was produced along with CO_2. The anabolic reaction, solved according to Equation 5.3, is the same for aerobic and anaerobic growth since the electron acceptor is not involved in the reaction, as shown in Equation 4.12. The reaction involved the conversion of lactate, ammonium, and protons into biomass. The overall growth reactions, as determined with Equations 5.5 and 5.6, for aerobic and anaerobic growth are shown in Equations 4.13 and 4.14, respectively. Those reactions predict 0.74 moles of O_2 to be reduced per mole lactate in the aerobic system,

and 0.99 moles of Fe(III) per mole of lactate in the anaerobic system. The observed ratio of O_2:lactate in the experiments was 0.33 $\pm$0.01. The ratio of Fe(III):lactate in the experiments was 0.40 $\pm$0.03. These are both much closer to the stoichiometry for the overall growth reaction than the catabolic reaction alone.

$$C_3H_5O_3^- + O_2 = C_2H_3O_2^- + CO_2 + H_2O \tag{4.10}$$

$$C_3H_5O_3^- + 1.33Fe^{3+} + 0.33OH^- = 1.33C_2H_4O_2 + 1.33Fe^{2+} + 0.33CO_2 \tag{4.11}$$

$$0.35C_3H_5O_3^- + 0.2NH_4^+ + 0.15H^+ = CH_{1.8}O_{0.5}N_{0.2} + 0.45H_2O + 0.05CO_2 \tag{4.12}$$

$$1.35C_3H_5O_3^- + O_2 + 0.2NH_4^+ + 0.15H^+ = CH_{1.8}O_{0.5}N_{0.2} + C_2H_3O_2^- + 1.05CO_2 + 1.450H_2O \tag{4.13}$$

$$1.35C_3H_5O_3^- + 1.33Fe^{3+} + 0.33OH^- + 0.2NH_4^+ + 0.15H^+ = CH_{1.8}O_{0.5}N_{0.2} + 1.33C_2H_4O_2 + 1.33Fe^{2+} + 0.38CO_2 + 0.450H_2O \tag{4.14}$$

4.3.5 Growth rate impacts

For both O_2 and Fe(III) growth, the growth rate increased with temperature. As shown in Figure 4.5, growth rate was maximized at the highest temperature included for each condition (35°C for Fe(III) and 36°C for O_2). For aerobic growth, at 95% confidence, growth rates below 36°C were indistinguishable. For anaerobic growth, however, growth rates at each temperature were statistically unique. However, the magnitude of variation between

25°C and 30°C was much smaller than at higher temperatures. Figure 4.6 illustrates growth rate as a function of biomass yield. Fe(III)-based growth rate correlated inversely with biomass yield with an R^2 of 0.86. O_2-based growth rates did not show a correlation with biomass yield ($R^2 \ll 0.01$).

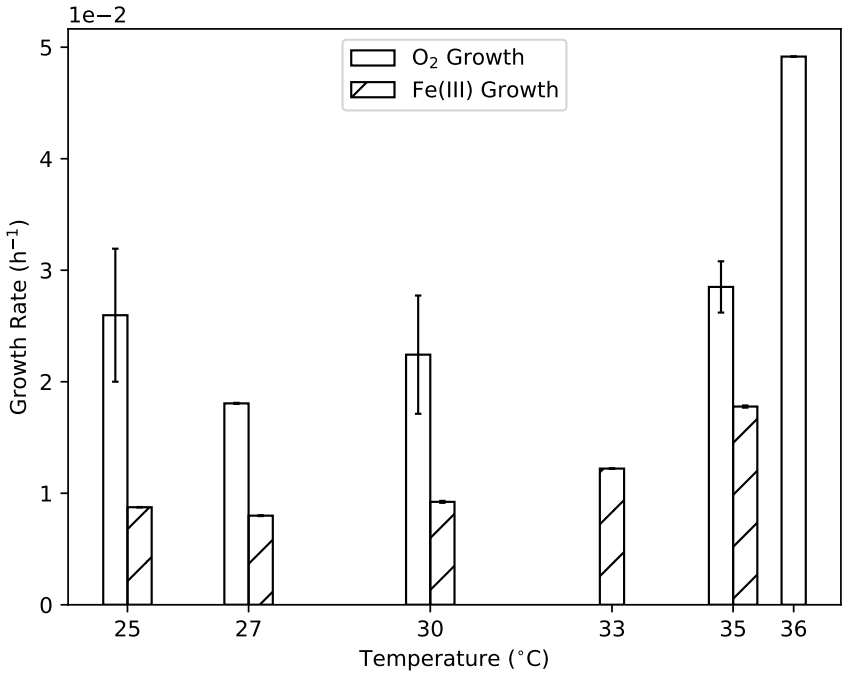

Figure 4.5: Growth rates for each experimental condition. Error bars reflect standard deviation between replicate experiments.

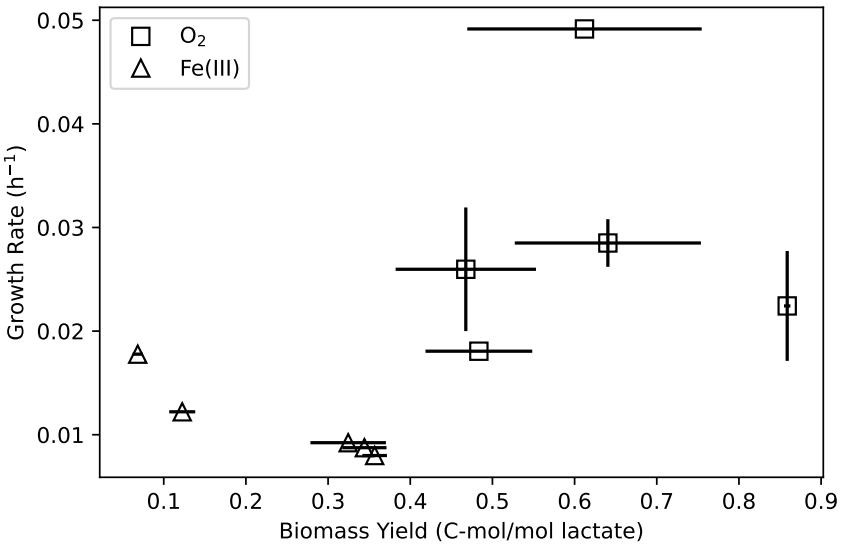

Figure 4.6: Growth rates as a function of biomass yield. Error bars reflect standard deviation between replicate experiments.

4.4 Discussion

4.4.1 Temperature impacts

For both growth strategies, an upper limit of growth temperature was established. For O_2 growth, growth was not observed above 38°C. For Fe(III) growth, 35°C was the maximum temperature. It is notable that the growth strategies yielded different temperature limits, though they are quite close, and likely reflects differences in the physiological underpinnings of those metabolisms. Specifically, the temperature limits for those growth strategies may differ because different enzymes are required for O_2 and Fe(III) growth (Myers & Myers, 1993; Blakeney et al., 2000a). However, due in large part to the complex nature of electron transfer across the cell envelope and the multiple cytochromes that are thought to be involved for CN32 (Blakeney et al., 2000b), few details regarding the exact enzymes involved in O_2 and Fe(III) growth have been quantified. Despite these limits, since temperature limits for growth often depend on limits to enzymatic activity (Daniel, 1996), we can infer a similar effect for CN32.

Another factor that may influence growth temperature limits is the growth media. Moreover, since the growth media was different for aerobic and Fe-based growth (in lactate concentration and Fe(III) versus O_2 presence) those differences must be considered when comparing the data. For both media, the ionic strength was ca. 0.04 M. There is some evidence that increasing ionic strength can yield a higher temperature limit for bacterial growth (Nichols et al., 2000). This suggests that if salt concentrations in the media were increased, the temperature limit might also increase. While the Fe(III)-based experiments had a slightly higher ionic strength (0.045 M versus 0.041 M for O_2 experiments) due to the higher concentration of lactate and the ionic nature of the electron acceptor, that difference is much smaller than those that have been observed to incur temperature limit impacts. Therefore, the ionic strength difference between the two grow media was likely not large enough to influence the temperature limits for growth.

The clear relationship between temperature and thermodynamic efficiency for both O_2-

and Fe(III)-based growth indicates that allocation of the energy produced in catabolism also changes with temperature. Because efficiency is defined by the proportion of Gibbs energy used in anabolism, that allocation of energy reflects its relative use in the production of new biomass (anabolism) versus other non-growth processes. Moreover, loss of efficiency can also correlate to increased production of exudates, as the total C-mol of biomass produced was based on cell counts rather than total organic carbon. The production of biofilms in bacteria, specifically, has been shown to increase with a decrease in temperature (Burman & Bengtsson-Palme, 2021), which would lead to a loss of efficiency at lower temperatures. Our aerobic data are consistent with this from 27 – 30°C while the anaerobic data are not. This may indicate that biofilm production is happening predominantly in the aerobic system. At higher temperatures, expenditure of energy to maintain sufficient cellular functioning, rather than to reproduce, may explain the statistically significant decrease in thermodynamic efficiency above 30°. As has been previously shown, protein instability and aggregation, along with membrane fluidity, increase with temperature, thereby affecting cellular homeostasis (Schramm et al., 2019; de Mendoza & Cronan, 1983). These changes require the cell to overcome that physiological stress to maintain its internal functions, likely resulting in increased energy use.

4.4.2 Gibbs energy partitioning

The partitioning of Gibbs energy yielded from catabolism into the enthalpy (ΔH_{inc}) and entropy ($T\Delta S_{inc}$) during incubation according to Equation 5.2 is illustrated in Figure 4.7. $T\Delta S_{inc}$ is calculated directly from the ΔG_{inc} and measured values of ΔH_{inc}. These values are compared to the standard state values for both O_2- and Fe(III)-based growth, for 1 C-mol of biomass and adjusted to the temperatures investigated. For O_2 growth, ΔG_r° is slightly more negative than ΔH_r°. This predicts that the entropic component of growth (ΔS_r°) is minimal. The data show a reverse trend; ΔH_{inc} is more negative than ΔG_{inc}. When the difference between ΔH_{inc} and ΔG_{inc} is minimized at 30°, the most efficient growth is

observed. This suggests that reactions occurring that cause a decoupling of the anabolic cycle from the catabolic cycle (i.e., reactions associated with maintenance, production of exudates, and similar processes) are exothermic. It is also clear that standard state predictions of how Gibbs energy is partitioned during growth can vary substantially from actual incubations.

Standard state predictions of growth on Fe(III) shows the same general trend as oxygen (ΔG_r° more negative than ΔH_r°), but the magnitude of that difference is much greater. Consequently, the entropic component of growth is predicted to be more significant. This can be conceptualized by considering the metabolite stream during growth. The production of small metabolites would increase entropy during growth, thus helping drive ΔG_r° negative (Von Stockar & Liu, 1999). The data do not show a significant entropic component during incubation; that is ΔH_{inc} is very similar to ΔG_{inc}. ΔH_{inc} is closer to standard state predictions than ΔG_{inc} and growth efficiency is maximized when the difference between standard state predictions and the data are minimized (i.e., at 30°C and below).

Standard state predictions represent an ideal growth scenario with maximum coupling between the anabolic and catabolic cycle. Experimental incubations, however, introduce multiple energy consuming non-growth processes, such as cellular maintenance and the production of exudates, that do not result in new cell production. As a result, measured thermodynamic potentials diverge from predicted thermodynamic potentials. We can, therefore, infer the relative activity of those processes by the magnitude of that divergence. As efficiency decreases, the coupling between the catabolic and anabolic processes becomes weaker as non-growth processes increase. Moreover, the extent of non-growth processes varies, making the entropic component of growth difficult to predict with a standard state system. The growth conditions in which efficiency is maximized will come the closest to standard state predictions, but non-growth processes will still introduce deviations. Despite this, the comparative trends in ΔH_{inc} and thermodynamic efficiency suggest that comparisons between calorimetric measurements and standard state predictions of

the enthalpy of growth can be used to evaluate growth efficiency, as originally proposed by von Stockar et al. (1993).

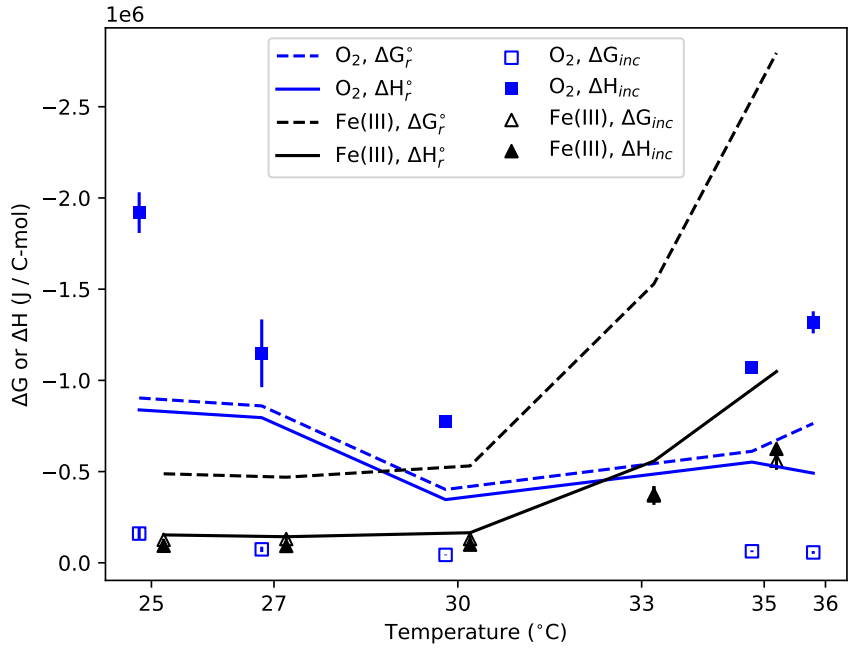

Figure 4.7: Standard state and measured values for ΔG and ΔH for both growth strategies at each temperature investigated. Error reflects standard deviation between replicate samples.

4.4.3 O_2 vs. Fe(III) growth

An important result from this work is the contrast between thermodynamic efficiency for O_2 and Fe(III) growth as a function of temperature. As mentioned above, a possible explanation lies in the fact that CN32 is capable of producing biofilm, which is a mixture of cells and a matrix of extracellular polymeric substances. Biofilm production is important to consider because the enthalpy of its formation is measurable by calorimetry (Peitzsch et al., 2008; Das, 2021) and consumption of electron donors and acceptors is necessary to yield energy for that formation (Speers & Reguera, 2012). Therefore, if biofilm production is not measured and taken into account when calculating the total C-mol biomass produced, the

thermodynamic efficiency values will be impacted. While macroscopic instances of biofilm were not observed, biofilm is typically observed by scanning electron microscopy (Alhede et al., 2012). Smaller biofilms may have been missed with the flourescence microscopy used in this study. Thus, biofilm production may have occurred in our experimental cultures and impacted thermodynamic efficiency calculations. Moreover, two of the variables that influence biofilm production were included in these experiments: O_2 and elevated temperatures.

For *Shewanella* strains in particular, the presence of O_2 has been shown to dramatically increase biofilm production (Wu et al., 2013). In contrast, elevated temperature has been demonstrated to reduce biofilm formation in other taxa (Yan et al., 2020; Pinel et al., 2021). Therefore, at lower temperatures, where oxygen solubility is also higher, biofilm production may have occurred to a high enough degree that it altered the calorimetric signal and Gibbs energy of incubation. At higher temperature, this effect could be minimized. Therefore, higher growth efficiencies, when normalized to a C-mol value derived solely from cell counts, would be predicted at higher temperatures. This was observed 30°C and higher.

In the Fe(III) growth experiments, we would expect less, if any, biofilm production. This is consistent with the observed consistency in growth efficiency at 30°C and below. This does not, however, explain the loss of efficiency with Fe(III)-based growth at higher temperature. Temperature is known to impact Fe(III) reduction rates and the bioavailbility of solid phase Fe(III). Aromokeye et al. (2018) found that the ability of iron-reducing bacteria to use solid phase Fe(III) and Fe(III) reduction rates increased with a decrease in temperature. Consequently, the decrease in thermodynamic efficiency at elevated temperature is, at least in part, likely related to the ability of CN32 to access Fe(III).

Characterizing Fe(III)-based growth of *S. putrefaciens* sp. is essential to predict its influence on geochemical conditions. A key component for making geochemical predictions is representing growth with a chemical equation that reasonably reflects the observed consumption and production of substrate and metabolites, respectively. For example, Equa-

tion 4.15 illustrates the established stoichiometry for Fe(III) growth by *S. putrefaciens* as described in Lovley (1993). This stiochiometry has been applied without verification (Tran et al., 2020).

$$C_3H_5O_3^- + 4Fe^{3+} + 2H_2O = C_2H_3O_2 + HCO_3^- + 4Fe^{2+} + 5H^+ \tag{4.15}$$

The measurements made in this work, however, are consistent with a very different reaction stoichiometry (see Equation 4.11). Geochemical predictions of Fe(II) production based on Equation 4.15 would over-predict production by approximately 2.5 times according to the present work. Moreover, if the overall growth reaction is considered relative to Equation 4.15, that over-prediction of Fe(II) becomes closer to 3 times according to the present work. These differences are substantial and could alter geochemical predictions of mineral phase stability, redox conditions, ionic strength, and similar variables. Consequently, verification of reasonable chemical equations of microbial growth are critical to accurate geochemical modeling.

4.5 Conclusions

In this work, we presented the first quantitative comparison of aerobic and anaerobic growth by CN32. Through a combination of calorimetric analysis and measured changes to a defined growth medium, we described the bioenergetics of those growth strategies. Those data demonstrated a contrasting effect of temperature on thermodynamic efficiency between aerobic and anaerobic growth, which is likely explained through varied biofilm production and Fe(III) bioavailability and reduction rates. Comparisons between incubation enthalpies and Gibbs energies revealed additional nuances in growth efficiency and were counter to standard state predictions. This demonstrates the necessity of direct bioenergetic measurements, as variables that are difficult to predict, such as cell maintenance energy, directly affect that efficiency. This work also provides a stoichiometric description of both growth strategies. Those values are in juxtaposition with previously applied, theoretical, stoichiometries. This further motivates continued application of measured bioenergetics, as the use of theoretical growth stoichiometries may lead to inaccurate predictions regarding the effects of that growth. In all, this work provides data crucial to accurately describing the growth of a common subsurface bacterium, under a ranges of conditions, and advances our understanding of its role in both oxygenated and anaerobic systems.

Chapter 5

BIOENERGETIC EFFECTS OF H_2 LIMITATION AND TEMPERATURE ON *METHANOCALDOCOCCUS SP.* FS406-22

Co-authored by Addien C. Wray and Drew Gorman-Lewis

Abstract

It is widely thought that some of the earliest life used a metabolic pathway broadly similar to the hyperthermophilic archaean *Methanocaldococcus sp.* FS406-22 (hereafter FS406), found today at hydrothermal vents, wherein methane is produced through the oxidation of molecular hydrogen. To better understand the energetic requirements of evolutionarily old metabolic processes like hydrogen oxidation, analysis of the thermodynamics of those microbes is both necessary and notably underexplored. FS406 is an ideal candidate for expanding our knowledge in this area due to its metabolic plasticity, where it is capable of growth over a wide range of temperatures and pressures. In this work, we quantified the bioenergetics of methanogenic growth by FS406 at three temperatures (65, 76, and 85°C). We investigated growth across a range of hydrogen partial pressure (0.4 – 0.8) to impose substrate-limiting conditions and produce a range of biomass yields. This also allowed us to investigate the stress response of FS406 and relate the thermodynamic characterization to growth efficiency. Results showed that growth was most efficient at 76°C with the highest partial pressure of hydrogen. Growth efficiency at 65 and 85°C was similar across the nutrient conditions investigated. Decreased growth efficiency correlated with decreased biomass yield, and increased heat production during incubation. The data clearly showed that the partitioning of Gibbs energy dissipation into enthalpy and entropy changed as non-growth reactions increased during incubation. Increased cellular maintenance (i.e., non-growth reactions) was characterized by an increase in the enthalpy

of incubation, which suggest that non-growth reactions are highly exothermic. The enthalpy of incubation normalized to substrate consumption was determined to range from -34 to -46 kJ/mol with peak growth efficiency characterized with a heat dissipation of -39 kJ/mol. This work provides new insights into the thermodynamic underpinnings of a metabolically ancient hydrothermal vent archaean and helps to better constrain the energetic requirements of early life.

5.1 Introduction

The exact parameters of the metabolisms employed by early life are not known. However, it is possible to put some constraints on what pathways may have been energetically feasible. This constraint-focused approach has been applied to variety of ecological niches, such as marine sediments and extreme habitats, and has been used to estimate, more broadly, energetic maxima and minima for microbial life (e.g., Lane, 2014; LaRowe & Amend, 2015; Kempes et al., 2017; Merino et al., 2019). This understanding is rooted in our knowledge of the geochemical conditions of those systems. For the early Earth, the high concentrations of molecular hydrogen suggest that life may have used it as a primary electron donor (Caffrey et al., 2007; Vignais & Billoud, 2007; Peters et al., 2015). The H^+/H_2 electrode potential makes H_2 an excellent electron donor coupled to a variety of electron acceptors. Given that organic carbon was likely not very abundant on early Earth, it is plausible that H_2 oxidation was coupled to CO_2 reduction (Sousa et al., 2018). The Acetyl Co-A pathway of methanogenesis, where H_2 is oxidized and CO_2 reduced in methanogenesis, is widely considered a plausible model for early metabolism (Baross & Hoffman, 1985; Martin et al., 2008; Martin & Sousa, 2016; Weiss et al., 2016; Sousa et al., 2018; Martin, 2020). To place further constraints on that metabolic strategy, we can measure the thermodynamic properties of extant methanogenic microorganisms. Of those, the hyperthermophilic archaean *Methanocaldococcus sp.* FS406-22 (hereafter FS406) is an ideal candidate as it can be cultured *ex situ*, demonstrates a wide variety of metabolic capability (including growth at a range of temperatures and pressures), and is found in hydrothermal vents – themselves possible niches for early life (Mehta & Baross, 2006). Quantification of the bioenergetics that underpins the growth of FS406, however, has not been done.

To date, thermodynamic measurements of methanogenic microbial growth have focused largely on calorimetric measurements of arachaea found in the digestive tracts of cattle (Von Stockar et al., 2000; Liu et al., 2001b). While limited research in this area has included thermophilic archaea (Schill et al., 1999), to the authors' best knowledge, direct

measurements of marine hyperthermophilic methanogenic bioenergetics remain unexamined. Still, these works, along with non-bioenergetic focused research into methanogenic microbes, have helped identify which geochemical variables methanogens are the most sensitive to and, thus, what components may constrain their growth. Of those, electron donor availability and temperature appear to play a significant role in constraining the growth of methanogens (Zinder et al., 1984; Morgan et al., 1997; Reeve et al., 1997; Russell, 2007; Costa et al., 2013; Fuchs et al., 2016; Chen et al., 2020). Missing is a combined comparison of those variables with hyperthermophiles.

Methanogenic hyperthermophilic growth requires microbes to overcome physiological and biochemical effects of temperature. The precise molecular adaptations employed have not been fully characterized, however, survival at extreme temperatures requires cell components (e.g., lipids, nucleic acids, proteins) which are typically heat-sensitive to be chemically altered. For example, archaean membranes contain lipids (diphytanyl-glycerol and di(bithytanyl)-diglycerol) that impart significant temperature resistance (Ramirez et al., 1994), and their DNA double helix contains additional histones which further increase its thermal stability (Reddy & Suryanarayana, 1988). In addition, for growth at extreme temperatures, the enzymes responsible for metabolic processes need to be both stable and able to react. To avoid irriversible denaturation at high temperatures, hyperthermophilic enzymes are typically folded into very stable conformations (Gavrilov et al., 2016). The rate of reaction for thermophilic emzymes is also temperature-dependent, where reactivity rates increase with temperature to a limit, beyond which they react more slowly (Danson et al., 1996). At mesophilic temperatures the fleixbility of those enzymes may also decrease (Danson et al., 1996), potentially limiting growth at lower temperatures. Overall, while these adaptations allow microbes to survive, and even grow, at elevated temperatures, that effect is varied, where growth is typically optimized at a temperature below the absolute limit for growth of a particular strain (Stetter, 1999). Thus, growth characteristics of methanogenic hyperthermophiles, and their bioenergetics need to be considered across a

range of temperature.

That thermal spectrum is also highly relevant to the availability of both the electron donor and acceptor (H_2 and CO_2, respectively) typically used in methanogenesis. Their solubilities are directly affected by temperature and both decrease in solubility with temperature. This may explain the high microbial concentrations in and near the effluent of hydrothermal vents. Some vents produce H_2 and CO_2 in high concentrations, such that aqueous forms of both compounds are still present at high enough concentrations for methanogenic growth, despite the solubility impact of the effluent temperature (Ver Eecke et al., 2012; Konn et al., 2015; Adam & Perner, 2018). Farther from the vent, however, concentrations of H_2 diminishes below the threshold values for *Methanocaldococcus jannaschii* identified by Ver Eecke et al. (2012), likely due to a combination of the gases evolving from the aqueous to gaseous phase and dilution by the surrounding seawater. This is important because methanogenesis requires a high concentration of H_2 relative to CO_2, given its typical reaction of

$$4H_2 + CO_2 = CH_4 + 2H_2O \tag{5.1}$$

where four moles of hydrogen are consumed per mole of CO_2. This means that the availability of aqueous H_2 may be growth limiting farther from the vent. How H_2 concentration affects the bioenergetics of methanogenic hyperthermophiles is clearly important to fully understand that group of microbes, but it has yet to be examined.

An important direction the field of bioenergetics has taken in recent decades is to quantify growth according to the equation:

$$\Delta G = \Delta H - T\Delta S \tag{5.2}$$

where ΔG is the change in Gibbs free energy, ΔH is the enthalpy of growth, and TΔS is the entropic change incurred from growth (Von Stockar & Liu, 1999; Heijnen & Kleerebezem, 2010; González-Cabaleiro et al., 2019; Hart & Gorman-Lewis, 2021). Certain studies have

focused on quantifying all three of these terms, which provides a more complete picture of the growth process than relying on ΔH measurements alone (e.g., Von Stockar & Liu, 1999; Heijnen & Kleerebezem, 2010; González-Cabaleiro et al., 2019; Hart & Gorman-Lewis, 2021). Furthermore, that approach allows for growth to be described in terms of its driving force. That means that we can determine whether growth is primarily enthalpy-derived, entropy-derived, or a combination. This approach has produced intriguing results, such as the identification of entropy-retarded growth (Von Stockar & Liu, 1999) and the first identification of endothermic growth (Von Stockar et al., 2000). Clearly this approach to bioenergetic analysis can yield nuanced descriptions of what parameters constrain growth. The application of it, then, to taxa relevant to early metabolic strategies is key to constraining our understanding of the chemical requirements for that life.

FS406 is an ideal candidate for expanding our knowledge in this area. The metabolic plasticity it exhibits, which includes growth at a wide range of temperatures (up to 92°C) and pressures, also would allow for extrapolation of its bioenergetic constraints to a variety of conditions. The fact that it inhabits hydrothermal vent effluent further increases its relevance to early life. In this work, we quantified enthalpy, Gibbs energy consumption, and entropy of FS406 growth at a range of temperatures (65-85°C) and H_2 partial pressures (0.4-0.8). These data ultimately improve our understand of the bioenergetic requirements of methanogenesis and place constraints on the thermodynamic underpinnings of early life.

5.2 Materials and Methods

5.2.1 Culture preparation

FS406 was maintained on 5 mL of a defined growth medium (Mehta & Baross, 2006) at 65°C. Cultures were grown to stationary phase (24 h, ±4 h) and maintained with a 4% inoculum. Experimental cultures were prepared such that initial biomass concentration was 1.0 μg/mL ($\pm$0.05). In an anaerobic chamber with an N_2:H_2 atmosphere (98:2), 2.5 mL aliquots were added to 4.22 mL borosilicate glass vials sealed with butyl rubber septum type stopper and aluminum sealing rings. The headspace of each vial was then sparged with an 80:20 H_2/CO_2 gas mixture. The sparging pressure was equal to the pressure of the H_2/CO_2 for the experiment (either 1.21, 1.53, or 2.38 atm). 1.21 atm vials were sparged for 30 seconds while the higher partial pressure vials were sparge for 10 seconds. It was assumed that sufficient removal of the headspace gas was obtained such that it would not impact our measurements. Each vial was then pressurized to either 1.21, 1.53, or 2.38 atm with the H_2/CO_2 mix. The lower two pressure vials were then brought to 2.38 atm total pressure with pure CO_2. The resulting vials were all at 2.38 atm, with H_2 partial pressures of 0.4, 0.5, and 0.8. H_2 partial pressure was varied to achieve a range of biomass yields.

5.2.2 Calorimetric analysis

Calorimetric measurements were made by growing 2.5 mL cultures of FS406 in 4.2 mL glass vials, sealed with butyl rubber septa and aluminum sealing rings, in a TAM III nanocalorimeter that measures heat flux between a reaction and reference vessel as a function of time (Johansson & Wadsö, 1999; Goldberg & Wadsö, 2001). Calorimetric response was calibrated by electrical heating and verified by measuring protonation of TRIS at 25°C (Grenthe et al., 1970). The total heat evolved during growth was measured by monitoring heat flux in the calorimeter throughout the growth period, and the integrating under the resulting curve.

5.2.3 Overall growth reaction modeling

The systems investigated in this work related to growth of FS406 under controlled conditions in reaction vials. From this point forward, we refer to changes in the reaction vials as a result of microbial growth as "incubation" to recognize that abiotic or biotically influenced abiotic reactions will also occur. Simplified macrochemical equations to represent cell growth were used according to Heijnen & Kleerebezem (2010). Those equations are based on the production of one carbon-mole of generic biomass, according to the formula $CH_{1.8}O_{0.5}N_{0.2}$ (Heijnen & Kleerebezem, 2010; Calabrese et al., 2021). The anabolic and catabolic components of the growth reaction were represented according to Equations 5.3 and 5.4. The coefficients for the anabolic and catabolic reactions were determined by solving a series of linear equations to satisfy balances of mass and charge.

$$Y^{an} = a \cdot e^{-}donor + b \cdot Nsource + c \cdot H^{+} + d \cdot H_2O + e \cdot CO_2 + f \cdot oxidizede^{-}donor + CH_{1.8}O_{0.5}N_{0.2} \quad (5.3)$$

$$Y^{cat} = g \cdot e^{-}donor + h \cdot e^{-}acceptor + i \cdot oxidizede^{-}donor + j \cdot reducede^{-}acceptor \quad (5.4)$$

To produce sufficient energy to drive anabolism, the catabolic reaction needs to be performed multiple times. That relationship defines the catabolic multiplicative factor necessary to produce one C-mol of biomass, f_{cat}, as described in Equation 5.5

$$f_{cat} = \frac{-1}{Y_{X/D}} + Y_D^{an} \quad (5.5)$$

where $Y_{X/D}$ is the C-mol biomass produced per mol of e^{-}donor consumed and Y_D^{an} is the anabolic coefficient of the e^{-}donor.

From Equations 5.3 – 5.5 we can calculate the coefficients for the overall growth reaction (OGR) with Equation 5.6:

$$Y^{OGR} = Y^{an} + f_{cat} \cdot Y^{cat} \tag{5.6}$$

5.2.4 Gibbs energy of incubation

The Gibbs energy change during incubation was calculated for each experiment before and after growth based on activities of all the chemical species in the overall growth reaction. Measurements of pH and H_2 were made with an Orion 8103BN Ross semi-micro combination pH electrode and a Unisense Clark-type hydrogen microelectrode, respectively. Methane in the headspace was measured by a Shimadzu GC2030 gas chromatograph using a GS-CARBONPLOT column and flame ionizing detector. CO_2 loss was assumed to be in stoichiometric parity with methane, according to Equation 5.1. Standard states for this work at all temperatures and pressures are unit activity of the pure solvent, unit activity of aqueous species in a hypothetical 1 molal solution referenced to infinite dilution, unit activity of the pure minerals or other crystalline solids, and unit fugacity of a pure gas at 1 bar. The standard state Gibbs energies of formation (ΔG_f°) for the chemical species in the growth reaction were calculated at the experiment temperature with the revised Helgeson-Kirkham-Flowers (HKF) equations of state (Helgeson et al., 1978, 1981; Tanger & Helgeson, 1988) using SUPCRT92 (Shock et al., 1989; Johnson et al., 1992). For biomass, $\Delta G_f^\circ = -67$ kJ/mol was used for all growth experiments (Heijnen & van Dijken, 1992). The standard state Gibbs energies of reactions (ΔG_r°) of the overall growth reaction determined for each experiment were calculated using Equation 5.7, where $\Delta G^\circ_{f,products}$ and $G^\circ_{f,reactants}$ are the standard state Gibbs energies of formation for the products and reactants of the growth reaction, respectively, and Y_i^{ogr} is the stoichiometric coefficient of the ith chemical species in the overall growth reaction.

$$\Delta G_r^\circ = \sum(\Delta G_{f,products}^\circ \times Y_i^{ogr}) - \sum(\Delta G_{f,reactants}^\circ \times Y_i^{ogr}) \tag{5.7}$$

The change in Gibbs energy of a given chemical reaction represents the Gibbs energy potentially available for microbial growth. This is defined by Equation 5.8, where ΔG_r° is modified with the concentration-dependent reaction quotient (Q), the universal gas constant (R), and absolute temperature (T).

$$\Delta G = \Delta G_r^\circ + 2.3026 \times R \times T \times log(Q) \tag{5.8}$$

Q was calculated according to Equation 5.9, where a_i is the thermodynamic activity of the i^{th} chemical species in the overall growth reaction (r) and $v_{i,r}$ is the stoichiometric coefficient for that species.

$$Q = \Pi a_i^{v_{i,r}} \tag{5.9}$$

Activities of the aqueous species were calculated using PHREEQC (Parkhurst & Appelo, 1999). Activity of biomass in solution was converted from molality (C-mol/kg solvent) assuming an activity coefficient of 1 (Tebes-Stevens et al., 1998; Xu et al., 1998; Parkhurst & Appelo, 1999). Overall Gibbs energy change during incubation, ΔG_{inc}, for each experiment was calculated with Equation 5.10 as the difference between initial ΔG_r available ($\Delta G_{r,initial}$), calculated from the initial chemical composition of the medium solution and biomass, and final ΔG_r available ($\Delta G_{r,final}$), calculated from the final chemical composition of the medium solution and biomass.

$$\Delta G_{inc} = \Delta G_{r,initial} - \Delta G_{r,final} \tag{5.10}$$

5.3 Results

Results are presented as a function of biomass yield (C-mol per mole H_2 consumed). Biomass yield varied between approximately 1.5×10^{-3} and 5.8×10^{-3} C-mol per mole H_2 consumed. Figures 5.1 and 5.2 illustrate ΔH_{inc} and ΔG_{inc}. Overall, heat production decreases with biomass yield, with an R^2 of 0.90. At each temperature, the greatest ΔH_{inc} correlated with the lowest biomass yield. At 76 and 85°C, the smallest ΔH_{inc} value also correlated with the greatest biomass yield. A very similar trend was also observed when comparing ΔG_{inc} to biomass yield; ΔG_{inc} decreases with biomass yield and has an R^2 value of 0.90. This trend which is also observed at each temperature individually.

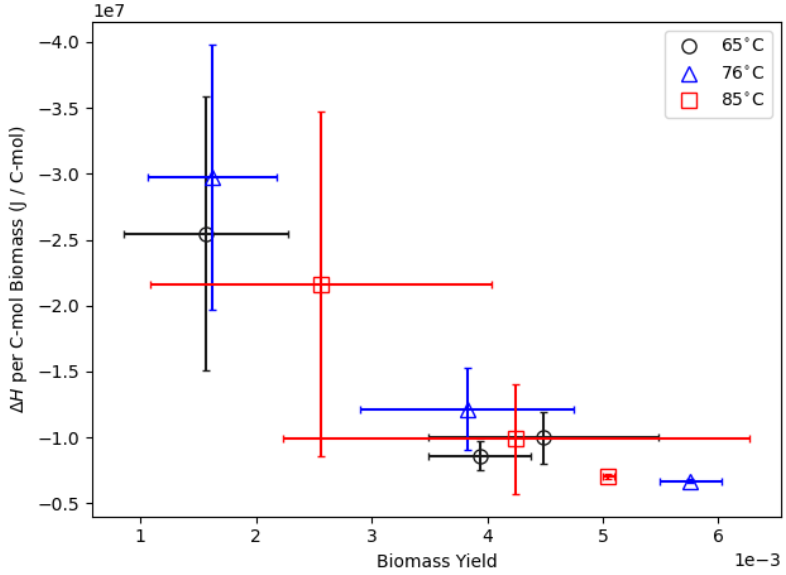

Figure 5.1: Enthalpies of growth under each condition, normalized to C-mol biomass produced, compared to biomass yield (C-mol per mol H_2. Error bars reflect standard deviation between replicate experiments.

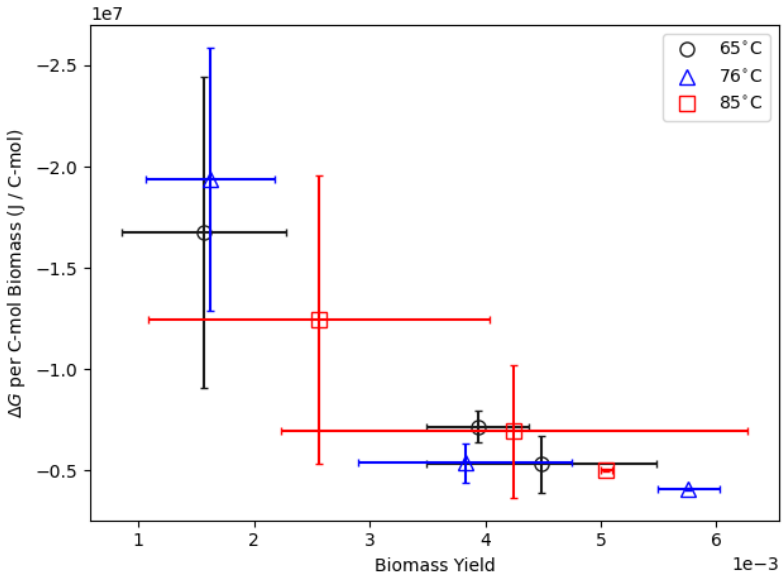

Figure 5.2: Gibbs energy consumed during incubation under each condition, normalized to C-mol biomass produced, compared to biomass yield (C-mol per mol H_2). Error bars reflect standard deviation between replicate experiments.

Methane production varied across experimental conditions and is illustrated as a function of biomass yield in Figures 5.3 and 5.4. A trend emerged with methane production normalized to C-mol biomass produced, with an R^2 of 0.88. Biomass yield was largest when methane produced per C-mol biomass was smallest. When methane produced is normalized the H_2 consumption no clear trends are evident (R^2 = 0.08).

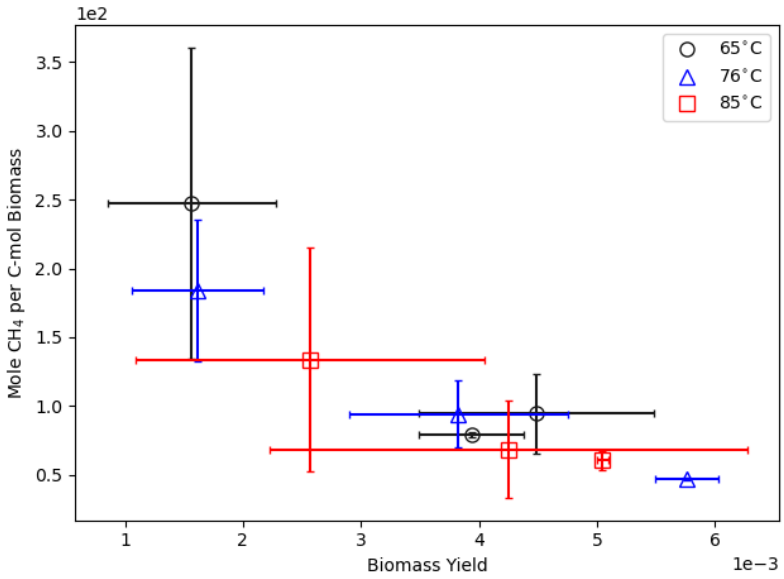

Figure 5.3: Methane produced under each condition, normalized to C-mol biomass produced, compared to biomass yield (C-mol per mol H_2). Error bars reflect standard deviation between replicate experiments.

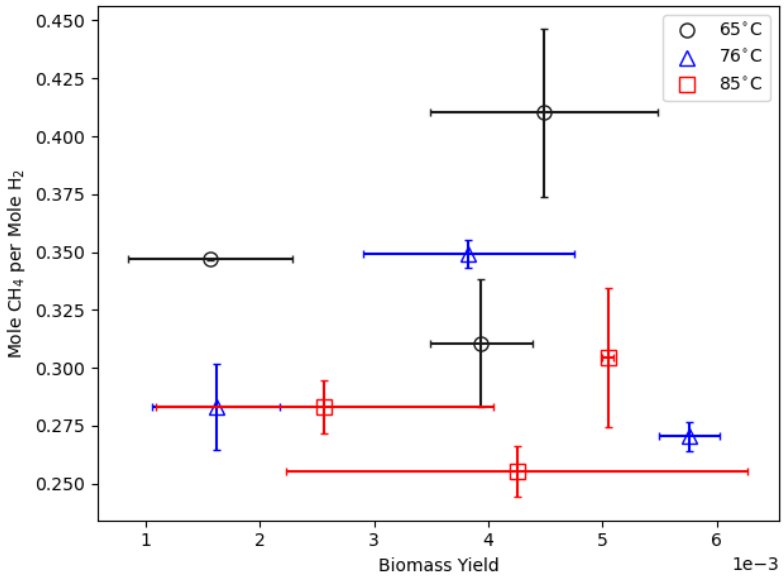

Figure 5.4: Methane produced under each condition, normalized to H_2 consumed, compared to biomass yield (C-mol per mol H_2). Error bars reflect standard deviation between replicate experiments.

Averaged growth rate at each temperature is illustrated in Figure 5.5. The maximum growth rate was achieved at 76°. Growth rate as a function of biomass yield is shown in Figure 5.6, and no clear trend emerges (R^2 = 0.18). What does become clear in Figure 5.6 is that the highest growth rate produced a biomass yield of ≈ 0.004 C-mol / mol H_2, which is approximately the median biomass yield produced across the experimental conditions.

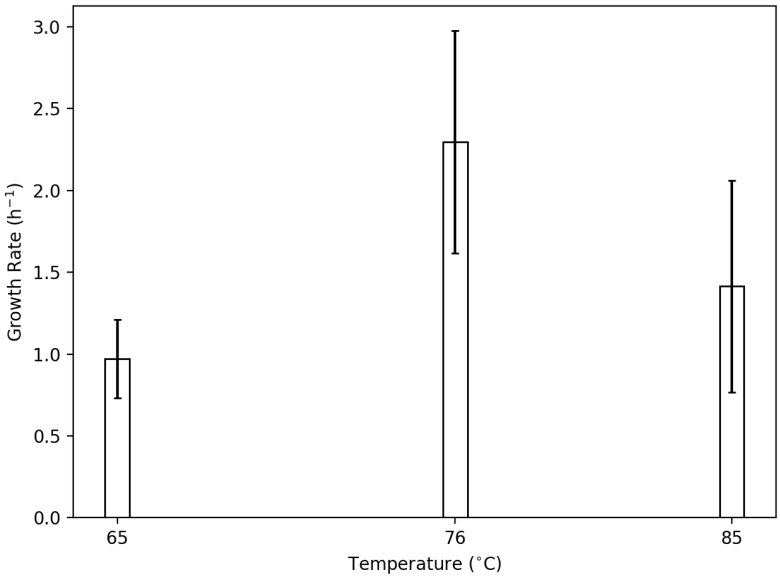

Figure 5.5: Growth rate of each temperature condition. Error bars reflect standard deviation between all experiments at each temperature.

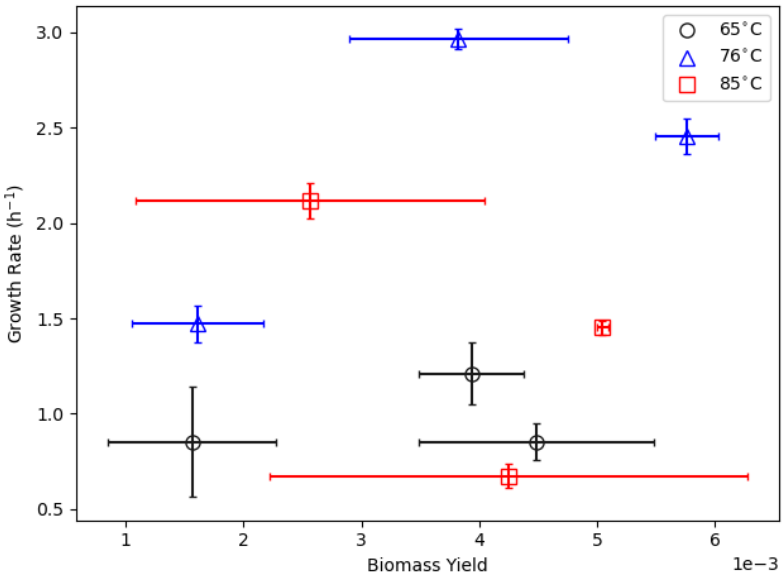

Figure 5.6: Growth rates, compared to biomass yield (C-mol per mol H_2). Error bars reflect standard deviation between replicate experiments.

5.3.1 Growth stoichiometry

We determined the catabolic reaction based on Equation 5.4 and constraints provided by changes to the growth media, as shown in Equation 5.1. The ratio of CO_2 consumed per mole of H_2 oxidized was 0.25 mole. The anabolic reaction, solved according to Equation 5.3, involved the conversion of H_2, CO_2, ammonium, and protons into biomass. The unscaled overall growth reaction, as determined by summing Equations 5.1 and 5.11, is shown in Equation 5.12. That reaction predicts 0.33 moles of CO_2 to be reduced per mole H_2. The observed ratio of CO_2:H_2 in the experiments was 0.28 $\pm$0.05. This is between the predictions for the catabolic and overall growth reactions, reflecting the measurable influence of anabolism on the relative concentrations of H_2 and CO_2.

$$2.1H_2 + CO_2 + 0.2NH_4 = CH_{1.8}O_{0.5}N_{0.2} + 1.5H_2O + 0.2H^+ \tag{5.11}$$

$$6.1H_2 + 2CO_2 + 0.2NH_4 = CH_{1.8}O_{0.5}N_{0.2} + CH_4 + 3.5H_2O + 0.2H^+ \tag{5.12}$$

5.4 Discussion

5.4.1 Growth Efficiency

A common approach for energetic calculations and comparisons of biological data is to normalize those data to the total amount of biomass produced (Schill et al., 1999; Liu et al., 2001a; Hart & Gorman-Lewis, 2021). This can be taken as the total number of cells produced, or, as done in this work, the moles of organic carbon produced according to a simplified chemical formula for biomass (Heijnen & Kleerebezem, 2010). Normalization to biomass is essential for calculation of the catabolic scaling factor (described above) and to consider trends in thermodynamic potentials. However, the production of biomass is frequently inconsistent, even under identical conditions, and particularly when cultures produce low biomass (e.g., 3.5 μg dry weight). As a result, the error between replicate experiments can be large. This effect can be seen our data; the experiments that produced the largest biomass yields (greater than 5×10^{-3} C-mol / mol H_2) had the smallest errors. Despite the larger errors associated with biomass normalization, some trends do emerge in the data.

Thermodynamic efficiency is defined as the ratio of the anabolic to catabolic ΔG_{inc} scaled by f_{cat} (Calabrese et al., 2021). Figure 5.7 illustrates efficiency as a function of biomass yield. The varied initial partial pressure of H_2 in the cultures allowed us to gather data across a range of biomass yields through nutrient limitation. This also imparted stress on cultures that resulted in a measurable response. A clear trend is exhibited ($R^2 = 0.98$) where the highest biomass yield shows the most efficient growth. This is an expected trend given that efficient growth connotes a tighter coupling between the catabolic and anabolic reactions (Russell, 2007); thus, more energy liberated by the catabolic cycle is used for biomass production rather than non-growth reactions.

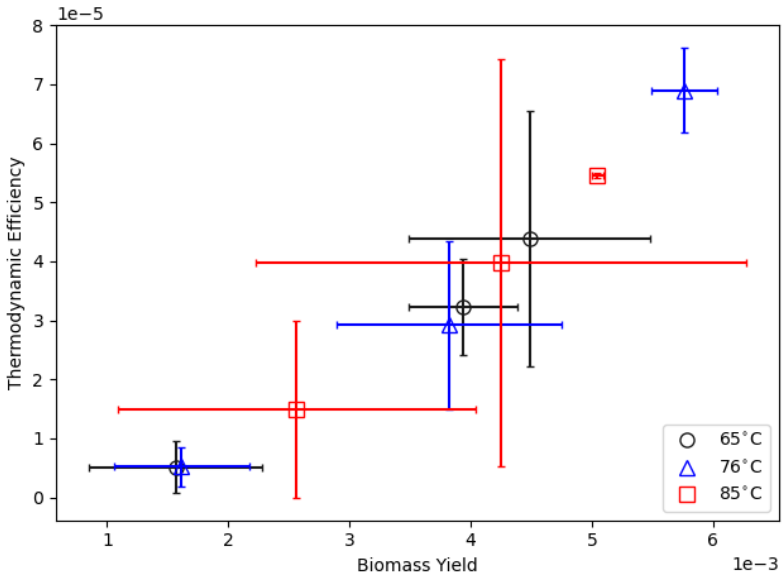

Figure 5.7: Thermodynamic efficiency compared to biomass yield. Error bars reflect standard deviation between replicate experiments.

Examining thermodynamic efficiency as a function of ΔH_{inc} can reveal relationships between biomass production and non-growth reactions that are not discernible by considering ΔG_{inc} alone. As shown in Figure 5.8, a higher ΔH_{inc} correlates with lower thermodynamic efficiency. This is corresponds to an increase in the anabolic reaction decoupling from the catabolic reaction due to non-growth reactions such as turnover of macromolecular compounds, osmoregulation, and many other reactions (Van Bodegom, 2007). Therefore, an increase in decoupled reactions, in turn, corresponds to higher heat production. This implies that these non-growth reactions are predominantly exothermic.

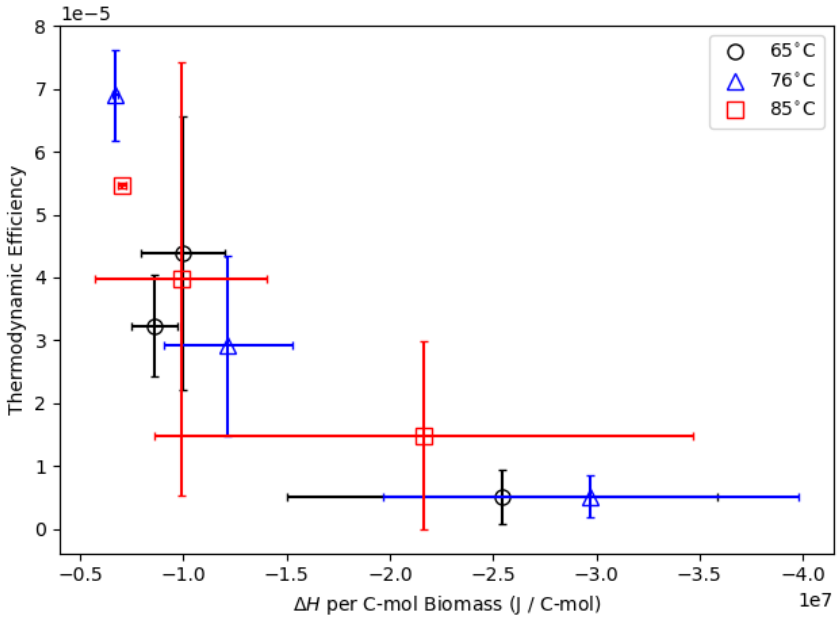

Figure 5.8: Thermodynamic efficiency compared to ΔH_{inc} per C-mol biomass produced. Error bars reflect standard deviation between replicate experiments.

Considering microbial growth according to Equation 5.2, it is clear that the entropic contribution to growth cannot be neglected. The entropic contribution can be conceptualized by considering the metabolite stream during growth. The production of small metabolites would increase entropy during incubation, thus helping drive ΔG_r° negative (Von Stockar & Liu, 1999). The inverse, production of larger molecules or simply the lack of ion or molecules exiting the cell, would decrease entropy and retard growth. $T\Delta S_{inc}$ is calculated directly from the ΔG_{inc} and measured values of ΔH_{inc}. Examining $T\Delta S_{inc}$ as a function of thermodynamic efficiency can further elucidate the relation between non-growth reactions and this thermodynamic potential as shown in Figure 5.9. An observable trend is present, where efficiency decreases with increased entropy (R^2 = 0.76).

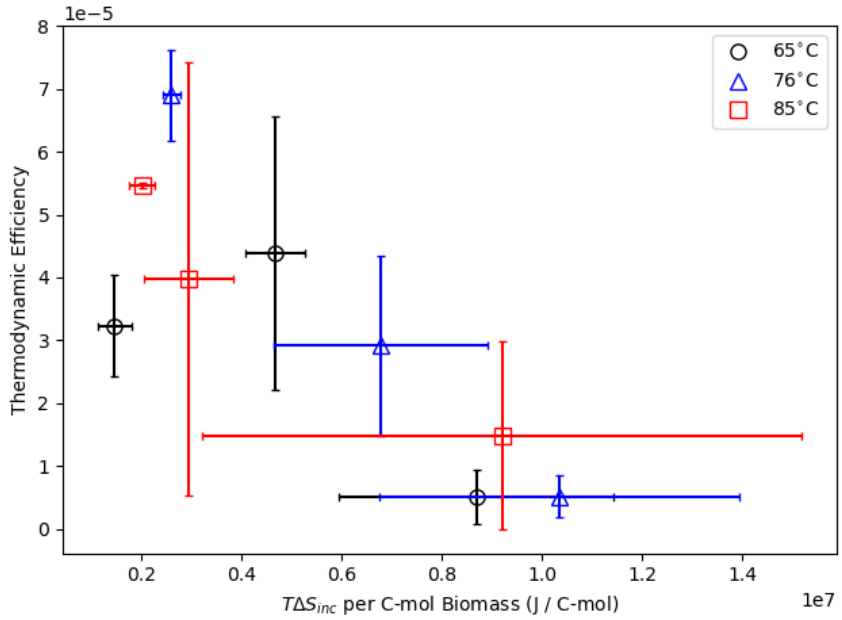

Figure 5.9: Thermodynamic efficiency compared to the entropic component of growth. Error bars reflect standard deviation between replicate samples.

As shown in Figure 5.10, standard state predictions suggest that growth should be slightly entropy-driven (since ΔG is more exergonic than ΔH is exothermic). The observed thermodynamics, however, are in contrast to those predictions and show that entropy is retarding growth (ΔG is less exergonic than ΔH is exothermic). This is likely because standard state predictions do not take into account non-growth reactions. If non-growth reactions do not expel ions or molecules from the cell, then there is a consumption of Gibbs energy and an increase in internal entropy, which can then only be dissipated through heat. The data clearly show this trend with exothermic or enthalpy-driven growth across all conditions. It is notable though, that the data that are closest to standard state predictions are those with the highest biomass yield. These data correspond to the most efficient growth at each temperature. This indicates that as thermodynamic efficiency increases, the magnitude of non-growth reactions relative to growth reactions decreases. Consequently, there is less internal entropy production that needs to be dissipated, and we observe this through less heat production during incubation. The opposite is also observed, where, for cells that

are under the most stress and have the lowest biomass yield, ΔH_{inc} is the large in order to dissipate internal entropy production from non-growth reactions, and this correlates to the greatest discrepancies relative to standard state.

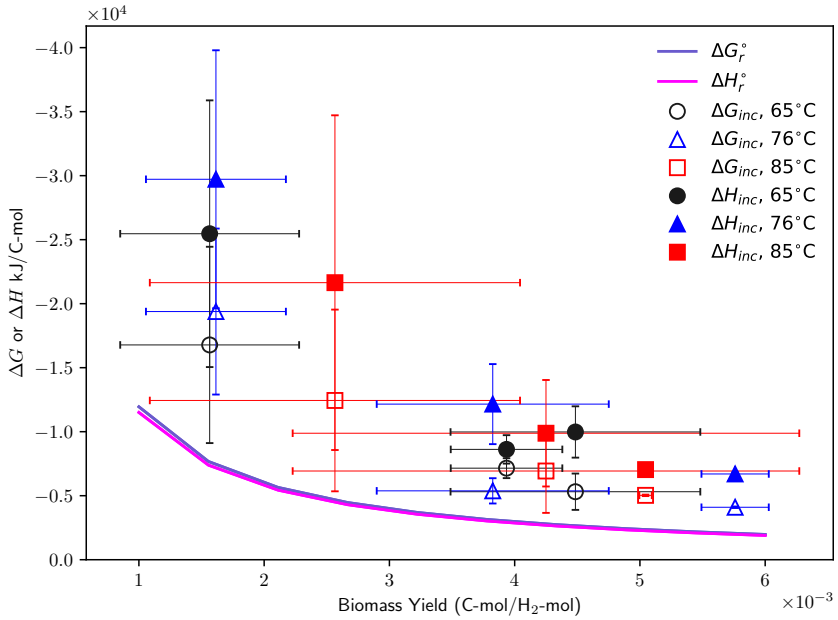

Figure 5.10: Curves represent standard state predictions for enthalpy (ΔH_r°) and Gibbs energy (ΔG_r°) over the range of biomass yield considered. Solid points are ΔH_{inc} and open points are ΔG_{inc} at each temperature. Black is 65°C, blue is 76°C, and red is 85°C. Error bars reflect standard deviation between replicate samples.

5.4.2 Heat Dissipation Limits

Another common approach to energetic comparisons of biological data is normalization to substrate consumption or metabolite production. This approach is also commonly used when understanding geochemical impacts is the primary focus of studies (Smith & Shock, 2007; Amenabar et al., 2017). Combining this normalization strategy with another indicator of efficiency, enthalpy efficiency, can help to elucidate additional details behind the energetics. Enthalpy efficiency, described by von Stockar et al. (1993), is the ratio of the

standard state enthalpy of biomass formation ($\Delta H_x^\circ = -91$ kJ/C-mol, used at all temperatures (Heijnen & van Dijken, 1992)) to the difference between ΔH_x° and ΔH_{inc}. These parameters often have lower errors than parameters involving ΔG_{inc}, because many chemical analysis necessary are necessary for Gibbs energy calculations. Considering the data in terms of enthalpy efficiency versus ΔH_{inc} normalized to H_2 consumed ($\Delta H_{inc/molH}$) reduced the chemical analyses to biomass quantification and H_2, thereby lowering some errors associated with experimental conditions.

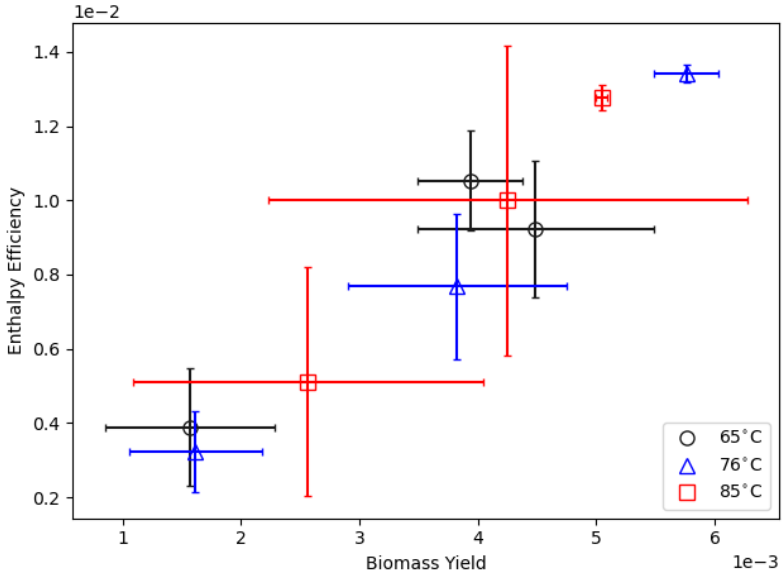

Figure 5.11: Enthalpy efficiency compared to biomass yield. Error bars reflect standard deviation between replicate experiments.

Figure 5.11 illustrates enthalpy efficiency as a function of biomass yield. Enthalpy efficiency follows the same trends as found for thermodynamic efficiency, with maximum efficiency found at 76°C. This suggests it is a suitable parameter to discern impacts of the experimental conditions on growth efficiency. Considering enthalpy efficiency as a function of $\Delta H_{inc/molH}$ provides a view of the data to further characterize how heat production during incubation is related to biomass production. The more biomass that is produced during incubation will produce more heat, which is why normalization of calorimeteric

data is so important, such that meaningful for comparisons can be made across experiments. The correlation of high heat production with low thermodynamic efficiency (Figure 5.8) and low biomass yield (Figure 5.1) are strong evidence that high heat production is associated with reactions that do not produce new biomass. In addition to this clear trend, we can observe some thermodynamic limits on growth that are illustrated in the Figure 5.12 at 65 and 76°C; errors associated with experimental conditions at 85°C do not make similar comparisons possible given the inconsistent growth. We will first consider data at 76°C, where maximum enthalpy efficiency at 76°C correspond with $\Delta H_{inc/molH}$ of approximately -39 kJ/mol. This $\Delta H_{inc/molH}$ value can be regarded as the optimal heat dissipation per mole of H_2 consumed, under our experimental conditions. $\Delta H_{inc/molH}$ increases as enthalpy efficiency decreases, to 0.003 and 0.008, with p-values of 0.04 or less. These experiments have similar values of $\Delta H_{inc/molH}$ (≈ -45 kJ/mol) yet different enthalpy efficiencies. Cells in both experiments clearly experienced stressed relative to the experiment with higher efficiency experiment, and it appears that $\Delta H_{inc/molH}$ of ≈ -45 kJ/mol is an upper limit for heat dissipation, under our experimental conditions, which allows for biomass yields from ≈ 0.0017 to 0.0045 across the temperatures investigated.

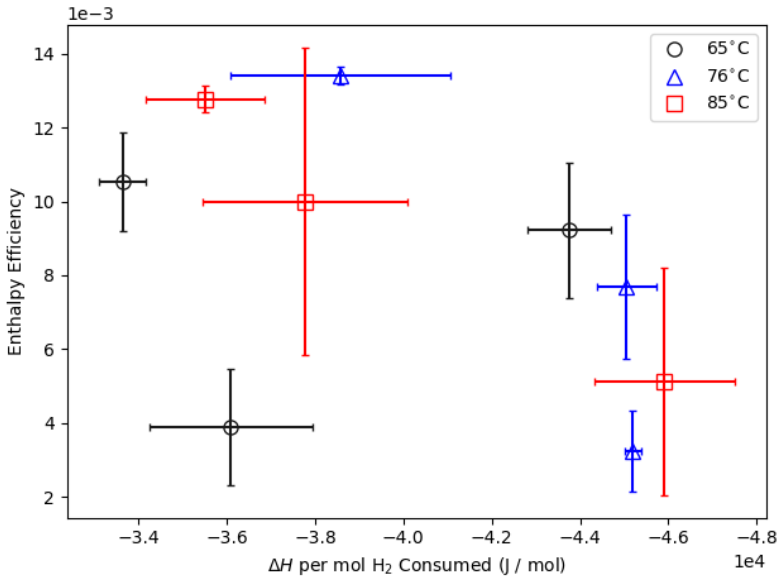

Figure 5.12: Enthalpy efficiency compared to ΔH per mol H_2 consumed. Error bars reflect standard deviation between replicate experiments.

Data at 65°C in Figure 5.12 also show an interesting trend that defines a lower bound on $\Delta H_{inc/molH}$ and agrees with the upper bound at 76°C. The lowest observed $\Delta H_{inc/molH}$ is ≈ -34 kJ/mol and corresponds to an enthalpy efficiency of 0.011. This experiment differs from the experiment with a $\Delta H_{inc/molH}$ of ≈ -36 kJ/mol with a p value of 0.051, which suggests -34 kJ/mol is a lower $\Delta H_{inc/molH}$ bound at 65°C under our experimental conditions. We also observe a similar range in biomass yields ($\approx 0.0017 - 0.004$) at the lower end of $\Delta H_{inc/molH}$ values as observed in the higher limit. The data at 65 and 76°C suggest FS406 is characterized by $\Delta H_{inc/molH}$ values between -34 and -46 kJ/mol. These parameters can be used in future studies to characterize growth of FS406 with calorimetric measurements and measurements of H_2 consumption.

5.5 Conclusions

In this work we have presented, to the authors' best knowledge, the first bioenergetic measurements of a hydrothermal vent dwelling, hyperthermophilic methanogen. Investigations across a range of temperature and H_2-limiting conditions showed that most efficient growth, defined in terms of thermodynamic efficiency and enthalpy efficiency, occurred at 76°C. Unsurprisingly, FS406 exhibited clear stress responses as H_2 availability decreased, which was evident in biomass yield and exceedingly clear in $\Delta H_{inc/molH}$ measurements and $T\Delta S_{inc}$ calculations.

The approach we used in this study begins to lay the foundation for determining the energetic landscape that can support FS406 growth. Calorimetry is the easiest and most direct energetic measurement that is possible to make on microbial cultures; however, context for calorimetric measurements is essential to interpret their meaning. For FS406, direct measurements of H_2 consumption with Clark-type electrodes provides an efficient method to quantify substrate consumption, and provide that essential context to interpret the calorimetric signal. The $\Delta H_{inc/molH}$ values determined in this work make it possible to quickly evaluate growth conditions in relation to maximal growth efficiency observed under our experimental conditions with just calorimetric and H_2 consumption measurements.

To fully contextualize that energetic landscape, additional work is needed across a broader suite of environmental conditions, such as the extreme pressures present on the seafloor. That, more complete, understanding is essential to accurately constrain the energetic requirements of methanogenesis in hydrothermal systems. This has far reaching implications, including characterizing modern-day methane production, establishing the energetic bounds of early life on Earth, and the evaluating the magnitude of habitability of environments beyond it. Ultimately, this work advances that effort and demonstrates key trends in the bioenergetics of growth by FS406 that can help guide future research.

Chapter 6

ASTROBIOLOGICAL CONTRIBUTIONS

The astrobiological impacts of a given set of data can be divided into two categories: what those data tell us about life on Earth and how they can inform our search for life elsewhere. This dissertation addresses both categories by describing how life on Earth has adapted to fill a wide variety of niches as well as the geochemical impacts of their presence, which is a necessary context in which to view our search for life beyond Earth.

In terms of Earth-based life, the data presented here aid our understanding of the origin of life. The emergence of life from abiotic compounds, fundamentally, requires a long-lived energy source. Theories concerning what that source may have been include the possibility of a natural nuclear reactor, where the decay of U-235 produces the heat necessary to catalyze early reactions. Regardless of the habitat, for life to proceed, chemical oxidants and reductants are required. Thus, despite the reducing conditions found on early Earth, that natural nuclear reactor would inherently mix with an oxidant, yielding U(VI). How the first cells interacted chemically with that U(VI) is thus of importance. The data presented here help to constrain the types of such reactions possible on a bacterial surface. Another possible energy source is a hydrothermal system. This work provides energetic constraints on the requirements for a metabolism thought to be employed by some of the earliest life: methanogenesis.

These data also help to improve our understanding of the subsequent diversification and environmental signatures of microorganisms. First, they serve as a foundation for the evaluation of early N-fixation bioenergetics. The dissertation also identifies more accurate stoichiometries of growth for a range of metabolic strategies. Lastly, these data suggest a possible explanation for juxtaposed observations of biosignatures of early life

and the lack of associated organic carbon. It is shown that the catabolic cycle, from which biosignatures are typically derived, may proceed in excess relative to the anabolic cycle under energy-limited conditions. For example, this may help to explain how banded iron formations were formed biologically and yet today have no organic carbon present. An energy-limited environment, which is more likely on early Earth due to the lack of oxygen and overall reducing conditions, in which Fe-oxidizing microbes were growing, could produce a substantial amount of Fe(III) without yielding sufficient biomass for long-term preservation.

For exosystems, this dissertation placed constraints on energetic requirements for aerobic and anaerobic growth, as well as high temperature, hydrothermal growth, which will help us better understand what life could survive in a given system. In addition, it is useful for understanding the magnitude of habitability (i.e., how much biomass could be supported) as it provides a quantification of biomass yield under varied conditions and with different substrates.

The search for life elsewhere must also consider the fact that organisms will impact one another by altering the redox state of the system during growth. Thus, the number and type of metabolic strategies an exosystem can support will partially dictate the amount of biomass and the type of geochemical signatures we may expect. This work addresses such effects primarily by identifying the contrast between theoretical and observed growth stoichiometries. As an organism grows, that stoichiometry will determine how it alters the redox state of its environment, which will directly affect the thermodynamic favorability of other growth strategies. So, knowing the actual impact one organism may have on the growth of another requires an accurate characterization of its growth, and this work provides that context for multiple growth mechanisms. Surficial reactions can have a similar effect, as they can remove, to varying degrees, certain compounds from solution. This work advances our understanding of interactions between microbial surfaces and a heavy metal that can serve both as an energy source and as a toxic inhibitor of life.

Finally, the search for life will always be limited in scope, so we need to understand what evidence is best to look for – products of biological activity or organisms themselves. These data show that the energetic limitations of a given system, as it relates to a metabolism of interest, must be taken into account. An energy-limited system can produce a large quantity of catabolic products (i.e., a biosignature) without yielding much biomass. So, in a system with little available energy, efforts should focus on finding products of microbial catabolism, while a more energy-rich system would motivate the search for biomass. In all, these data suggest that the choice of whether to search for a biosignature or living cells needs to reflect to the energetics of a system.

Chapter 7

CONCLUSIONS

The quantification of microbial thermodynamic properties is essential to characterize and predict interactions between microorganisms and their geochemical environment. The co-application of calorimetric measurements (ΔH) and calculations of the Gibbs energies associated with a reaction of interest (e.g., protonation, metabolism) greatly improves the accuracy of that assessment. Once quantified, these parameters can be used to calculate the entropic component of the reaction. This additional parameter can help describe both how certain geochemical variables affect reactivity (e.g., conformational changes to a functional group) and the driving forces for the reaction (e.g., whether growth is entropy-driven or not). The work described in this dissertation shows that, when taken in concert, assessing all three thermodynamic terms (ΔH, ΔG, and ΔS) improves our ability to describe how the cell surface and its metabolic cycle interact with local geochemistry, from oxic to hydrothermal systems.

Future Directions

This work has demonstrated that the gram-negative bacterium *Shewanella putrefaciens* strain CN32 has a highly reactive surface, with three identifiable functional groups. It has also shown that the reactive potential of the cell surface is measurably impacted by changes in ionic strength – an effect that had previously been poorly constrained in the literature. To expand on these insights, research is needed in multiple directions. For example, the protonation effects of electrolytes with divalent cations would provide additional context for how the surface reactivity may change under more complex conditions. In addition, while it is evident that there is a conformational change on the amine group with changing

ionic strength, these data do not describe the structural alterations to that group involved and should be investigated more thoroughly.

This work has also demonstrated that CN32 can play a vital role in sequestering aqueous U(VI) through surface complexation reactions. Those reactions were found to be strongly impacted by multiple geochemical variables applicable to most environments. These data would be more widely applicable to natural systems if the effect of other divalent cations could be considered. In addition, radionuclide waste streams can often have very high concentrations of U (much more than the 10 μM considered here). Data concerning the impact to cell structure (e.g., possible lysis of the cell) when U concentrations are increased would help us better understand the impact of CN32 in highly enriched sites. Moreover, the kinetics of the adsorption need to be quantified, as the time period over which the U will stay adhered to the cell was not investigated but is necessary for the application of these data to a real-world system. Lastly, the chemical fate of the adsorbed U upon cell death needs to be described. Future work should characterize U geochemistry in concert with lysed and partially lysed cells, as functional groups previously constrained to the interior of the cell may come into play under those conditions.

Beyond describing surface complexation properties, this dissertation provides important context for the growth of CN32, under both oxic and anoxic conditions. Overall, the efficiency of CN32's growth is strongly impacted by temperature, but that impact depends on the metabolism involved, especially at lower temperatures, where O_2-based growth was found to be more sensitive to temperature changes. These data would be strengthened by a thorough quantification of biofilm production in aerobic and anaerobic systems. In addition, since CN32 is known to utilize a wide variety of redox pairs, similar stoichiometric analyses, where the true growth stoichiometries are measured, with redox pairs other than the lactate-O_2 and lactate-Fe(III) considered here, would make the data more broadly applicable to natural systems.

In addition to these bacterial data, this work also provides important constraints on the

growth of a methanogenic archaean, FS406. Those data demonstrated that, while growth is possible over a wide range of temperatures, its efficiency is maximized in the middle of that range. These data are foundational in providing a basis for comparing growth to more energy-taxing conditions, such as a lack of pre-fixed nitrogen. Thus, future work can build directly from these data to understand how additional stress, such as the need to fix N_2, affects bioenergetics.

BIBLIOGRAPHY

Adam, N., & Perner, M., 2018. Microbially mediated hydrogen cycling in deep-sea hydrothermal vents. Front. Microbiol., 9. https://doi.org/10.3389/fmicb.2018.02873.

Adhikari, D., Zhao, Q., Das, K., Mejia, J., Huang, R., Wang, X., Poulson, S. R., Tang, Y., Roden, E. E., & Yang, Y., 2017. Dynamics of ferrihydrite-bound organic carbon during microbial Fe reduction. Geochim. Cosmochim. Acta, 212, 221–233. https://doi.org/10.1016/j.gca.2017.06.017.

Ahmad, M., Kalinina, O., & Lengauer, T., 2014. Entropy gain due to water release upon ligand binding. J. Cheminform., 6, 2014. https://doi.org/10.1186/1758-2946-6-s1-p35.

Alessi, D. S., Henderson, J. M., & Fein, J. B., 2010. Experimental measurement of monovalent cation adsorption onto Bacillus subtilis cells. Geomicrobiol. J., 27, 464–472. https://doi.org/10.1080/01490450903490813.

Alessi, D. S., Uster, B., Veeramani, H., Suvorova, E. I., Lezama-Pacheco, J. S., Stubbs, J. E., Bargar, J. R., & Bernier-Latmani, R., 2012. Quantitative separation of monomeric U(IV) from UO2 in products of U(VI) reduction. Environ. Sci. Technol., 46, 6150–6157. https://doi.org/10.1021/es204123z.

Alhede, M., Qvortrup, K., Liebrechts, R., Høiby, N., Givskov, M., & Bjarnsholt, T., 2012. Combination of microscopic techniques reveals a comprehensive visual impression of biofilm structure and composition. FEMS Immunol. Med. Microbiol., 65, 335–342. https://doi.org/10.1111/j.1574-695X.2012.00956.x.

Amenabar, M. J., Shock, E. L., Roden, E. E., Peters, J. W., & Boyd, E. S., 2017. Microbial substrate preference dictated by energy demand rather than supply. Nat. Geosci., 10, 577–581. https://doi.org/10.1038/NGEO2978.

Anderson, C., Jakobsson, A. M., & Pedersen, K., 2007. Influence of in situ biofilm coverage on the radionuclide adsorption capacity of subsurface granite. Environ. Sci. Technol., 41, 830–836. https://doi.org/10.1021/es0608702.

Anderson, R. T., Vrionis, H. A., Ortiz-Bernad, I., Resch, C. T., Long, P. E., Dayvault, R., Karp, K., Marutzky, S., Metzler, D. R., Peacock, A., White, D. C., Lowe, M., & Lovley, D. R., 2003. Stimulating the in situ activity of Geobacter species to remove uranium from the groundwater of a uranium-contaminated aquifer. Appl. Environ. Microbiol., 69, 5884–91. https://doi.org/10.1128/aem.69.10.5884-5891.2003.

Arnold, T., Utsunomiya, S., Geipel, G., Ewing, R. C., Baumann, N., & Brendler, V., 2006. Adsorbed U(VI) surface species on muscovite identified by laser fluorescence spectroscopy and transmission electron microscopy. Environ. Sci. Technol., 40, 4646–52. https://doi.org/10.1021/es052507l.

Aromokeye, D. A., Richter-heitmann, T., Oni, O. E., Kulkarni, A., & Friedrich, M. W., 2018. Temperature Controls Crystalline Iron Oxide Utilization by Microbial Communities in Methanic Ferruginous Marine Sediment Incubations. Front. Microbiol., 9, 2574. https://doi.org/10.3389/fmicb.2018.02574.

Ayala-torres, C., Hernández, N., & Galeano, A., 2014. Zeta potential as a measure of the surface charge of mycobacterial cells. Anal. Microbiol., 64, 1189–1195. https://doi.org/10.1007/s13213-013-0758-y.

Barbucci, R., & Barone, V., 1979. A rationalization of the enthalpy of protonation of polyamines. J. Solution Chem., 8, 427–438.

Barbucci, R., Barone, V., Micheloni, M., & Rusconi, L., 1981. Thermodynamics of protonation of tetramines with different degrees of N-methylation. J. Phys. Chem., 85, 64–68. https://doi.org/10.1021/j150601a015.

Barbucci, R., & Vacca, A., 1974. Co-ordinating Properties in Aqueous Solution of the Oxygen Atom in Bis- 2-aminoethyl Ether. Dalt. Trans., (p. 2363).

Barnie, S., Zhang, J., Wang, H., Yin, H., & Chen, H., 2018. Chemosphere The in fl uence of pH , co-existing ions , ionic strength , and temperature on the adsorption and reduction of hexavalent chromium by undissolved humic acid. Chemosphere, 212, 209–218. https://doi.org/10.1016/j.chemosphere.2018.08.067.

Baross, J. A., & Hoffman, S. E., 1985. Submarine Hydrothermal Vents and Associated Gradient Environments as Sites for the Origin and Evolution of Life, .

Belli, K. M., DiChristina, T. J., Van Cappellen, P., & Taillefert, M., 2015. Effects of aqueous uranyl speciation on the kinetics of microbial uranium reduction. Geochim. Cosmochim. Acta, 157, 109–124. https://doi.org/10.1016/j.gca.2015.02.006.

Beskok, A., & Pillai, Æ. S. D., 2008. Zeta Potential of Selected Bacteria in Drinking Water When Dead , Starved , or Exposed to Minimal and Rich Culture Media. Curr. Opin. Microbiol., 56, 93–97. https://doi.org/10.1007/s00284-007-9046-z.

Beveridge, T. J., & Koval, S. F., 1981. Binding of metals to cell envelopes of Escherichia coli K-12. Appl. Environ. Microbiol., 42, 325–335. https://doi.org/10.1128/aem.42.2.325-335.1981.

Beveridge, T. J., & Murray, R. G., 1976. Uptake and retention of metals by cell walls of Bacillus subtilis. J. Bacteriol., 127, 1502–1518. https://doi.org/10.1128/jb.127.3.1502-1518.1976.

Beveridge, T. J., & Murray, R. G. E., 1980. Sites of metal deposition in the cell wall of Bacillus subtilis. J. Bacteriol., 141, 876–887.

Bishop, B. A., Flynn, S. L., Warchola, T. J., Alam, M. S., Robbins, L. J., Liu, Y., Owttrim, G. W., Alessi, D. S., & Konhauser, K. O., 2019. Adsorption of biologically critical trace elements to the marine cyanobacterium Synechococcus sp. PCC 7002: Implications for marine trace metal cycling. CHEMICAL GEOLOGY, 525, 28–36. https://doi.org/10.1016/j.chemgeo.2019.05.021.

Blakeney, M. D., Moulaei, T., & DiChristina, T. J., 2000a. Fe(III) reduction activity and cytochrome content of Shewanella putrefaciens grown on ten compounds as sole terminal electron acceptor. Microbiol. Res., 155, 87–94. https://doi.org/10.1016/S0944-5013(00)80042-7.

Blakeney, M. D., Moulaei, T., & DiChristina, T. J., 2000b. Fe(III) reduction activity and cytochrome content of Shewanella putrefaciens grown on ten compounds as sole terminal electron acceptor. Microbiol. Res., 155, 87–94. https://doi.org/10.1016/S0944-5013(00)80042-7.

Borch, T., Kretzschmar, R., Skappler, A., Van Cappellen, P., Ginder-Vogel, M., Voegelin, A., & Campbell, K., 2010. Biogeochemical redox processes and their impact on contaminant dynamics. Environ. Sci. Technol., 44, 15–23. https://doi.org/10.1021/es9026248.

Borrok, D., Borrok, M. J., Fein, J. B., & Kiessling, L. L., 2005a. Link between chemotactic response to Ni^{2+} and its adsorption onto the *Escherichia Coli* cell surfaces. Environ. Sci. Technol., 39, 5227–5233. https://doi.org/10.1021/es0482381.

Borrok, D., Turner, B. F., & Fein, J. B., 2005b. A universal surface complexation framework for modeling proton binding onto bacterial surfaces in geologic settings. American Journal of Science, 305, 826–853. https://doi.org/10.2475/ajs.305.6-8.826.

Borrok, D. M., & Fein, J. B., 2005. The impact of ionic strength on the adsorption of protons, Pb, Cd, and Sr onto the surfaces of Gram negative bacteria: Testing non-electrostatic, diffuse, and triple-layer models. J. Colloid Interface Sci., 286, 110–126. https://doi.org/10.1016/j.jcis.2005.01.015.

Boteva, S., Radeva, G., Traykov, I., & Kenarova, A., 2016. Effects of long-term radionuclide and heavy metal contamination on the activity of microbial communities , inhabiting uranium mining impacted soils. Env. Sci Pollut Res, 23, 5644–5653. https://doi.org/10.1007/s11356-015-5788-5.

Brassard, P., Kramer, J. R., & Collins, P. V., 1990. Binding Site Analysis Using Linear Programming. Environ. Sci. Technol., 24, 195–201.

Bretti, C., Cigala, R. M., De Stefano, C., Lando, G., & Sammartano, S., 2014. Thermodynamics for proton binding of pyridine in different ionic media at different temperatures. J. Chem. Eng. Data, 59, 143–156. https://doi.org/10.1021/je4009602.

Brooks, S. C., Fredrickson, J. K., Carroll, S. L., Kennedy, D. W., Zachara, J. M., Plymale, A. E., Kelly, S. D., Kemner, K. M., & Fendorf, S., 2003. Inhibition of bacterial U(VI) reduction by calcium. Environ. Sci. Technol., 37, 1850–1858. https://doi.org/10.1021/es0210042.

Brown, W., & Zhao, J., 1995. Corrections: Adsorption of Sodium Dodecyl Sulfate on Polystyrene Latex Particles Using Dynamic Light Scattering and Zeta Potential Measurements (Macromolecules (1993) 26(11) (2711–2715) (10.1021/ma00063a012)). Macromolecules, 28, 2103. https://doi.org/10.1021/ma00110a054.

Burgos, W. D., Senko, J. M., Dempsey, B. A., Roden, E. E., Stone, J. J., Kemner, K. M., & Kelly, S. D., 2007. Soil humic acid decreases biological uranium(VI)

reduction by Shewanella putrefaciens CN32. Environ. Eng. Sci., 24, 755–761. https://doi.org/10.1089/ees.2006.0009.

Burman, E., & Bengtsson-Palme, J., 2021. Microbial Community Interactions Are Sensitive to Small Changes in Temperature. Front. Microbiol., 12, 1–8. https://doi.org/10.3389/fmicb.2021.672910.

Busalmen, J. P., & De Sánchez, S. R., 2001. Influence of pH and ionic strength on adhesion of a wild strain of Pseudomonas sp. to titanium. J. Ind. Microbiol. Biotechnol., 26, 303–308. https://doi.org/10.1038/sj.jim.7000133.

Butzen, M. L., & Fein, J. B., 2019. Influence of extracellular polymeric substances on the adsorption of cadmium onto three bacterial species. GEOMICROBIOLOGY JOURNAL, 36, 412–422. https://doi.org/10.1080/01490451.2018.1564804.

Caffrey, S. M., Park, H. S., Voordouw, J. K., He, Z., Zhou, J., & Voordouw, G., 2007. Function of periplasmic hydrogenases in the sulfate-reducing bacterium Desulfovibrio vulgaris hildenborough. J. Bacteriol., 189, 6159–6167. https://doi.org/10.1128/JB.00747-07.

Calabrese, S., Chakrawal, A., Manzoni, S., & Cappellen, P. V., 2021. Energetic scaling in microbial growth. PNAS, 118.

Chen, H., Zhu, T., Li, B., Fang, C., & Nie, M., 2020. The thermal response of soil microbial methanogenesis decreases in magnitude with changing temperature. Nat. Commun., 11, 1–7. https://doi.org/10.1038/s41467-020-19549-4.

Chen, L., Liu, J., Zhang, W., Zhou, J., Luo, D., & Li, Z., 2021. Uranium (U) source , speciation , uptake , toxicity and bioremediation strategies in soil-plant system : A review. J. Hazard. Mater., 413, 125319. https://doi.org/10.1016/j.jhazmat.2021.125319.

Christensen, J. J., Izatt, R. M., & Hansen, L. D., 1967. Thermodynamics of Proton Ionization in Dilute Aqueous Solution. VII. ΔH° and ΔS° Values for Proton Ionization from Carboxylic Acids at 25°. J. Am. Chem. Soc., 89, 213–222. https://doi.org/10.1021/ja00978a005.

Ciffroy, P., & Benedetti, M., 2018. A comprehensive probabilistic approach for integrating natural variability and parametric uncertainty in the prediction of trace metals speciation in surface waters. Environ. Pollut., 242, 1087–1097. https://doi.org/10.1016/j.envpol.2018.07.064.

Clifton, L. A., Skoda, M. W., Le Brun, A. P., Ciesielski, F., Kuzmenko, I., Holt, S. A., & Lakey, J. H., 2015. Effect of divalent cation removal on the structure of gram-negative bacterial outer membrane models. Langmuir, 31, 404–412. https://doi.org/10.1021/la504407v.

Cook, M. C., Blank, J. G., Suzuki, S., Nealson, K. H., & Morrill, P. L., 2021. Assessing Geochemical Bioenergetics and Microbial Metabolisms at Three Terrestrial Sites of Serpentinization: The Tablelands (NL, CAN), The Cedars (CA, USA), and Aqua de Ney (CA, USA). J. Geophys. Res. Biogeosciences, 126, 1–16. https://doi.org/10.1029/2019JG005542.

Cossio Salas, E., Berelson, W. M., Hammond, D. E., Kampf, R., Nealson, K. H., Cossio, E., Berelson, W. M., Hammond, D. E., Kampf, A. R., Nealson, K. H., Influence, T., Salas, E. C., Berelson, W. M., Hammond, D. E., Kampf, A. R., & Nealson, K. H., 2009. The Influence of Carbon Source on the Products of Dissimilatory Iron Reduction The Influence of Carbon Source on the Products of Dissimilatory Iron Reduction, . 0451. https://doi.org/10.1080/01490450903060806.

Costa, K. C., Yoon, S. H., Pan, M., Burn, J. A., Baliga, N. S., & Leigh, J. A., 2013. Effects of H2 and formate on growth yield and regulation of methanogenesis in Methanococcus maripaludis. J. Bacteriol., 195, 1456–1462. https://doi.org/10.1128/JB.02141-12.

Coutelot, F. M., Seaman, J. C., & Baker, M., 2018. Uranium(VI) adsorption and surface complexation modeling onto vadose sediments from the Savannah River Site. Environ. Earth Sci., 77. https://doi.org/10.1007/s12665-018-7316-7.

Cox, J. S., Smith, D. S., Warren, L. A., & Ferris, F. G., 1999. Characterizing heterogeneous bacterial surface functional groups using discrete affinity spectra for proton binding. Environ. Sci. Technol., 33, 4514–4521. https://doi.org/10.1021/es990627l.

Dale, J. R., & Dichristina, T. J., 2006. Respiration-linked uranium reduction by Shewanella putrefaciens Strain 200. Abstr. Pap. Am. Chem. Soc., 120-GEOC.

Daniel, R. M., 1996. The upper limits of enzyme thermal stability. Enzyme Microb. Technol., 19, 74–79. https://doi.org/10.1016/0141-0229(95)00174-3.

Danil De Namor, A. F., & Pacheco Tanaka, D. A., 1998. Thermodynamics of protonation and complexation of EDTA derivatives and metal cations in water. J. Chem. Soc. - Faraday Trans., 94, 3105–3110. https://doi.org/10.1039/a805435e.

Danson, M. J., Hough, D. T., Russell, R. J., Taylor, G. L., & Pearl, L., 1996. Enzyme thermostability and thermoactivity. Protein Eng., 9, 629–630. https://doi.org/10.1093/protein/9.8.629.

Das, D., 2021. Measuring Metabolism and Bioenergetic Profiles of Biofilm: Isothermal Calorimetry, Differential Scanning Calorimetry, and Future of Chip Calorimetry. In M. Nag, & D. Lahiri (Eds.), *Anal. Methodol. Biofilm Res.*.

Daughney, C. J., & Fein, J. B., 1998. The effect of ionic strength on the adsorption of H+, Cd2+, Pb2+ and Cu2+ by Bacillus subtilis and Bacillus licheniformis: A surface complexation model. J. Colloid Interface Sci., 198, 53–77. https://doi.org/10.1006/jcis.1997.5266.

De Robertis, A., De Stefano, C., & Gianguzza, A., 1991. Salt effects on the protonation of l-histidine and l-aspartic acid: a complex formation model. Thermochim. Acta, 177, 39–57. https://doi.org/10.1016/0040-6031(91)80083-U.

De Stefano, C., Giuffrè, O., & Sammartano, S., 2005. Protonation constants of ethylenediamine, diethylenetriamine, and spermine in NaCl(aq), NaI(aq), (CH3)4NCl(aq), and (C 2H5)4NI(aq) at different ionic strengths and t = 25 °C. J. Chem. Eng. Data, 50, 1917–1923. https://doi.org/10.1021/je050177e.

De Stefano, C., Milea, D., & Sammartano, S., 2004. Speciation of phytate ion in aqueous solution: Thermodynamic parameters for protonation in NaCl. Thermochim. Acta, 423, 63–69. https://doi.org/10.1016/j.tca.2004.04.017.

DeRobertis, A., DeStefano, C., & Foti, C., 1999. Medium effects on the protonation of carboxylic acids at different temperatures. J. Chem. Eng. Data, 44, 262–270. https://doi.org/10.1021/je980239j.

DiChristina, T. J., & DeLong, E. F., 1993. Design and application of rRNA-targeted oligonucleotide probes for the dissimilatory iron- and manganese-reducing bacterium Shewanella putrefaciens. Appl. Environ. Microbiol., 59, 4152–60.

Dong, W., & Brooks, S. C., 2006. Determination of the formation constants of ternary complexes of uranyl and carbonate with alkaline earth metals (Mg2+, Ca2+, Sr 2+, and Ba2+) using anion exchange method. Environ. Sci. Technol., 40, 4689–4695. https://doi.org/10.1021/es0606327.

Dong, W., & Brooks, S. C., 2008. Formation of aqueous MgUO2(CO3)32- complex and uranium anion exchange mechanism onto an exchange resin. Environ. Sci. Technol., 42, 1979–1983. https://doi.org/10.1021/es0711563.

Dube, A., Zbytniewski, R., Kowalkowski, T., Cukrowska, E., & Buszewski, B., 2001. Adsorption and Migration of Heavy Metals in Soil. Polish J. Environ. Stud., 10, 1–10.

Dubey, A. N., Relan, G. R., & Vaidyanathan, S., 1999. Simultaneous determination of uranium and plutonium at trace levels in process streams using Arsenazo III by derivative spectrophotometry. J. Radioanal. Nucl. Chem., 240, 741–746. https://doi.org/10.1007/BF02349847.

Dzombak, D. A., & Morel, F. M. M., 1990. *Surface Complexation Modeling: Hydrous Ferric Oxide*. New York: Wiley-Interscience.

Eaton, J. W., Bateman, D., Hauberg, S., & Wehbring, R., 2021. *GNU Octave version 6.4.0 manual: a high-level interactive language for numerical computations*. manual.

Edward J. King, 1965. *Acid-base equilibria*. New York: MacMillan.

Eilers, P. H., 2004. Parametric Time Warping. Anal. Chem., 76, 404–411. https://doi.org/10.1021/ac034800e.

Fein, J. B., 2006. Thermodynamic modeling of metal adsorption onto bacterial cell walls: Current challenges. In D. Sparks (Ed.), *Adv. Agron.* (pp. 179–202). San Diego: Elsevier Academic Press Inc. https://doi.org/10.1016/S0065-2113(06)90005-4.

Fein, J. B., Boily, J.-F., Yee, N., Gorman-Lewis, D., & Turner, B. F., 2005. Potentiometric titrations of Bacillus subtilis cells to low pH and a comparison of modeling approaches. Geochim. Cosmochim. Acta, . https://doi.org/10.1016/j.gca.2004.07.033.

Fein, J. B., Daughney, C. J., Yee, N., & Davis, T. A., 1997. A chemical equilibrium model for metal adsorption onto bacterial surfaces. Geochim. Cosmochim. Acta, 61, 3319–3328. https://doi.org/10.1016/S0016-7037(97)00166-X.

Feng, J., Wang, T., Zhang, S., Shi, W., & Zhang, Y., 2014. An optimized SYBR green I/PI assay for rapid viability assessment and antibiotic susceptibility testing for Borrelia burgdorferi. PLoS One, 9. https://doi.org/10.1371/journal.pone.0111809.

Flynn, S., Szymanowski, J., & Fein, J., 2014. Modeling bacterial metal toxicity using a surface complexation approach. Chemical Geology, 374–375, 110–116. https://doi.org/10.1016/j.chemgeo.2014.03.010.

Flynn, T. M., Flynn, T. M., Sanford, R. A., Ryu, H., Bethke, C. M., & Levine, A. D., 2013. Functional microbial diversity explains groundwater chemistry in a pristine aquifer Functional microbial diversity explains groundwater chemistry in a pristine aquifer. BMC Microbiol., 13, 1.

Fowle, D. A., Fein, J. B., & Aaron, M., 2000. Experimental study of uranyl adsorption onto Bacillus subtilis. Environ. Sci. Technol., 34, 3737–3741. https://doi.org/10.1021/es991356h.

Frank, H. S., & Evans, M. W., 1945. Free volume and entropy in condensed systems III. Entropy in binary liquid mixtures; Partial molal entropy in dilute solutions; Structure and thermodynamics in aqueous electrolytes. J. Chem. Phys., 13, 507–532. https://doi.org/10.1063/1.1723985.

Fuchs, A., Lyautey, E., Montuelle, B., & Casper, P., 2016. Effects of increasing temperatures on methane concentrations and methanogenesis during experimental incubation of sediments from oligotrophic and mesotrophic lakes. J. Geophys. Res. Biogeosciences, 121, 1394–1406. https://doi.org/10.1002/2016JG003328.

Furukawa, Y., & Dale, J. R., 2013. The surface properties of Shewanella putrefaciens 200 and S. oneidensis MR-1: The effect of pH and terminal electron acceptors. Geochem. Trans., 14. https://doi.org/10.1186/1467-4866-14-3.

Gans, P., & O'Sullivan, B., 2000. GLEE, a new computer program for glass electrode calibration. Talanta, 51, 33–37. https://doi.org/10.1016/S0039-9140(99)00245-3.

Gavin, H. P., 2019. *The Levenberg-Marquardt algorithm for nonlinear least squares curve-fitting problems*. manual.

Gavrilov, S. N., Stracke, C., Jensen, K., Menzel, P., Kallnik, V., Slesarev, A., Sokolova, T., Zayulina, K., Bräsen, C., Bonch-Osmolovskaya, E. A., Peng, X., Kublanov, I. V., & Siebers, B., 2016. Isolation and characterization of the first xylanolytic hyperthermophilic euryarchaeon Thermococcus sp. strain 2319x1 and its unusual multidomain glycosidase. Front. Microbiol., 7, 1–17. https://doi.org/10.3389/fmicb.2016.00552.

Ginn, B., & Fein, J. B., 2009. Temperature dependence of Cd and Pb binding onto bacterial cells. Chem. Geol., 259, 99–106. https://doi.org/10.1016/j.chemgeo.2008.09.021.

Goldberg, R., & Wadsö, I., 2001. Standards in isothermal microcalorimetry (IUPAC Technical Report). Pure Appl. Chem., 73, 1625–1639. https://doi.org/10.1351/pac200173101625.

Goldberg, R. N., Kishore, N., & Lennen, R. M., 2002. Thermodynamic quantities for the ionization reactions of buffers. J. Phys. Chem. Ref. Data, 31, 231–370. https://doi.org/10.1063/1.1416902.

Goldberg, S., & Johnston, C. T., 2001. Mechanisms of arsenic adsorption on amorphous oxides evaluated using macroscopic measurements, vibrational spectroscopy, and surface complexation modeling. J. Colloid Interface Sci., 234, 204–216. https://doi.org/10.1006/jcis.2000.7295.

González-Cabaleiro, R., Curtis, T. P., & Ofiţeru, I. D., 2019. Bioenergetics analysis of ammonia-oxidizing bacteria and the estimation of their maximum growth yield. Water Res., 154, 238–245. https://doi.org/10.1016/j.watres.2019.01.054.

Gorman-Lewis, D., 2009. Calorimetric measurements of proton adsorption onto Pseudomonas putida. J. Colloid Interface Sci., 337, 390–395. https://doi.org/10.1016/j.jcis.2009.05.066.

Gorman-Lewis, D., 2011. Enthalpies of proton adsorption onto Bacillus licheniformis at 25, 37, 50, and 75°C. Geochim. Cosmochim. Acta, 75, 1297–1307. https://doi.org/10.1016/j.gca.2010.12.009.

Gorman-Lewis, D., 2014. Enthalpies and Entropies of Cd and Zn Adsorption onto Bacillus licheniformis and Enthalpies and Entropies of Zn Adsorption onto Bacillus subtilis from Isothermal Titration Calorimetry and Surface Complexation Modeling. Geomicrobiol. J., 31, 383–395. https://doi.org/10.1080/01490451.2013.835887.

Gorman-Lewis, D., Elias, P. E., & Fein, J. B., 2005a. Adsorption of aqueous uranyl complexes onto Bacillus subtilis cells. Environ. Sci. Technol., 39, 4906–4912. https://doi.org/10.1021/es047957c.

Gorman-Lewis, D., Fein, J. B., Soderholm, L., Jensen, M. P., & Chiang, M. H., 2005b. Experimental study of neptunyl adsorption onto Bacillus subtilis. Geochim. Cosmochim. Acta, 69, 4837–4844. https://doi.org/10.1016/j.gca.2005.06.028.

Gorman-Lewis, D., Jensen, M. P., Harrold, Z. R., & Hertel, M. R., 2013. Complexation of neptunium(V) with Bacillus subtilis endospore surfaces and their exudates. Chem. Geol., 341, 75–83. https://doi.org/10.1016/j.chemgeo.2013.01.004.

Gorman-Lewis, D., Martens-Habbena, W., & Stahl, D. A., 2014. Thermodynamic characterization of proton-ionizable functional groups on the cell surfaces of ammonia-oxidizing bacteria and archaea. Geobiology, 12, 157–171. https://doi.org/10.1111/gbi.12075.

Gorman-Lewis, D., Martens-Habbena, W., & Stahl, D. A., 2019. Cu(II) adsorption onto

ammonia-oxidizing bacteria and archaea. Geochimica et Cosmochimica Acta, 255, 127–143. https://doi.org/10.1016/j.gca.2019.04.011.

Grenthe, I., Ots, H., & Ginstrup, O., 1970. A calorimetric determination of the enthalpy of ionization of water and the enthalpy of protonation of THAM at 5, 20, 25, 35, and 50C. Acta Chem. Scand., 24, 1067–1080.

Grube, M., Muter, O., Strikauska, S., Gavare, M., & Limane, B., 2008. Application of FT-IR spectroscopy for control of the medium composition during the biodegradation of nitro aromatic compounds. J. Ind. Microbiol. Biotechnol., 35, 1545–1549. https://doi.org/10.1007/s10295-008-0456-0.

Guillaumont, R., Fanghanel, T., Fuger, J., Grenthe, I., Neck, V., Palmer, D. a., & Rand, M. H., 2003. *Update on the Chemical Thermodynamics of Uranium, Neptunium, Plutonium, Americium and Technetium*.

Haas, J. R., Dichristina, T. J., & Wade, R., 2001. Thermodynamics of U(VI) sorption onto Shewanella putrefaciens. Chem. Geol., 180, 33–54. https://doi.org/10.1016/S0009-2541(01)00304-7.

Hao, W., Flynn, S. L., Kashiwabara, T., Alam, M. S., Bandara, S., Swaren, L., Robbins, L. J., Alessi, D. S., & Konhauser, K. O., 2019. The impact of ionic strength on the proton reactivity of clay minerals. Chem. Geol., 529, 119294. https://doi.org/10.1016/j.chemgeo.2019.119294.

Harrold, Z. R., & Gorman-Lewis, D., 2013. Thermodynamic analysis of Bacillus subtilis endospore protonation using isothermal titration calorimetry. Geochim. Cosmochim. Acta, 109, 296–305. https://doi.org/10.1016/j.gca.2013.01.002.

Hart, C., & Gorman-Lewis, D., 2021. Energetics of Acidianus ambivalens

growth in response to oxygen availability. Geobiology, 19, 48–62. https://doi.org/10.1111/gbi.12413.

Hau, H. H., & Gralnick, J. A., 2007. Ecology and biotechnology of the genus Shewanella. Annu. Rev. Microbiol., 61, 237–258. https://doi.org/10.1146/annurev.micro.61.080706.093257.

He, Z., Yang, Y., Zhou, S., Zhong, H., & Sun, W., 2013. The effect of culture condition and ionic strength on proton adsorption at the surface of the extreme thermophile Acidianus manzaensis. Colloids Surfaces B Biointerfaces, 102, 667–673. https://doi.org/10.1016/j.colsurfb.2012.09.028.

Heijnen, J., & van Dijken, J., 1992. In search of a thermodynamic description of biomass yields for the chemotrophic growth of micro- organisms. Biotechnol. Bioeng., 39, 833–858.

Heijnen, J. J., & Kleerebezem, R., 2010. Bioenergetics of Microbial Growth. Encycl. Ind. Biotechnol., (pp. 1–66).

Helgeson, H., Kirkham, D., & Flowers, G., 1981. Theoretical pre- diction of the thermodynamic behavior of aqueous electrolytes at Theoretical pre- diction of the thermodynamic behavior of aqueous electrolytes at high pressures and temperatures: IV. Calculation of activity coeffi- cients, osmotic coeffi. Am. J. Sci., 281, 1249–1516. https://doi.org/10.2475/ajs.281.10.1249.

Helgeson, H. C., Delany, J. M., Nesbitt, H. W., & Bird, D. K., 1978. Summary and Critique of the Thermodynamic Properties of Rock-forming Minerals. Am. J. Sci., 278, 1–229.

Hoehler, T. M., 2004. Biological energy requirements as quantitative boundary conditions for life in the subsurface. Geobiology, 2, 205–215. https://doi.org/10.1111/j.1472-4677.2004.00033.x.

Ibrahim, M., Alaam, M., El-Haes, H., Jalbout, A. F., & De Leon, A., 2006. Analysis of the structure and vibrational spectra of glucose and fructose. Eclet. Quim., 31, 15–21. https://doi.org/10.1590/S0100-46702006000300002.

Irudayam, S. J., & Henchman, R. H., 2009. Entropic cost of protein-ligand binding and its dependence on the entropy in solution. J. Phys. Chem. B, 113, 5871–5884. https://doi.org/10.1021/jp809968p.

Javanbakht, V., Alavi, S. A., & Zilouei, H., 2014. Mechanisms of heavy metal removal using microorganisms as biosorbent. Water Sci. Technol., 69, 1775–1787. https://doi.org/10.2166/wst.2013.718.

Ji, Y., Yang, X., Ji, Z., Zhu, L., Ma, N., Chen, D., Jia, X., Tang, J., & Cao, Y., 2020. DFT-Calculated IR Spectrum Amide I, II, and III Band Contributions of N-Methylacetamide Fine Components. ACS Omega, 5, 8572–8578. https://doi.org/10.1021/acsomega.9b04421.

Jiang, W., Saxena, A., Song, B., B. Ward, B., J. Beveridge, T., & C. B. Myneni, S., 2004. Elucidation of Functional Groups on Gram-Positive and Gram-Negative Bacterial Surfaces Using Infrared Spectroscopy. Langmuir, 20, 11433–11442. https://doi.org/10.1021/la049043+.

Johansson, P., & Wadsö, I., 1999. An isothermal microcalorimetric titration/perfusion vessel equipped with electrodes and spectrophotometer. Thermochim. Acta, 342, 19–29. https://doi.org/10.1016/s0040-6031(99)00299-3.

Johnson, J. W., Oelkers, E. H., & Helgeson, H. C., 1992. SUPCRT92: A software package for calculating the standard molal thermodynamic properties of minerals, gases, aqueous species, and reactions from 1 to 5000 bar and 0 to 1000°C. Comput. Geosci., 18, 899–947.

Jr, R. W., & Dichristina, T. J., 2000. Isolation of U (VI) reduction-de ¢ cient mutants of Shewanella putrefaciens. FEMS Microbiol. Lett., 184, 143–148.

K. Auer, G., & B. Weibel, D., 2017. Bacterial Cell Mechanics. Biochemistry, 56, 3710–3724. https://doi.org/10.1021/acs.biochem.7b00346.

Kahm, M., Hasenbrink, G., Lichtenberg-Fraté, H., Ludwig, J., & Kschischo, M., 2010. Grofit: Fitting biological growth curves with R. J. Stat. Softw., 33, 1–21. https://doi.org/10.18637/jss.v033.i07.

Kalintsev, A., Migdisov, A., Alcorn, C., Baker, J., Brugger, J., Mayanovic, R. A., Akram, N., Guo, X., Xu, H., Boukhalfa, H., Caporuscio, F. A., Viswanathan, H., Jove-Colon, C., Wang, Y., Matteo, E., & Roback, R., 2021. Uranium carbonate complexes demonstrate drastic decrease in stability at elevated temperatures. Commun. Chem., 4, 1–8. https://doi.org/10.1038/s42004-021-00558-3.

Kamnev, A. A., Antonyuk, L. P., Matora, L. Y., Serebrennikova, O. B., Sumaroka, M. V., Colina, M., Renou-Gonnord, M. F., & Ignatov, V. V., 1999. Spectroscopic characterization of cell membranes and their constituents of the plant-associated soil bacterium Azospirillum brasilense. J. Mol. Struct., 480-481, 387–393. https://doi.org/10.1016/S0022-2860(98)00712-1.

Kempes, C. P., van Bodegom, P. M., Wolpert, D., Libby, E., Amend, J., & Hoehler, T., 2017. Drivers of bacterial maintenance and minimal energy requirements. Front. Microbiol., 8, 1–10. https://doi.org/10.3389/fmicb.2017.00031.

Kenney, J. P., Ellis, T., Nicol, F. S., Porter, A. E., & Weiss, D. J., 2018. The effect of bacterial growth phase and culture concentration on U(VI) removal from aqueous solution. Chem. Geol., 482, 61–71. https://doi.org/10.1016/j.chemgeo.2018.01.025.

Kenney, J. P., Kirby, M. E., Cuadros, J., & Weiss, D. J., 2017a. A conceptual model to predict uranium removal from aqueous solutions in water-rock systems associated with low- and intermediate-level radioactive waste disposal. RSC Adv., 7, 7876–7884. https://doi.org/10.1039/c6ra26773d.

Kenney, J. P., Kirby, M. E., Cuadros, J., & Weiss, D. J., 2017b. A conceptual model to predict uranium removal from aqueous solutions in water-rock systems associated with low- and intermediate-level radioactive waste disposal. RSC Adv., 7, 7876–7884. https://doi.org/10.1039/c6ra26773d.

Kitano, H., Onishi, Y., Kirishima, A., Sato, N., & Tochiyama, O., 2006. Determination of the thermodynamic quantities of complexation between Eu(III) and carboxylic acids by microcalorimetry. Radiochim. Acta, 94, 541–547.

Koebnik, R., Locher, K. P., & Van Gelder, P., 2000. Structure and function of bacterial outer membrane proteins: Barrels in a nutshell. Mol. Microbiol., 37, 239–253. https://doi.org/10.1046/j.1365-2958.2000.01983.x.

Konn, C., Charlou, J. L., Holm, N. G., & Mousis, O., 2015. The production of methane, hydrogen, and organic compounds in ultramafic-hosted hydrothermal vents of the mid-atlantic ridge. Astrobiology, 15, 381–399. https://doi.org/10.1089/ast.2014.1198.

Kostka, E., Iii, G. W. L., Nealson, K. H., & April, R., 1995. Chemical and biological reduction of Mn (III) -pyrophosphate complexes : Potential importance of dissolved Mn (III) as an environmental oxidant, . (pp. 885–894).

Krasikova, I. N., Kapustina, N. V., Isakov, V. V., Dmitrenok, A. S., Dmitrenok, P. S., Gorshkova, N. M., & Solov'eva, T. F., 2004. Detailed structure of lipid A isolated from lipopolysaccharide from the marine proteobacterium Marinomonas vaga ATCC 27119T. Eur. J. Biochem., 271, 2895–2904. https://doi.org/10.1111/j.1432-1033.2004.04212.x.

Ktodzinska, E., Szumski, M., Dzuibakiewixz, E., Hrynkiewicz, K., Skwarek, E., Janusz, W., & Buszewski, B., 2010. Effect of zeta potential value on bacterial behavior during electrophoretic separation. Electrophoresis, 31, 1590–1596. https://doi.org/10.1002/elps.200900559.

Kukkadapu, R., Zachara, J., Fredrickson, J., Kennedy, D., Dohnalkova, A., & McCready, D., 2005. Ferrous hydroxy carbonate is a stable transformation product of biogenic magnetite R AVI K . K UKKADAPU ,* J OHN M . Z ACHARA , J AMES K . F REDRICKSON , D AVID W . K ENNEDY ,. Am. Mineral., 90, 510–515. https://doi.org/10.2138/am.2005.1727.

Lane, N., 2014. Bioenergetic constraints on the evolution of complex life. Cold Spring Harb. Perspect. Biol., 6, 1–18. https://doi.org/10.1101/cshperspect.a015982.

Langmuir, D., 1997. *Aqueous Environmental Geochemistry*. Prentice Hall.

LaRowe, D. E., & Amend, J. P., 2015. Power limits for microbial life. Front. Microbiol., 6, 1–11. https://doi.org/10.3389/fmicb.2015.00718.

Liu, C., Gorby, Y. A., Zachara, J. M., Fredrickson, J. K., & Brown, C. F., 2002. Reduction kinetics of Fe(III), Co(III), U(VI), Cr(VI), and Tc(VII) in cultures of dissimilatory metal-reducing bacteria. Biotechnol. Bioeng., 80, 637–49. https://doi.org/10.1002/bit.10430.

Liu, C., Zachara, J. M., Gorby, Y. A., Szecsody, J. E., & Brown, C. F., 2001a. Microbial reduction of Fe(III) and sorption/precipitation of Fe(II) on Shewanella putrefaciens strain CN32. Environ. Sci. Technol., 35, 1385–1393. https://doi.org/10.1021/es0015139.

Liu, J., Yu, Q., Showalter, A. R., Bunker, B. A., Swanson, J. S., Reed, D., Rong, X., & Fein, J. B., 2020. Cadmium and proton adsorption onto a halophilic archaeal species: The role of cell envelope sulfhydryl sites. GEOCHIMICA ET COSMOCHIMICA ACTA, 276, 186–197. https://doi.org/10.1016/j.gca.2020.02.038.

Liu, J. S., Marison, I. W., & von Stockar, U., 2001b. Microbial growth by a net heat up-take: A calorimetric and thermodynamic study on acetotrophic methanogenesis by Methanosarcina barkeri. Biotechnol. Bioeng., 75, 170–180. https://doi.org/10.1002/bit.1176.

Lopez-fernandez, M., Jroundi, F., & Ruiz-fresneda, M. A., 2020. Minireview Microbial interaction with and tolerance of radionuclides : underlying mechanisms and biotechnological applications. Microb. Biotechnol., 14, 810–828. https://doi.org/10.1111/1751-7915.13718.

Lopez-Fernandez, M., Romero-González, M., Günther, A., Solari, P. L., & Merroun, M. L., 2018. Effect of U(VI) aqueous speciation on the binding of uranium by the cell surface of Rhodotorula mucilaginosa, a natural yeast isolate from bentonites. Chemosphere, 199, 351–360. https://doi.org/10.1016/j.chemosphere.2018.02.055.

Lovley, D., 1993. Dissimilatory metal reduction. Annu. Rev. Microbiol., 47, 263–290. https://doi.org/10.1108/07378830410524567.

Lovley, D. R., & Phillips, E. J., 1992. Bioremediation of Uranium Contamination with Enzymatic Uranium Reduction. Environ. Sci. Technol., 26, 2228–2234. https://doi.org/10.1021/es00035a023.

Lovley, D. R., Phillips, E. J., Gorby, Y. A., & Landa, E. R., 1991. Microbial reduction of uranium. Nature, 350, 413–416. https://doi.org/10.1038/350413a0.

Lunau, M., Lemke, A., Walther, K., Martens-Habbena, W., & Simon, M., 2005. An improved method for counting bacteria from sediments and turbid environments by epifluorescence microscopy. Environ. Microbiol., 7, 961–968. https://doi.org/10.1111/j.1462-2920.2005.00767.x.

Lundstedt, E., Kahne, D., & Ruiz, N., 2021. Assembly and Maintenance of Lipids at the Bacterial Outer Membrane. Chem. Rev., 121, 5098–5123. https://doi.org/10.1021/acs.chemrev.0c00587.

Maamar, S. B., Aquilina, L., Quaiser, A., Pauwels, H., Michon-Coudouel, S., Vergnaud-Ayraud, V., Labasque, T., Roques, C., Abbott, B. W., & Dufresne, A., 2015. Groundwater isolation governs chemistry and microbial community structure along hydrologic flowpaths. Front. Microbiol., 6, 1–13. https://doi.org/10.3389/fmicb.2015.01457.

Maeder, M., & Neuhold, Y.-M., 2007. *Practical data analysis in chemistry, volume 26*. San Diego, CA, USA: Elsevier Science.

Mansuy, N., 2018. *Groundwater Microbiology*. https://doi.org/10.1201/9780203734063-3.

Marshall, K. C., Stout, R., & Mitchell, R., 1971. Mechanism of the Initial Events in the Sorption of Marine Bacteria to Surfaces. J. Gen. Microbiol., 68, 337–348. https://doi.org/10.1099/00221287-68-3-337.

Marshall, M. J., Beliaev, A. S., Dohnalkova, A. C., Kennedy, D. W., Shi, L., Wang, Z., Boyanov, M. I., Lai, B., Kemner, K. M., McLean, J. S., Reed, S. B., Culley, D. E., Bailey, V. L., Simonson, C. J., Saffarini, D. A., Romine, M. F., Zachara, J. M., & Fredrickson, J. K., 2006. c-type cytochrome-dependent formation of U(IV) nanoparticles by Shewanella oneidensis. PLoS Biol., 4, 1324–1333. https://doi.org/10.1371/journal.pbio.0040268.

Martin, W., Baross, J., Kelley, D., & Russell, M. J., 2008. Hydrothermal vents and the origin of life. Nat. Rev. Microbiol., 6, 805–814. https://doi.org/10.1038/nrmicro1991.

Martin, W. F., 2020. Older Than Genes: The Acetyl CoA Pathway and Origins. Front. Microbiol., 11, 1–21. https://doi.org/10.3389/fmicb.2020.00817.

Martin, W. F., & Sousa, F. L., 2016. Early microbial evolution: The age of anaerobes. Cold Spring Harb. Perspect. Biol., 8. https://doi.org/10.1101/cshperspect.a018127.

Martinez, R. E., Smith, D. S., Kulczycki, E., & Ferris, F. G., 2002. Determination of intrinsic bacterial surface acidity constants using a Donnan shell model and a continuous pK a distribution method. J. Colloid Interface Sci., 253, 130–139. https://doi.org/10.1006/jcis.2002.8541.

Mehta, M. P., & Baross, J. A., 2006. Nitrogen fixation at 92C by a hydrothermal vent archaeon. Science (80-.)., 314, 1783–1786. https://doi.org/10.1126/science.1134772.

Mei, H., Liu, Y., Tan, X., Feng, J., Ai, Y., & Fang, M., 2020. U(VI) adsorption on hematite nanocrystals: Insights into the reactivity of {001} and {012} facets. J. Hazard. Mater., 399, 123028. https://doi.org/10.1016/j.jhazmat.2020.123028.

de Mendoza, D., & Cronan, J. E., 1983. Thermal regulation of membrane lipid fluidity in bacteria. Trends Biochem. Sci., 8, 49–52. https://doi.org/10.1016/0968-0004(83)90388-2.

Merino, N., Aronson, H. S., Bojanova, D. P., Feyhl-Buska, J., Wong, M. L., Zhang, S., & Giovannelli, D., 2019. Living at the extremes: Extremophiles and the limits of life in a planetary context. Front. Microbiol., 10. https://doi.org/10.3389/fmicb.2019.00780.

Moon, E. M., & Peacock, C. L., 2012. Adsorption of Cu(II) to ferrihydrite and ferrihydrite-bacteria composites: Importance of the carboxyl group for Cu mobility in natural environments. Geochim. Cosmochim. Acta, 92, 203–219. https://doi.org/10.1016/j.gca.2012.06.012.

Morgan, R. M., Pihl, T. D., Nölling, J., & Reeve, J. N., 1997. Hydrogen regulation of growth, growth yields, and methane gene transcription in Methanobacterium thermoautotrophicum δH. J. Bacteriol., 179, 889–898. https://doi.org/10.1128/jb.179.3.889-898.1997.

Myers, C. R., & Myers, J. M., 1993. Ferric reductase is associated with the membranes of anaerobically grown Shewanella putrefaciens MR-1. FEMS Microbiol. Lett., 108, 15–22. https://doi.org/10.1111/j.1574-6968.1993.tb06066.x.

Myers, C. R., & Nealson, K. H., 1988. Bacterial Manganese Reduction and Growth with Manganese Oxide as the Sole Electron Acceptor Published by : American Association for the Advancement of Science Stable URL : http://www.jstor.org/stable/1701057 REFERENCES Linked references are available on J. Science (80-.)., 240, 1319–1321.

Myers, C. R., & Nealson, K. H., 1990. Respiration-linked proton translocation couples to anaerobic reduction of manganese(IV) and iron(III) in Shewanella putrefaciens MR-1. J. Bacteriol., 172, 6232–6238. https://doi.org/10.1128/jb.172.11.6232-6238.1990.

Nash, K. L., Rao, L. F., & Choppin, G. R., 1995. Calorimetric and laser induced fluorescence investigation of the complexation geometry of selected europium-gem-diphosphonate complexes in acidic solutions. Inorg. Chem., 34, 2753–2758. https://doi.org/10.1021/ic00114a038.

Nazarenko, E. L., Komandrova, N. A., Gorshkova, R. P., Tomshich, S. V., Zubkov, V. A., Kilcoyne, M., & Savage, A. V., 2003. Structures of polysaccharides and oligosaccharides of some Gram-negative marine Proteobacteria. Carbohydr. Res., 338, 2449–2457. https://doi.org/10.1016/j.carres.2003.06.004.

Nealson, K. H., & Moser, D. P., 1996. Growth of the facultative anaerobe Shewanella putrefaciens by elemental sulfur reduction . These include : Growth of the Facultative Anaerobe Shewanella putrefaciens by Elemental Sulfur Reduction. Appl. Environ. Microbiol., 62, 2100.

Nell, R. M., & Fein, J. B., 2017. Influence of sulfhydryl sites on metal binding by bacteria. Geochim. Cosmochim. Acta, 199, 210–221. https://doi.org/10.1016/j.gca.2016.11.039.

Newsome, L., Morris, K., Lloyd, J. R., & Doe, U. S., 2014. The biogeochemistry and bioremediation of uranium and other priority radionuclides. Chem. Geol., 363, 164–184. https://doi.org/10.1016/j.chemgeo.2013.10.034.

Ngwenya, N., & Chirwa, E. M. N., 2015. Characterisation of surface uptake and biosorption of cationic nuclear fission products by sulphate-reducing bacteria. Water SA, 41, 314–324. https://doi.org/10.4314/wsa.v41i3.03.

Nichols, D. S., Olley, J., Garda, H., & Brenner, R. R., 2000. Effect of Temperature and Salinity Stress on Growth and Lipid Composition of Shewanella gelidimarina. Microb. Ecol., 66, 2422–2429.

Noda, & Kanemasa, 1984. Determination of surface charge of some bacteria by colloid titration. Physiol Chem Phys Med NMR, 4, 263–274.

O'Loughlin, E. J., Gorski, C. A., Flynn, T. M., & Scherer, M. M., 2019. Electron donor utilization andsecondary mineral formation during the bioreduction of lepidocrocite by shewanella putrefaciens CN32. Minerals, 9. https://doi.org/10.3390/min9070434.

Panias, D., & Krestou, A., 2015. Uranium (VI) speciation diagrams in the UO22 + / CO32- / H2O system at 25 ° C. Eur. J. Miner. Process. Enviromental Prot., 4, 113–129.

Paquete, C. M., Nitschke, W., Daldal, F., & Zannoni, D., 2021. Editorial: Microbial Bioenergetics. Front. Microbiol., 12, 10–12. https://doi.org/10.3389/fmicb.2021.793917.

Parikh, S. J., & Chorover, J., 2006. ATR-FTIR spectroscopy reveals bond formation during bacterial adhesion to iron oxide. Langmuir, 22, 8492–8500. https://doi.org/10.1021/la061359p.

Parker, S. F., 2013. Assignment of the vibrational spectrum of l-cysteine. Chem. Phys., 424, 75–79. https://doi.org/10.1016/j.chemphys.2013.04.020.

Parkhurst, D. L., & Appelo, C., 1999. User's guide to PHREEQC (ver 2) - A computer program for speciation, batch-reaction, one-dimensional transport, and inverse geochemical calculations. URL: `http://www.xs4all.nl/{~}appt/index.html`.

Paulo, C., Kenney, J. P., Persson, P., & Dittrich, M., 2018. Effects of phosphorus in growth media on biomineralization and cell surface properties of marine cyanobacteria synechococcus. Geosci., 8. https://doi.org/10.3390/geosciences8120471.

Peak, D., Ford, R. G., & Sparks, D. L., 1999. An in situ ATR-FTIR investigation of sulfate bonding mechanisms on goethite. J. Colloid Interface Sci., 218, 289–299. https://doi.org/10.1006/jcis.1999.6405.

Peitzsch, M., Harms, H., & Maskow, T., 2008. Real time analysis of Escherichia coli biofilms using calorimetry. Chem. Eng. Process., 47, 1000–1006. https://doi.org/10.1016/j.cep.2007.02.029.

Peters, J. W., Schut, G. J., Boyd, E. S., Mulder, D. W., Shepard, E. M., Broderick, J. B., King, P. W., & Adams, M. W., 2015. [FeFe]- and [NiFe]-hydrogenase diversity, mechanism, and maturation. Biochim. Biophys. Acta - Mol. Cell Res., 1853, 1350–1369. https://doi.org/10.1016/j.bbamcr.2014.11.021.

Philips, J., Driessche, N. V. D., Paepe, K. D., Prévoteau, A., Gralnick, J. A., & Arends, J. B. A., 2018. A Novel Shewanella Isolate Enhances Corrosion by Using Metallic Iron as the Electron Donor with Fumarate as the Electron Acceptor, .

Phoenix, V. R., Martinez, R. E., Konhauser, K. O., & Ferris, F. G., 2002. Characterization and implications of the cell surface reactivity of *Calothrix* sp strain KC97. Appl. Environ. Microbiol., 68, 4827–4834. https://doi.org/10.1016/j.gca.2004.02.007.

Pinel, I., Biškauskait, R., Pal, E., & Vrouwenvelder, H., 2021. Assessment of the Impact of Temperature on Biofilm Composition with a Laboratory Heat Exchanger Module. Microorganisms, 9, 1185. https://doi.org/5. https://doi.org/ 10.3390/microorganisms9061185.

Plette, A. C., van Riemskijk, W., Benebeiti, M. F., & van del Wal, A., 1995. pH Dependant Charging Behavoir of Isolated Cell Walls of a Gram-Positive Bacterium. J. Colloid Interface Sci., 173, 354–363. https://doi.org/10.1006/jcis.1995.1335.

Povedano-priego, C., Jroundi, F., Lopez-fernandez, M., Huertas, F. J., & Dopson, M., 2022. Applied Clay Science Impact of anoxic conditions , uranium (VI) and organic phosphate substrate on the biogeochemical potential of the indigenous bacterial community of bentonite. Appl. Clay Sci., 216, 106331.

Rahmelow, K., Hübner, W., & Ackermann, T., 1998. Infrared absorbances of protein side chains. Anal. Biochem., 257, 1–11. https://doi.org/10.1006/abio.1997.2502.

Rahnamoun, A., Kim, K., Pedersen, J. A., & Hernandez, R., 2020. Ionic Environment Affects Bacterial Lipopolysaccharide Packing and Function. Langmuir, 36, 3149–3158. https://doi.org/10.1021/acs.langmuir.9b03162.

Ramirez, C., Shimmin, L. C., Leggatt, P., & Matheson, A. T., 1994. Structure and Transcription of the L11-L1-L10-L12 Ribosomal Protein Gene Operon from the Extreme Thermophilic Archaeon Sulfolobus acidocaldarius. J. Mol. Biol., 244, 242–249.

Ray, C., Glein, C. R., Waite, J. H., Teolis, B., Hoehler, T., Huber, J. A., Lunine, J., & Postberg, F., 2021. Oxidation processes diversify the metabolic menu on Enceladus. Icarus, 364, 114248. https://doi.org/10.1016/j.icarus.2020.114248.

Reddy, T. R., & Suryanarayana, T., 1988. Novel histone-like DNA-binding proteins in the nucleoid from the acidothermophillic archaebacterium Sulfolobus acidocaldarius that

protect DNA against thermal denaturation Thipparthi. Biochim. Biophys. Acta - Bioenerg., 949, 87–96.

Reeve, J. N., Morgan, R. M., & Nolling, J., 1997. Environmental and molecular regulation of methanogenesis. Water Sci. Technol., 36, 1–6.

Robertson, A. P., & Leckie, J. O., 1997. Cation binding predictions of surface complexation models: Effects of pH, ionic strength, cation loading, surface complex, and model fit. J. Colloid Interface Sci., 188, 444–472. https://doi.org/10.1006/jcis.1996.4752.

Rosado, M. T., Duarte, M. L. T., & Fausto, R., 1998. Vibrational spectra of acid and alkaline glycine salts. Vib. Spectrosc., 16, 35–54. https://doi.org/10.1016/S0924-2031(97)00050-7.

Russell, J. B., 2007. The energy spilling reactions of bacteria and other organisms. J. Mol. Microbiol. Biotechnol., 13, 1–11. https://doi.org/10.1159/000103591.

Safonov, A. V., Andryushchenko, N. D., Ivanov, P. V., Boldyrev, K. A., Babich, T. L., German, K. E., & Zakharova, E. V., 2019. Biogenic Factors of Radionuclide Immobilization on Sandy Rocks of Upper Aquifers. Radiochemistry, 61, 99–108. https://doi.org/10.1134/S1066362219010156.

Sang, S., Zhang, X., Dai, H., Hu, B. X., Ou, H., & Sun, L., 2018. Diversity and predictive metabolic pathways of the prokaryotic microbial community along a groundwater salinity gradient of the Pearl River Delta, China. Sci. Rep., 8, 1–11. https://doi.org/10.1038/s41598-018-35350-2.

Sar, P., & D'Souza, S. F., 2001. Biosorptive uranium uptake by a Pseudomonas strain: Characterization and equilibrium studies. J. Chem. Technol. Biotechnol., 76, 1286–1294. https://doi.org/10.1002/jctb.517.

Sawada, K., Miyagawa, T., Sakaguchi, T., & Doi, K., 1993. Structure and thermodynamic properties of aminopoly-phosphonate complexes of the alkaline-earth metal ions. J. Chem. Soc. Dalt. Trans., (pp. 3777–3784). https://doi.org/10.1039/DT9930003777.

Schill, N. A., Liu, J. S., & Von Stockar, U., 1999. Thermodynamic analysis of growth of Methanobacterium thermoautotrophicum. Biotechnol. Bioeng., 64, 74–81. https://doi.org/10.1002/(SICI)1097-0290(19990705)64:1¡74::AID-BIT8¿3.0.CO;2-3.

Schneck, E., Papp-Szabo, E., & Quinn, B., 2009. Calcium ions induce collapse of charged O-side chains of lipopolysaccharides from Pseudomonas aeruginosa. J. R. Soc. Interface, 6, S671–S678. https://doi.org/https://doi.org/10.1098/rsif.2009.0190.focus.

Schramm, F. D., Schroeder, K., & Jonas, K., 2019. Protein aggregation in bacteria. FEMS Microbiol. Rev., 44, 54–72. https://doi.org/10.1093/femsre/fuz026.

Selinummi, J., Seppälä, J., Yli-Harja, O., & Puhakka, J. A., 2005. Software for quantification of labeled bacteria from digital microscope images by automated image analysis. Biotechniques, 39, 859–862. https://doi.org/10.2144/000112018.

Sheng, L., & Fein, J. B., 2013a. Uranium adsorption by Shewanella oneidensis MR-1 as a function of dissolved inorganic carbon concentration. Chem. Geol., 358, 15–22. https://doi.org/10.1016/j.chemgeo.2013.08.039.

Sheng, L., & Fein, J. B., 2013b. Uranium adsorption by Shewanella oneidensis MR-1 as a function of dissolved inorganic carbon concentration. Chem. Geol., 358, 15–22. https://doi.org/10.1016/j.chemgeo.2013.08.039.

Sheng, L., Szymanowski, J., & Fein, J. B., 2011. The effects of uranium speciation on the rate of U(VI) reduction by Shewanella oneidensis MR-1. Geochim. Cosmochim. Acta, 75, 3558–3567. https://doi.org/10.1016/j.gca.2011.03.039.

Shock, E. L., Helgeson, H. C., & Sverjensky, D. A., 1989. Calculation of the thermodynamic and transport properties of aqueous species at high pressures and temperatures : Standard partial molal properties of inorganic neutral species. Geochim. Cosmochim. Acta, 53, 2157–2183.

Silhavy, T. J., Kahne, D., & Walker, S., 2010. The bacterial cell envelope. Cold Spring Harb. Perspect. Biol., 2. https://doi.org/10.1101/cshperspect.a000414.

Simpson, B. W., & Trent, M. S., 2019. Pushing the envelope: LPS modifications and their consequences. Nat. Rev. Microbiol., 17, 403–416. https://doi.org/10.1038/s41579-019-0201-x.

Sitte, J., Löffler, S., Burkhardt, E.-m., Goldfarb, K. C., Büchel, G., Hazen, T. C., & Küsel, K., 2015. Metals other than uranium affected microbial community composition in a historical uranium-mining site. Env. Sci Pollut Res, 22, 19326–19341. https://doi.org/10.1007/s11356-015-4791-1.

Smeaton, C. M., & Van Cappellen, P., 2018. Gibbs Energy Dynamic Yield Method (GEDYM): Predicting microbial growth yields under energy-limiting conditions. Geochim. Cosmochim. Acta, 241, 1–16. https://doi.org/10.1016/j.gca.2018.08.023.

Smith, D. S., & Ferris, F. G., 2003. Specific surface chemical interactions between hydrous ferric oxide and iron-reducing bacteria determined using pKa spectra. J. Colloid Interface Sci., 266, 60–67. https://doi.org/10.1016/S0021-9797(03)00667-2.

Smith, J. N., & Shock, E. L., 2007. A thermodynamic analysis of microbial growth experiments. Astrobiology, 7, 891–904. https://doi.org/10.1089/ast.2006.0118.

Smith, R. M., Martell, A. E., & Motekaitis, R. J., 2004. NIST critically selected stability constants of metal complexes database. NIST Stand. Ref. Database 46, (pp. National Institute of Standard and Technology, Gai).

Sokolov, I., Smith, D. S., Henderson, G. S., Gorby, Y. A., & Ferris, F. G., 2001. Cell surface electrochemical heterogeneity of the Fe(III)-reducing bacteria Shewanella putrefaciens. Environ. Sci. Technol., 35, 341–347. https://doi.org/10.1021/es001258s.

Sousa, F. L., Preiner, M., & Martin, W. F., 2018. Native metals, electron bifurcation, and CO2 reduction in early biochemical evolution. Curr. Opin. Microbiol., 43, 77–83. https://doi.org/10.1016/j.mib.2017.12.010.

Speers, A. M., & Reguera, G., 2012. Electron donors supporting growth and electroactivity of geobacter sulfurreducens anode biofilms. Appl. Environ. Microbiol., 78, 437–444. https://doi.org/10.1128/AEM.06782-11.

Stanley, D. M., & Wilkin, R. T., 2019. Solution equilibria of uranyl minerals: Role of the common groundwater ions calcium and carbonate. J. Hazard. Mater., 377, 315–320. https://doi.org/10.1016/j.jhazmat.2019.05.101.

Stetter, K. O., 1999. Extremophiles and their adaptation to hot environments. FEBS Lett., 452, 22–25. https://doi.org/10.1016/S0014-5793(99)00663-8.

von Stockar, U., Larsson, C., & Marison, I. W., 1993. Calorimetry and energetic efficiencies in aerobic and anaerobic microbial growth. Pure Appl. Chem., 65, 1889–1892.

von Stockar, U., Maskow, T., Liu, J., Marison, I. W., Pati, R., & M, C. U., 2006. Thermodynamics of microbial growth and metabolism : An analysis of the current situation, . 121, 517–533. https://doi.org/10.1016/j.jbiotec.2005.08.012.

Stylo, M., Alessi, D. S., Shao, P. P., Lezama-Pacheco, J. S., Bargar, J. R., & Bernier-Latmani, R., 2013. Biogeochemical controls on the product of microbial U(VI) reduction. Environ. Sci. Technol., 47, 12351–12358. https://doi.org/10.1021/es402631w.

Tanger, J., & Helgeson, H., 1988. Calculation of the thermodynamic and transport properties of aqueous species at high pressures and temperatures; revised equations of state for the standard partial molal properties of ions and electrolytes. Am. J. Sci., 288, 19–98. https://doi.org/10.2475/ajs.288.1.19.

Tebes-Stevens, C., J. Valocchi, A., Vanbriesen, J. M., & Rittmann, B. E., 1998. Multicomponent transport with coupled geochemical and microbiological reactions: Model description and example simulations. J. Hydrol., 209, 8–26. https://doi.org/10.1016/S0022-1694(98)00104-8.

Torres, E., 2020. Biosorption: A review of the latest advances. Processes, 8, 1–23. https://doi.org/10.3390/pr8121584.

Tournassat, C., Tinnacher, R. M., Grangeon, S., & Davis, J. A., 2018. Modeling uranium(VI) adsorption onto montmorillonite under varying carbonate concentrations: A surface complexation model accounting for the spillover effect on surface potential. Geochim. Cosmochim. Acta, 220, 291–308. https://doi.org/10.1016/j.gca.2017.09.049.

Tourney, J., & Ngwenya, B. T., 2010. The effect of ionic strength on the electrophoretic mobility and protonation constants of an EPS-producing bacterial strain. J. Colloid Interface Sci., 348, 348–354. https://doi.org/10.1016/j.jcis.2010.04.082.

Tran, T. M., Han, H. J., Ko, J. I., & Lee, J. U., 2020. Effect of indigenous microbial consortium on bioleaching of arsenic from contaminated soil by Shewanella putrefaciens. Sustain., 12. https://doi.org/10.3390/SU12083286.

Van Bodegom, P., 2007. Microbial maintenance: A critical review on its quantification. Microb. Ecol., 53, 513–523. https://doi.org/10.1007/s00248-006-9049-5.

Ver Eecke, H. C., Butterfield, D. A., Huber, J. A., Lilley, M. D., Olson, E. J., Roe, K. K., Evans, L. J., Merkel, A. Y., Cantin, H. V., & Holden, J. F., 2012. Hydrogen-limited growth

of hyperthermophilic methanogens at deep-sea hydrothermal vents. Proc. Natl. Acad. Sci. U. S. A., 109, 13674–13679. https://doi.org/10.1073/pnas.1206632109.

Vignais, P. M., & Billoud, B., 2007. Occurrence, classification, and biological function of hydrogenases: An overview. Chem. Rev., 107, 4206–4272. https://doi.org/10.1021/cr050196r.

Viollier, E., Inglett, P. W., Hunter, K., Roychoudhury, A. N., & Van Cappellen, P., 2000. The ferrozine method revisited: Fe(II)/Fe(III) determination in natural waters. Appl. Geochemistry, 15, 785–790. https://doi.org/10.1016/S0883-2927(99)00097-9.

Von Stockar, U., & Liu, J. S., 1999. Does microbial life always feed on negative entropy? Thermodynamic analysis of microbial growth. Biochim. Biophys. Acta - Bioenerg., 1412, 191–211. https://doi.org/10.1016/S0005-2728(99)00065-1.

Von Stockar, U., Marison, I. W., & Liu, J. S., 2000. Endothermic microbial growth. A calorimetric investigation of an extreme case of entropy-driven microbial growth. Pure Appl. Chem., 72, 1835–1838. https://doi.org/10.1351/pac200072101835.

Wainipee, W., Cuadros, J., Sephton, M. A., Unsworth, C., Gill, M. G., Strekopytov, S., & Weiss, D. J., 2013. The effects of oil on As(V) adsorption on illite, kaolinite, montmorillonite and chlorite. Geochim. Cosmochim. Acta, 121, 487–502. https://doi.org/10.1016/j.gca.2013.07.018.

Weiss, M. C., Sousa, F. L., Mrnjavac, N., Neukirchen, S., Roettger, M., Nelson-Sathi, S., & Martin, W. F., 2016. The physiology and habitat of the last universal common ancestor. Nat. Microbiol., 1, 1–8. https://doi.org/10.1038/nmicrobiol.2016.116.

Welte, W., Nestel, U., Wacker, T., & Diederichs, K., 1995. Structure and function of the porin channel. Kidney Int., 48, 930–940. https://doi.org/10.1038/ki.1995.374.

Westall, J. C., Jones, J. D., Turner, G. D., & Zachara, J. M., 1995. Models for Association of Metal Ions with Heterogeneous Environmental Sorbents. 1. Complexation of Co(II) by Leonardite Humic Acid as a Function of pH and NaClO4 Concentration. Environ. Sci. Technol., 29, 951–959. https://doi.org/10.1021/es00004a015.

Wightman, P. G., Fein, J. B., Wesolowski, D. J., Phelps, T. J., Benezeth, P., & Palmer, D. A., 2001. Measurement of bacterial surface protonation constants for two species at elevated temperatures. Geochim. Cosmochim. Acta, 65, 3657–3669. https://doi.org/10.1016/S0016-7037(01)00763-3.

Willey, J., Sherwood, L., & Woolverton, C., 2008. *Prescott, Harley, and Klein's Microbiology*. McGraw-Hill Higher Education.

Wilson, W. W., Wade, M. M., Holman, S. C., & Champlin, F. R., 2001. Status of methods for assessing bacterial cell surface charge properties based on zeta potential measurements. J. Microbiol. Methods, 43, 153–164. https://doi.org/10.1016/S0167-7012(00)00224-4.

Wojdyr, M., 2010. Fityk: A general-purpose peak fitting program. J. Appl. Crystallogr., 43, 1126–1128. https://doi.org/10.1107/S0021889810030499.

Wray, A., & Gorman-Lewis, D., 2022. Thermodynamic and spectroscopic investigations of Shewanella putrefaciens CN32 cell envelope. Chem. Geol., 600, 120853. https://doi.org/10.1016/j.chemgeo.2022.120853.

Wu, C., Cheng, Y. Y., Yin, H., Song, X. N., Li, W. W., Zhou, X. X., Zhao, L. P., Tian, L. J., Han, J. C., & Yu, H. Q., 2013. Oxygen promotes biofilm formation of Shewanella putrefaciensCN32through a diguanylate cyclase and an adhesin. Sci. Rep., 3, 1–7. https://doi.org/10.1038/srep01945.

Xu, Y., Schoonen, M. A., Nordstrom, D. K., Cunningham, K. M., & Ball, J. W., 1998.

Sulfur geochemistry of hydrothermal waters in Yellowstone National Park: I. The origin of thiosulfate in hot spring waters. Geochim. Cosmochim. Acta, 62, 3729–3743. https://doi.org/10.1016/S0016-7037(98)00269-5.

Yan, J., Xie, J., Lin, L., & Flint, S., 2020. Comparative Proteome Analysis of Shewanella putrefaciens WS13 Mature Biofilm Under Cold Stress. Front. Microbiol., 11, 1–10. https://doi.org/10.3389/fmicb.2020.01225.

Yang, Y., Wang, S., & Albrecht-Schmitt, T. E., 2014. Microbial dissolution and reduction of uranyl crystals by Shewanella oneidensis MR-1. Chem. Geol., 387, 59–65. https://doi.org/10.1016/j.chemgeo.2014.08.020.

Zenobi, M. C., Luengo, C. V., Avena, M. J., & Rueda, E. H., 2008. An ATR-FTIR study of different phosphonic acids in aqueous solution. Spectrochim. Acta - Part A Mol. Biomol. Spectrosc., 70, 270–276. https://doi.org/10.1016/j.saa.2007.07.043.

Zinder, S. H., Anguish, T., & Cardwell, S. C., 1984. Effects of temperature on methanogenesis in a thermophilic (58° C) anaerobic digestor. Appl. Environ. Microbiol., 47, 808–813. https://doi.org/10.1128/aem.47.4.808-813.1984.

Zou, Y., Wang, X., Khan, A., Wang, P., Liu, Y., Alsaedi, A., Hayat, T., & Wang, X., 2016. Environmental Remediation and Application of Nanoscale Zero-Valent Iron and Its Composites for the Removal of Heavy Metal Ions: A Review. Environ. Sci. Technol., 50, 7290–7304. https://doi.org/10.1021/acs.est.6b01897.

Appendix A

SUPPLMENTARY MATERIALS

A.1 Chapter 2

Table A.1: Extrapolated enthalpies of hydroxide neutralization at each ionic strength analyzed, according to and interpolated from Smith et al. (2004)

Ionic strength (M)	ΔH kJ mol^{-1}
0.02 – 0.04	-56.02
0.11 – 0.13	-56.48
0.51 – 0.53	-56.65

Table A.2: Surface complexation model parameters and thermodynamic potentials for the 1-site model at low, medium, and high ionic strengths. Standard error is reported.

IS (M)	Site	log(K)	[C] (μmol/g)	ΔG (kJ/mol)	ΔH (kJ/mol)	ΔS (J/molK^{-1})
0.02 - 0.04	$L1$	3.18 ± 0.73	-9 ± 0	-18.12 ± 4.19	-1988.92 ± 399.86	-6613.4 ± 1341.9
0.11 - 0.13	$L1$	6.99 ± 0.13	-9 ± 0	-39.90 ± 0.76	34.07 ± 0.87	248.2 ± 3.9
0.51 - 0.53	$L1$	6.48 ± 0.04	-9 ± 0	-36.95 ± 0.21	43.38 ± 0.39	269.6 ± 1.5

Table A.3: Surface complexation model parameters and thermodynamic potentials for the 2-site model at low, medium, and high ionic strengths. Standard error is reported.

IS (M)	Site	log(K)	[C] (μmol/g)	ΔG (kJ/mol)	ΔH (kJ/mol)	ΔS (J/molK^{-1})
0.02 - 0.04	$L1$	5.52 ± 0.21	114 ± 5	-31.50 ± 1.21	-8.38 ± 0.74	77.6 ± 4.8
	$L2$	8.88 ± 0.08	103 ± 5	-50.64 ± 0.48	-38.25 ± 0.68	41.6 ± 2.8
0.11 - 0.13	$L1$	5.97 ± 0.03	147 ± 3	-34.05 ± 0.18	-10.98 ± 0.65	77.4 ± 2.3
	$L2$	9.11 ± 0.04	176 ± 8	-51.97 ± 0.20	-38.09 ± 0.66	46.6 ± 2.3
0.51 - 0.53	$L1$	5.60 ± 0.01	135 ± 1	-31.94 ± 0.04	-11.96 ± 0.49	67.1 ± 1.6
	$L2$	9.31 ± 0.02	114 ± 4	-53.09 ± 0.10	-17.52 ± 0.69	119.4 ± 2.3

Table A.4: Surface complexation model parameters and thermodynamic potentials for the 4-site model at low, medium, and high ionic strengths. Changes in equilibrium constants of protonation (ΔK) reflect the difference between constants at 20°C and 45°C, as determined with Equation 8. Standard error is reported.

IS (M)	Site	log(K)	[C] (μmol/g)	ΔG (kJ/mol)	ΔH (kJ/mol)	ΔS (J/molK^{-1})	$\lvert\Delta K\rvert$
0.02 - 0.04	*L*1	4.20 ± 0.04	27 ± 1	-23.94 ± 0.25	11.35 ± 20.23	118.4 ± 67.9	0.16
	*L*2	5.01 ± 0.04	77 ± 5	-28.60 ± 0.24	-10.73 ± 4.16	60.0 ± 14.0	0.15
	*L*3	7.00 ± 0.05	69 ± 1	-39.94 ± 0.28	-13.07 ± 1.75	90.2 ± 6.0	0.18
	*L*4	9.47 ± 0.03	9 ± 5	-54.02 ± 0.16	-61.33 ± 1.93	-24.5 ± 6.5	0.86
0.11 - 0.13	*L*1	4.56 ± 0.10	102 ± 2	-26.00 ± 0.59	-8.10 ± 2.61	60.1 ± 9.0	0.11
	*L*2	6.09 ± 0.37	74 ± 10	-34.73 ± 2.11	-8.20 ± 3.20	89.0 ± 12.9	0.11
	*L*3	7.23 ± 0.26	55 ± 13	-41.23 ± 1.50	-21.68 ± 3.76	65.6 ± 13.6	0.30
	*L*4	9.42 ± 0.07	170 ± 10	-53.76 ± 0.41	-49.98 ± 1.62	12.7 ± 5.6	0.70
0.51 - 0.53	*L*1	4.86 ± 0.03	117 ± 2	-27.71 ± 0.18	-10.30 ± 0.82	58.4 ± 2.8	0.14
	*L*2	6.46 ± 0.04	64 ± 1	-36.87 ± 0.24	-14.20 ± 1.74	76.1 ± 5.9	0.20
	*L*3	8.29 ± 0.19	25 ± 5	-47.31 ± 1.07	6.79 ± 7.10	181.5 ± 24.1	0.10
	*L*4	9.87 ± 0.06	114 ± 4	-56.29 ± 0.35	-36.48 ± 3.97	66.5 ± 13.4	0.51

Table A.5: Statistical results from of the 3-site model, comparing enthalpies and entropies of each site as a function of ionic strength. Overall values are shown first, from the *F*-tests, and represent the impact of ionic strength on the results in general. *p*-values from the Tukey post-hoc analysis are shown subsequently for each ionic strength comparison at each site.

Parameter	Site	Overall *F*-value	Overall *p*-value	Low v. Medium (*p*)	Low v. High (*p*)	Medium v. High (*p*)
ΔH	1	3.54	0.03	0.86	0.04	0.11
ΔH	2	1.54	0.22	0.98	0.36	0.25
ΔH	3	282	$\ll 0.05$	$\ll 0.05$	$\ll 0.05$	$\ll 0.05$
ΔS	1	2.4	0.09	0.72	0.09	0.35
ΔS	2	0.82	0.44	0.79	0.86	0.41
ΔS	3	211	$\ll 0.05$	$\ll 0.05$	$\ll 0.05$	$\ll 0.05$

Table A.6: Statistical results of *F*-tests comparing 3- and 4-site model fits to potentiometric and ITC data. Statistical significance (here, at 95% confidence) indicates the more complex (4-site) model was a better fit to the data.

Potentiometric (P)/ITC	IS (M)	*F*-value	*p*-value	Optimal #-sites
P	Low	1.81	0.17	3
P	Low	16.59	$\ll 0.05$	4
P	Low	17.45	$\ll 0.05$	4
P	Medium	0.52	0.98	3
P	Medium	66.70	$\ll 0.05$	4
P	Medium	22.24	$\ll 0.05$	4
P	Medium	12.70	$\ll 0.05$	4
P	High	96.26	$\ll 0.05$	4
P	High	70.00	$\ll 0.05$	4
P	High	5.47	$\ll 0.05$	4
ITC	Low	0.39	0.84	3
ITC	Low	0.16	0.70	3
ITC	Medium	0.00	1.00	3
ITC	Medium	0.45	0.51	3
ITC	High	2.40	0.14	3
ITC	High	4.13	0.06	3

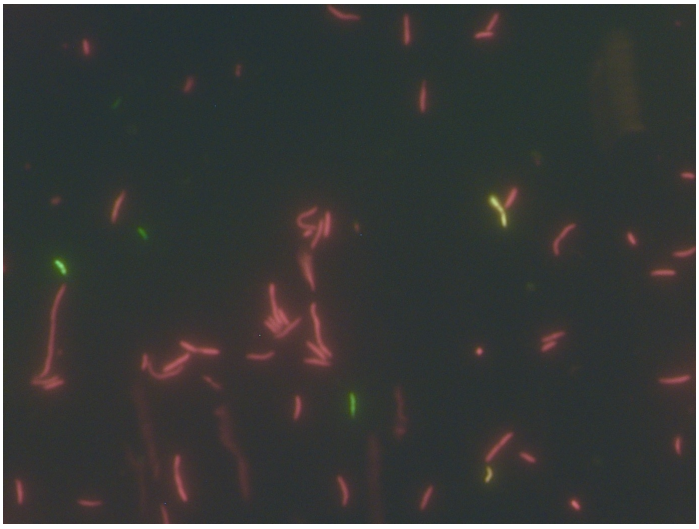

Figure A.1: Example of CN32 cells suspended in a solution of sodium perchlorate at pH 4. Green and yellow-green cells are viable and red cells are non-viable. Importantly, both viable and non-viable cells exhibit a nearly identical structure, indicating the surface of non-viable cells was equivalent to that of viable cells. This inference is supported by the potentiometric titration data, where stability constants and site concentrations were nearly identical between initial and reversibility titrations, despite the loss of cellular viability.

Table A.7: Viability of CN32 cells over experimental conditions. A 5% error was assigned to each value.

Condition	pH	Viability (%)
Post-washing	ca. 6.8	72
Pre-intial titration	10	77
Post-initial titration	4	51
Post-reversibility titration	4	6

Table A.8: Weight-to-Dry weight data. Error for average wet:dry ratio is standard error.

Replicate	Wet Weight (g)	Dry Weight (g)	Ratio (wet:dry)
1	0.02892	0.00814	3.55283
2	0.06243	0.01597	3.90920
3	0.09626	0.02325	4.14022
4	0.13414	0.03261	4.11346
5	0.15248	0.03820	3.99162
	Average ratio:	3.94147 ± 0.10575	

Table A.9: ITC model output enthalpies of protonation using previously identified stability constants by Sokolov et al. (2001) and Smith & Ferris (2003), with entropies of protonation calculated from those values.

Reference	Site	log(K)	ΔH (kJ/mol)	ΔS (J/molK^{-1})
Sokolov et al. (2001)	$L1$	3.72 ± 0.06	-11.8 ± 10.6	31.6 ± 35.6
	$L2$	4.95 ± 0.02	-3.1 ± 2.6	84.4 ± 8.7
	$L3$	6.64 ± 0.50	-18.6 ± 2.7	64.7 ± 9.1
	$L4$	8.83 ± 0.02	-165 ± 14.2	-383 ± 47.6
	$L5$	9.99 ± 0.01	-46.3 ± 7.4	36.0 ± 24.8
Smith & Ferris (2003)	$L1$	3.62 ± 0.06	-8.7 ± 36.3	40.1 ± 122
	$L2$	4.97 ± 0.03	-4.6 ± 3.4	79.7 ± 11.4
	$L3$	6.92 ± 0.04	-28.2 ± 13.8	37.9 ± 46.3
	$L4$	8.22 ± 0.02	-72.2 ± 14.2	-84.8 ± 47.6
	$L5$	9.97 ± 0.07	-108 ± 11.8	-171 ± 39.6

Table A.10: Ranges of thermodynamic properties for the protonation of characteristic surface structures.

Structure	log(K)	ΔH (kJ/mol)	ΔS (J/mol)	Reference(s)
Carboxylic acid	4.76 – 6.66	−11.0 – 0.9	N/A	Goldberg et al. (2002)
Carboxylic acid (in EDTAPA)	4.38	−12.98	40.3	Danil De Namor & Pacheco Tanaka (1998)
Polyphosphate	2.22 – 9.49	5 – 18.8	50.3 – 171	De Stefano et al. (2004)
Polyphosphate	2.96 – 13.07	−9 – 44.5	87.2 – 175.8	Sawada et al. (1993)
Amine (with adjacent carboxyl)	1.35 – 10.13	−99 – 15	−23 – 334	De Robertis et al. (1991)

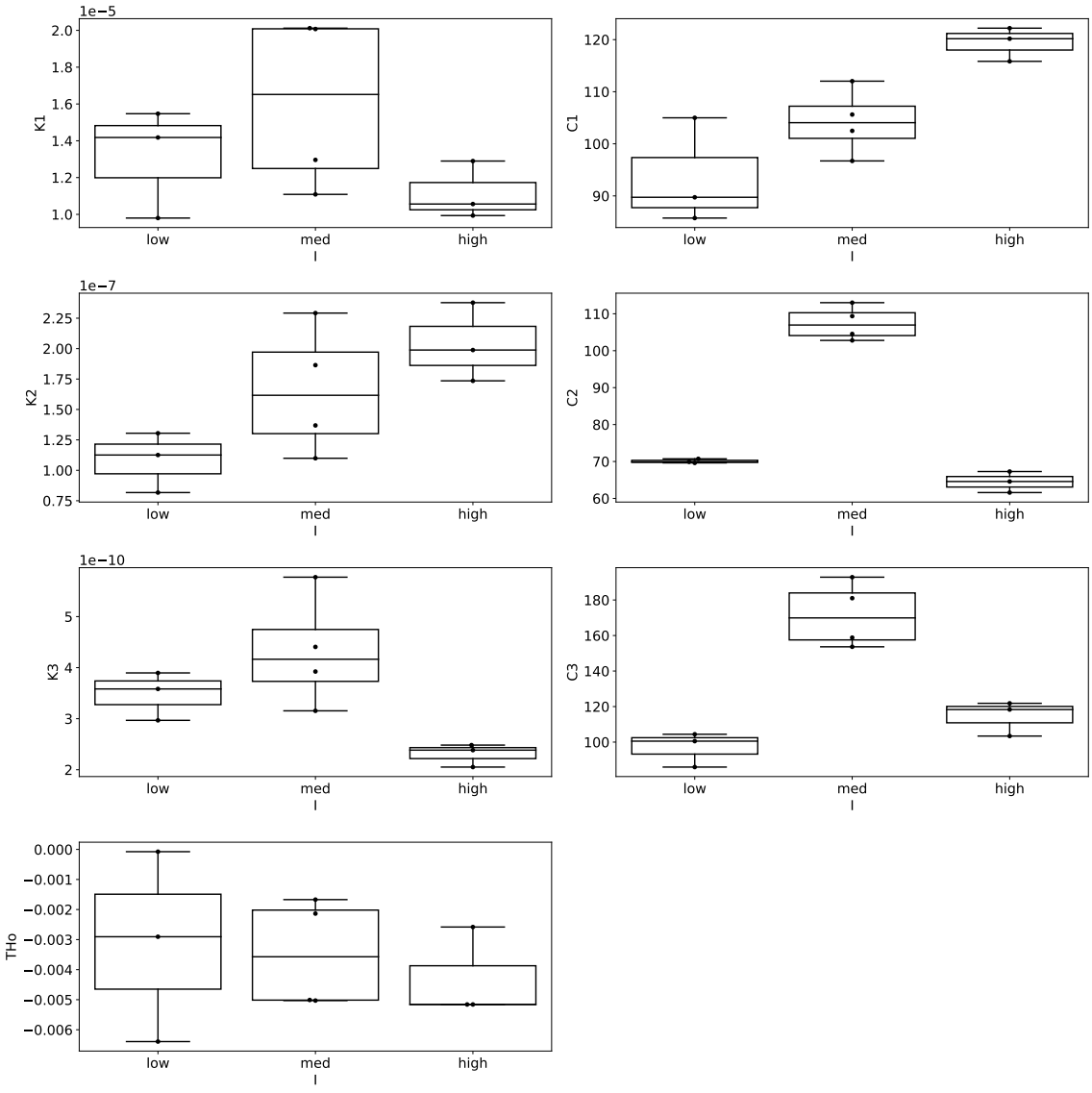

Figure A.2: Dissociation constants, concentrations, and T_H^0 distributions for each experiment. Statistically significant effects of ionic strength, at 95% confidence, were observed for K3, C1, C2, and C3.

A.1.1 FTIR Results

For IR band *c*, deconvolution can help to establish the relative contributions of asymmetric and symmetric bending of NH_3 groups. Specifically, while the peak at *c* is maintained (though slightly red shifted), at least four additional peaks are shown to contribute to the spectral signature in this region. Those are centered at 1498, 1527, and 1571 cm^{-1}. Grube et al. (2008) showed that bands at 1527 cm^{-1} correspond to nitro aromatic compounds. This suggests there is potential for multiple N-based vibrations, including the N-H and N-C vibrations from the amide II band itself. The other two peaks, at 1498 and 1571 cm^{-1}, while less prominent, are assigned to symmetric bending of an NH_3 group and a deprotonated carboxyl group (Rahmelow et al., 1998).

As shown in Figure A.3, in the region containing IR bands *g*, *h*, and *i*, peak positions at ca. 1118, 1084, and 1053 cm^{-1} were largely maintained. However, in between each of these peaks, an additional peak influences the overall structure. Between *g* and *h*, there is a peak at 1101 cm^{-1}, and between *h* and *i*, there is a peak at 1074 cm^{-1}. The peak at 1101 cm^{-1} is consistent with asymmetric stretching of PO_3^{2-}. The peak at 1074 cm^{-1} may also indicate PO_3^{2-} presence, or symmetric stretching of C-O-C or C-C bonds (Parikh & Chorover, 2006).

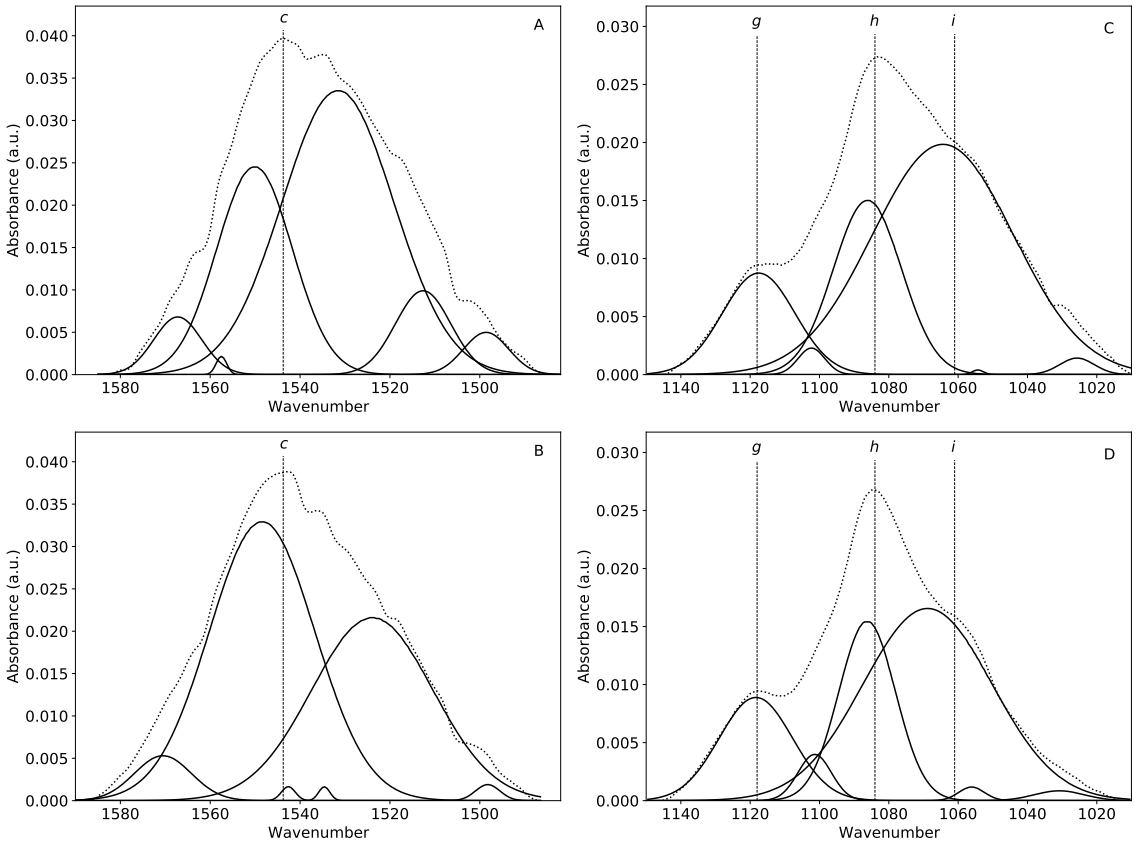

Figure A.3: Spectral regions of biomass containing peaks *c*, *g*, *h*, and *i*. Vertical broken lines indicate IR band assignments before deconvolution. A and C are at pH 4, and B and D are at pH 9. The summed spectra are broken curves, and the constituent Gaussian peaks are solid.

Table A.11: 1σ error of peak locations.

IR Band(s)/pH	Peak	Error
c (pH 4)	1499	0.5
c	1513	0.3
c	1532	3.0
c	1550	1.4
c	1558	0.2
c	1567	0.5
c (pH 9)	1498	0.3
c	1524	1.2
c	1535	0.2
c	1543	0.2
c	1548	0.6
c	1570	0.4
g, *h*, *i* (pH 4)	1026	0.3
g, *h*, *i*	1054	0.5
g, *h*, *i*	1064	0.7
g, *h*, *i*	1086	0.1
g, *h*, *i*	1102	0.2
g, *h*, *i*	1117	0.2
g, *h*, *i* (pH 9)	1031	0.6
g, *h*, *i*	1056	0.2
g, *h*, *i*	1069	1.6
g, *h*, *i*	1086	0.1
g, *h*, *i*	1101	0.2
g, *h*, *i*	1118	0.4

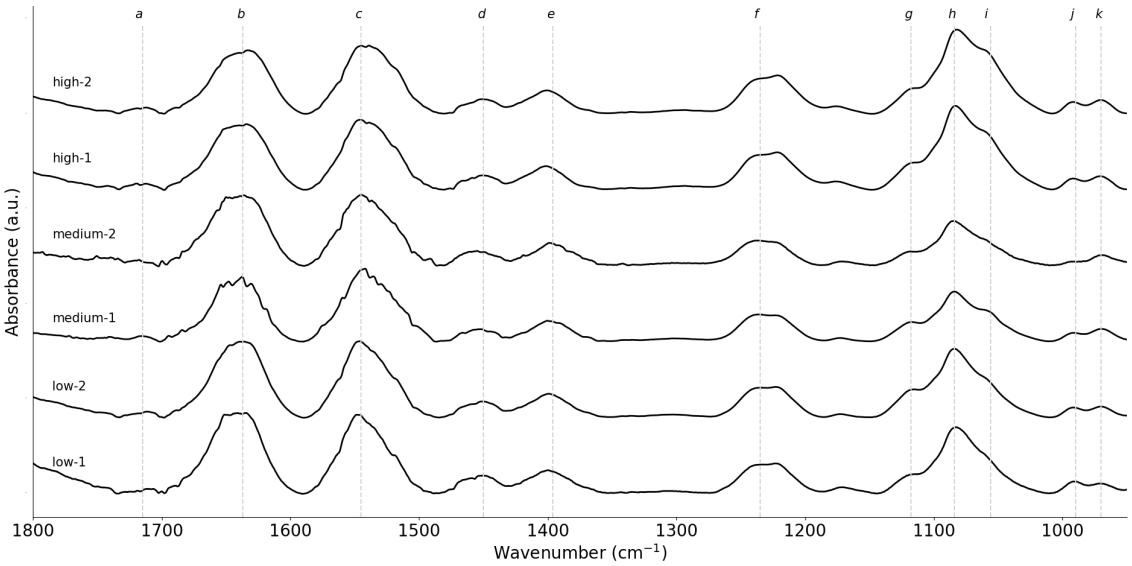

Figure A.4: FTIR spectra at each ionic strength investigated. Two spectra were taken at each ionic strength. Band assignments are summarized in main text and did not change with ionic strength.